PROCESSING FOAM-LIKE POROUS GLASS STRUCTURE USING A COMBINED PROCESS OF GLASS POWDER EXPANSION IN AQUEOUS ENVIRONMENT AND SINTERING PROCESS

A Thesis Submitted to
the Graduate School of Engineering and Sciences of
İzmir Institute of Technology
in Partial Fulfillment of the Requirements for the Degree of

DOCTOR OF PHILOSOPHY

in Materials Science and Engineering

by
Doğuş ZEREN

July 2019
İZMİR

We approve the thesis of **Doğuş ZEREN**

Examining Committee Members:

Prof. Dr. Mustafa GÜDEN
Department of Mechanical Engineering, İzmir Institute of Technology

Prof. Dr. Sedat AKKURT
Department of Mechanical Engineering, İzmir Institute of Technology

Prof. Dr. Mustafa M. DEMİR
Department of Materials Science and Engineering, İzmir Institute of Technology

Prof. Dr. Ali Aydın GÖKTAŞ
Department of Metallurgical and Materials Engineering, Dokuz Eylül University

Assoc. Prof. Dr. Emre YALAMAÇ
Department of Metallurgical and Materials Engineering, Celal Bayar University

2 July 2019

Prof. Dr. Mustafa GÜDEN
Supervisor, Department of
Mechanical Engineering
İzmir Institute of Technology

Assoc. Prof. Dr. Yaşar AKDOĞAN
Co-Supervisor, Department of
Materials Science and Engineering
İzmir Institute of Technology

Assoc. Prof. Dr. Haldun SEVİNÇLİ
Head of the Department of Materials
Science and Engineering

Prof. Dr. Aysun SOFUOĞLU
Dean of the Graduate School of
Engineering and Sciences

ACKNOWLEDGMENTS

I would like to express my deepest gratitude and appreciation to my supervisor Prof. Dr. Mustafa GÜDEN for his constant support, his valuable advises, guidance and patience throughout my PhD study. I would also like to show gratitude to my former co-supervisor Dr. Ufuk ŞENTÜRK and current co-supervisor Assoc. Prof. Dr. Yaşar AKDOĞAN for their guidance and support. I am also grateful to my other thesis committee members, Prof. Dr. Sedat AKKURT and Prof. Dr. Mustafa M. DEMİR for their advices and support.

I am very grateful to my institution, İzmir Institute of Technology, for providing me research facilities during my thesis study. I would like to thank to Prof. Dr. Muhsin ÇİFTÇİOĞLU and Dr. Özlem DUVARCI for helping me in rheological measurements. I also thank to Prof. Dr. Hürriyet POLAT for her support in the powder characterization in my thesis. I also would like to acknowledge the material support of AKG Gaz Beton company for my experimental study. I would like to thank to the crew of IZTECH Materials Research Center (IYTE-MAM) for their help in the materials characterization tests.

I would like to appreciate my roommates Can SINDIRAÇ and Salim Cenk ELMACI for their support during my graduate years. I would like to thank to my colleagues Tümcan ŞEN, Onur YENİGÜN, Hasan ÇELİK, Sevkan ÜLKER and send my best wishes to previous and current members of DTM-Lab for their support and helping. I would like to thank to my father, mother and brother for their endless support. Last but not least, I wish to express my greatest thankfulness to my wife, Esra TOPEL ZEREN for her encouragement, knowledge and patience during my studies in IZTECH.

ABSTRACT

PROCESSING FOAM-LIKE POROUS GLASS STRUCTURE USING A COMBINED PROCESS OF GLASS POWDER EXPANSION IN AQUEOUS ENVIRONMENT AND SINTERING PROCESS

Soda-lime glass foams were formed by the controlled pore structure of inorganic particle-liquid suspensions at room temperature and then sintered at elevated temperatures between 650ºC-800 ºC. The slurries were prepared using the glass particles below 38 μm (fine), between 38 and 45 μm (medium) and between 45 and 56 μm (coarse) and with 50, 55, and 60 wt% solid content and 2, 3, and 4 wt% carboxymethyl cellulose (CMC) binder addition. The slurries were foamed using an Al-based foaming agent and a calcium hydroxide alkali activator with an amount of 1 wt%.

An increase in CMC content and a decrease in particle size shifted the slurries from a Newtonian to a non-Newtonian behavior and slurry stabilization with the CMC addition. The extensively increased initial bubble pressure in high viscosity slurries resulted in higher linear expansion rate initially followed by a bursting of gas bubbles. The maximum foam linear expansion of the slurries increased with CMC addition until about ~5 Pa s and the expansions stayed almost constant over 400% expansion, while the slurries with the viscosity above 50 Pa s could not be foamed. The most effective factor on the maximum expansion was found the solid content followed by CMC content and the least effective factor was determined the particle size. Partial bonding of glass particles and excessive shrinkage of glass particles due to the melting of foam green bodies were seen at 650 and 800 ºC sintering temperatures. Prepared foam glasses showed lower compressive strengths and thermal conductivities than the glass foams reported in the literature.

Finally, foaming at room temperature with this technique was found to be more advantageous than conventional glass foam production techniques due to ease of pore formation controlling at room temperature.

ÖZET

SULU ORTAMDA CAM TOZUNUN GENLEŞMESİ VE SİNTERLEME YÖNTEMİNİ BİRLİKTE KULLANARAK KÖPÜKSÜ GÖZENEKLİ CAM YAPILARIN ÜRETİMİ

Soda-kireç cam köpükleri, oda sıcaklığında inorganik tanecik-sıvı süspansiyonlarının kontrollü gözenek yapısı ile oluşturulmuştur ve daha sonra 650-800 ^{o}C arasında yüksek sıcaklıklarda sinterlenmiştir. Bulamaçlar, 38 μm (ince) altı, 38 ve 45 μm arası (orta), ve 45 ve 56 μm arası (kaba) cam partiküller kullanılarak ağırlıkça %50, %55 ve %60 katı oranlarıyla ve ağırlıkça %2, %3 ve %4 CMC bağlayıcı ilavesiyle hazırlanmıştır. Bulamaçlar, ağırlıkça %1 miktarında Al bazlı bir köpürtme ajanı ve ağırlıkça %1 miktarında bir kalsiyum hidroksit alkali aktivatörü kullanılarak köpükleştirilmiştir.

CMC içeriğindeki artış ve tane boyutundaki düşüş, bulamaçları Newtonian 'dan Newtonian olmayan bir davranışa götürmüştür ve CMC ile bulamaçlar stabilize edilmiştir. Yüksek viskoziteli bulamaçlardaki yoğun şekilde artan başlangıç kabarcık basıncı, daha sonra gaz kabarcığı patlamasıyla daha yüksek doğrusal genleşme oranına sebep olmuştur. Bulamaçların maksimum köpük lineer genleşmesi, CMC ilavesi ile yaklaşık ~ 5 Pa s'ye kadar artmıştır ve genleşmeler, %400 genişlemenin üzerinde sabit kalırken, 50 Pa s'nın üzerindeki viskoziteye sahip bulamaçlar köpükleşememiştir. Maksimum genleşmedeki en etkili faktör, katı oranının ardından CMC içeriği olarak bulunmuştur ve en az etkili faktörün tane boyutu olduğu tespit edilmiştir. Cam partiküllerin kısmı olarak bağlanması ve yaş köpük malzemenin aşırı büzülmesi 650 ve 800 ^{o}C sinterleme sıcaklıklarında görülmüştür. Hazırlanan cam köpükler, literatürde bildirilen cam köpüklerden daha düşük basma dayanımı ve termal iletkenlik göstermiştir.

Son olarak, bu teknikle oda sıcaklığında köpükleştirmenin, oda sıcaklığında kontrollü gözenek oluşumu kolaylığından dolayı geleneksel cam köpük üretim tekniklerinden daha avantajlı olduğu bulunmuştur.

TABLE OF CONTENTS

LIST OF FIGURES ix

LIST OF TABLES xv

CHAPTER 1. INTRODUCTION 1

CHAPTER 2. PROCESSING AND PROPERTIES OF AERATED CONCRETE 3

2.1. Aerated Concrete 3

2.2. Microstructure and Mechanical and Thermal Properties of AAC 6

CHAPTER 3. MANUFACTURING METHODS AND PROPERTIES OF GLASS FOAMS 10

3.1. Brief History of Foam and Nodulated Glass Processing 10

3.2. Current Foam Glass and Granule Processing 13

3.3. Foaming Agents 15

3.4. Foaming Kinetics and Mechanical Properties 16

3.5. Mechanical Properties of Glass Foams 19

3.6. Thermal Conductivity of Glass Foams 21

3.7. Current Situation in Glass Foams 22

CHAPTER 4. FOAM STABILITY 24

4.1. Background of Cellular Structures 24

4.2. Foam Stability 29

CHAPTER 5. COLLOIDAL CERAMICS AND RHEOLOGICAL PROPERTIES OF SLURRIES 34

5.1. Colloidal Ceramics 34

5.2. Particle-Particle Forces 34

5.3. Rheology 39

5.4. Stable Suspensions 40

5.5. The Effect of Solid Content, Particle Size and Particle Shape 42

CHAPTER 6. MATERIALS AND EXPERIMENTAL PROCEDURE 43
6.1. Powders 43
6.2. Binder 45
6.3. Characterization 46
6.4. Rheological Properties of Slurries 46
6.5. Slurry Preparation and Foaming Experiments 47
6.6. Sintering of Green Bodies and Preparation for Compression Test and Thermal Conductivity Measurements 52

CHAPTER 7. RESULTS 54
7.1. As-Received Glass Powder 54
7.2. Rheology of Slurries 54
7.3. Characteristics of Foam Expansion 61
7.4. The Expansion Behavior of Slurries: Solid content and CMC Addition 63
7.5. Bubble Distribution 71
7.6. 3^3 Full Factorial Design of Experiments 73
7.7. Microstructural Analysis 77
7.8. Compression Strength and Thermal Conductivity of Sintered Bodies . 83

CHAPTER 8. DISCUSSION 86
8.1. The Effect of Particle Size on the Viscosity and Maximum Expansion 86
8.2. The Effect of Solid Content and CMC Amount on Viscosity 87
8.3. Expansion of Foams 88
8.4. The Foaming Reaction 91
8.5. 3^3 Full Factorial Design Results 91
8.6. Microstructural Analysis and Mechanical and Thermal Properties 92

CHAPTER 9. CONCLUSIONS 95
9.1. Recommendations for Future Studies 96

REFERENCES 98
APPENDIX A 105

LIST OF FIGURES

Figure **Page**

Figure 2.1. Schematic illustration of AAC production 4

Figure 2.2. Schematic illustration of aluminum dissolution in $Ca(OH)_2$ solution 5

Figure 2.3. Pores in AAC (a) artificial air pore, (b) inter-cluster pore and (c) inter-particle pore 7

Figure 2.4. The fracture pictures of (a) AC and (b) fiber added AC test specimen showing crack bridging of fibers 8

Figure 2.5. The effect of moisture content on relative compressive strength 9

Figure 3.1. Foam glass processing (a) vacuuming molten glass, (b) mixing molten glass with foaming agent powder, (c) heating glass powder/foaming powder agent and heating glass powder and foaming agent powder with (d) vermiculate 11

Figure 3.2. Nodulated cellular glass and method of forming based on (a) briquetting and (b) crushing sintered powder mixture 12

Figure 3.3. The influence of glass powder particle size on the microstructure of a glass foam foamed with 5 wt% SiC foaming agent 17

Figure 3.4. The pictures of cells of foam glass processed at (a) 750 (b) 800, (c) 850, (d) 900 and (e) 950 ^{o}C 17

Figure 3.5. The effect of particle size (D50) on the apparent density of foam glasses prepared at same temperature with different heating rate 17

Figure 3.6. The volume expansion-time and temperature-time graphs of (a) three glass powder compacts heated with the same rate and (b) glass powder compacts heated to different temperatures with different heating rates, the numbers corresponding to the different stages of compact expansion 18

Figure 3.7. Geometry of the cross-section of a tetrakaidecahedral cell edge with plateau borders 19

Figure 3.8. The fitting of glass foam compressive strength with Equation 3.1 20

Figure 3.9. Compressive and flexural strength vs. porosity of different samples 21

Figure 3.10. Compressive and bending strength as function of SiC amount 21

Figure **Page**

Figure 3.11. Thermal conductivity of sintered and melt-quenched samples with different foaming agents and amounts 22
Figure 3.12. Number of foam glass related patent publications 23
Figure 3.13. Number of foam glass related patent publications comparing total publications and publications of countries 23
Figure 4.1. Tetrahedral vertex at the intersection of four Plateau borders 24
Figure 4.2. Cell parts: Left Tetrakaidecahedra cell with walls, right: Weaire-Phelan cells 25
Figure 4.3. Radioscopy of aluminum foam showing Plateau borders 25
Figure 4.4. Foaming stages: nucleation, growth, coarsening and decay 26
Figure 4.5. Force balance at the fluid-gas interface 27
Figure 4.6. Transient cell wall formation 28
Figure 4.7. Drainage in cell walls 29
Figure 4.8. Foam stabilization with particles: a) particles with different shapes, b) surface roughness of particles, c) particles absorbed at the interface, d) individual hydrophilic particles, and aggregated or gelified particles in the foam channels, e) aggregated particles adsorbed at the interfaces and in the bulk and f) large aggregates or individual particles in Plateau borders 30
Figure 4.9. Wetting angle effect on the foam stabilization, top partially wetted particles and bottom wetted particles 31
Figure 4.10. Stabilization of foams (Left: poorly wetted, right: wetted particles) 31
Figure 4.11. A typical example of cell wall thickness and disjoining pressure 32
Figure 4.12. Al foam processing parameters 33
Figure 5.1. Clay particles suspended in water a) individual particle b) aggregated particle due to the attractional forces between the particles 34
Figure 5.2. The relationship between interparticle potential energy and the subsequent colloidal structure 35
Figure 5.3. Electric double layer diagram 37
Figure 5.4. Schematic representations of different types of polymers adsorbed in ceramic surfaces: a) homopolymer b) diblock copolymer c) comblike copolymer and d) Functional polymer 38

Figure **Page**

Figure 5.5. Types of rheological behavior a) Newtonian flow, b) shear thinning c) shear thickening d) Bingham plastic and e) pseudoplastic with yield stress 40
Figure 5.6. Degree of shear thinning of silicon nitride suspension at different solid contents 41
Figure 5.7. The relationship between viscosity and volume fraction of different solids 42
Figure 6.1. The picture of as-received waste glass 43
Figure 6.2. a) As-received glass powder and powders sieved between b) 45 and 56 and c) 38 and 45 μm and below d) 38 μm 44
Figure 6.3. The SEM micrographs of Al powder in a) 500x b) 1000x c) 2500x and d) 10000x magnification 45
Figure 6.4. Schematic representation of steric stabilization of glass particles provided by CMC addition 46
Figure 6.5. (a) Haake Mars II Rotational Rheometer device and (b) measurement plate where the sample placed 47
Figure 6.6. Stages of slurry preparation for foaming experiments 48
Figure 6.7. The molding tubes used in foaming experiments (a) Teflon© and (b) Plexiglass transparent tube 48
Figure 6.8. Foaming set-up 50
Figure 6.9. (a) Picture and (b) the technical drawing of Micro Epsilon ILR1030-8 laser sensor 50
Figure 6.10. The image of bubbles (a) from video record and (b) after Image J processing 51
Figure 6.11. (a) Thermal conductivity measurement device and (b) Glass foam sample for thermal conductivity measurement 53
Figure 7.1. The XRD pattern of as-received glass powder 54
Figure 7.2. Three measurements of (a) shear stress-shear rate and (b) viscosity-shear rate curves of the slurry with medium particle size, 50 wt% solid content and with no CMC addition 55

Figure **Page**

Figure 7.3. Three measurements of (a) shear stress-shear rate and (b) viscosity-shear rate curves of the slurry with medium particle size, 50 wt% solid content and 2 wt% CMC 56
Figure 7.4. Three measurements of shear stress-shear rate curves of the slurry with medium particle size, 55 wt% solid content and 2 wt% CMC 56
Figure 7.5. Three measurements of (a) shear stress-shear rate and (b) viscosity-shear rate curves of the slurry with medium particle size, 60 wt% solid content and 2 wt% CMC 57
Figure 7.6. The shear stress-shear rate curves of the slurries with 50 wt% solid and 2, 3 and 4 wt% CMC: (a) fine, (b) medium and (c) coarse powder size 58
Figure 7.7. The shear stress-shear rate curves of the slurries with 55 wt% solid and 2, 3 and 4 wt% CMC: (a) fine, (b) medium and (c) coarse powder size 59
Figure 7.8. The shear stress-shear rate curves of the slurries with 60 wt% solid and 2, 3 and 4 wt% CMC: (a) fine, (b) medium and (c) coarse powder size 60
Figure 7.9. The average viscosity vs. CMC wt% of the slurries with (a) 50, (b) 55 and (c) 60 wt% solid content at 20 s^{-1} shear rate 61
Figure 7.10. (a) Linear expansion-time curve of two foaming experiments and (b) smoothed and experimental foam expansion curves (medium powder with 2wt% CMC addition and 50% solid content) 62
Figure 7.11. Linear expansion-time curve of two foaming experiments and smoothed and experimental foam expansion curves (fine powder with 2wt% CMC addition and 60% solid content) 63
Figure 7.12. The expansion-time curves of slurries prepared with no CMC addition and different powder sizes (a) 50 and (b) 60 wt% solid content 64
Figure 7.13. The expansion-time curves of slurries with 50wt% solid content (a) 2, (b) 3 and (c) 4wt% CMC 65
Figure 7.14. The expansion-time curves of slurries with 55wt% solid content (a) 2, (b) 3 and (c) 4wt% CMC 66
Figure 7.15. The expansion-time curves of slurries with 60wt% solid content (a) 2, (b) 3 and (c) 4wt% CMC 67
Figure 7.16. The expansion-time curves of fine powder slurries with different solid and CMC content 68

Figure **Page**

Figure 7.17. The expansion-time curves of medium powder slurries with different solid and CMC content 69
Figure 7.18. The expansion-time curves of coarse powder slurries with different solid and CMC content 70
Figure 7.19. The expansion-time curves of medium powder with 4% CMC addition and 55% and 50% solid content and the corresponding foam expansion pictures 70
Figure 7.20. The variation of maximum expansion with log viscosity 71
Figure 7.21. The variations bubble diameter of medium powder slurry with 4 wt% CMC at different foaming times a) 50 b) 55 c) 60 wt% percent solid contents 72
Figure 7.22. The variations bubble diameter of medium powder at 9 and 25 minutes with different solid content 73
Figure 7.23. ANOVA diagnostics a) Normality plot of residual b) Predicted vs actual plot according the Response 1 (Maximum Expansion) 75
Figure 7.24. ANOVA diagnostics a) Normality plot of residual and b) Predicted vs. actual plot according the response 2 (viscosity) 76
Figure 7.25. Relationship between maximum expansion and viscosity by simulating the results 77
Figure 7.26. Glass foam green body 77
Figure 7.27. SEM images of the polished surface of foam glass embedded into epoxy matrix at different magnifications (a) 60x (b)100x (c) 250x (d) 1000x 78
Figure 7.28. The pictures of foam samples (a) before sintering and after sintering at (b)750 and (c) 800 ^{o}C 79
Figure 7.29. SEM images of sintered samples with 60 wt% solid content sintered at (a) 700 and (b) 750 ^{o}C 80
Figure 7.30. SEM images of sintered samples with 60 wt% solid content sintered at (a) 700 and (b) 750 ^{o}C showing fractured cell walls 81
Figure 7.31. SEM images of sintered samples sintered at 750 ^{o}C (a) 55 and (b) 60 wt% solid content 82

Figure **Page**

Figure 7.32. SEM images showing cell wall pores in foam samples sintered at 750 ^{o}C (a) 55 and (b) 60 wt% solid content 83
Figure 7.33. The compression stress-strain curves of the foamed and sintered samples (a) 55 wt% solid and 700 ^{o}C, (b) 60 wt% solid and 700 ^{o}C, (c) 55 wt% solid and 750 ^{o}C, (d) 60 wt% solid and 750 ^{o}C and the same foam sample sintered 60 min 84
Figure 7.34. The picture of a failed sintered foam sample in compression test 85
Figure 8.1. The relationship between solid fraction, ϕ and relative viscosity, μ_{rel} 87
Figure 8.2. The interdependence of drainage, coarsening and rheology 89
Figure 8.3. The variations of number of cells in slurries having different solid contents with time 90
Figure 8.4. Schematic representation of the foaming system 91
Figure 8.5. The response surface 3D plot of CMC content-maximum expansion and solid content-maximum expansion 92
Figure 8.6. The collapse strength of glass foams and the present study 93
Figure 8.7. The thermal conductivity of foam glasses and present study 94

LIST OF TABLES

Table **Page**

Table 2.1. The mechanical and thermal properties of AAC 7

Table 3.1. The properties of commercial foam glass products 13

Table 3.2. The composition of container and sheet glass cullet in different countries ... 14

Table 3.3. CRT glass compositions in wt% 15

Table 3.4. Foaming agents and their decomposition reactions 16

Table 5.1. Non-treated Hamaker constants for ceramic materials interacting under vacuum and across water at 298 K 36

Table 6.1. Slurries used in foaming experiments 49

Table 7.1. The measured and average viscosities of the slurries 57

Table 7.2. Responses of the study with different factors and levels 74

Table 7.3. ANOVA table for response 1 (maximum expansion) 75

Table 7.4. ANOVA table for response 2 (viscosity) 76

Table 7.5. The average density and compressive strength of compression tested sintered foam samples 85

Table 7.6. Thermal conductivities of sintered (750 ^{o}C) foams in different solid contents 85

CHAPTER 1

INTRODUCTION

Foams refer to the group of materials in which gas bubbles (cells) are regularly distributed in a liquid phase. Solidified liquid foams referred as to solid foams are classified as metal, polymer and ceramic foams based on the material of which they are made. Glass foams are made of SiO_2 and hence grouped within ceramic foams. Glass foam blocks are commercially available by few different companies and are primarily used for insulation purposes in buildings, water and hot oil pipes and tank bases. The specific applications in buildings include the roof and interior and exterior walls. Glass foams are effective in preventing the spreading of fire once it is ignited, exhibit higher compressive strength than polymeric foams and have comparable strength with metal foams. They have also low moisture absorption coefficient, giving them high durability and long-term life.

Recycled glass called also cullet is a very cheap source of glass foam production. The cullet is initially milled down to micron size powder after sequential and repetitive crushing, grinding and cleaning. Thereafter, the cleaned and milled glass powder is mixed with a foaming agent (e.g SiC, C and $CaCO_3$) at room temperature. In a later stage, the powder mixture is heated to an elevated temperature, typically to 900-1000 ^oC. During heating the glass powder melts, meanwhile the foaming agent decomposes to give a gaseous product such as CO_2 which expands the viscous molten glass.

Aerated concrete (AC), which is also known as a foam material, was invented by Swedish Architect Dr. Johan Axel Eriksson in 1920 together with Professor Henrik Kreüger at the Royal Institute of Technology [1]. The commercial AC production is based on a ceramic slurry of silica, lime, cement and water, which is expanded by the addition of an Al-powder contained foaming agent. The reaction between Al and calcium hydroxide results in H_2 gas evolution, leading to the expansion of slurry. In a final stage, dried foam is autoclaved under a relatively high pressure to give a cellular product called autoclaved aerated concrete (AAC).

In present thesis, a novel glass foam processing method which was a combination of glass powder expansion in aqueous slurry similar to AC and sintering green glass foam structures at high temperature was studied experimentally. A glass powder contained slurry was foamed in an aqueous environment at room temperature and then the foamed green structure was sintered to give a solid structure. The slurries in different solid content (50, 55 and 60 wt%), CMC amount (2, 3 and 4 wt%) and powder size distributions (45-56 μm, 38-45 μm and below 38 μm) were prepared. The rheology and dynamic expansion behavior of these slurries were investigated and the critical relationship between these two and their effects on the control over the pore formation and structure of the green body were discussed. The compressive mechanical properties of the sintered green bodies (600-800 ^{o}C) were also determined.

This study gives a new insight for foam glass production. Compared to conventional foam glass production techniques, the studied method offers more controllable pore size, shape, and distribution by eliminating foaming at a high temperature. The sintering temperature is also lower than that used in conventional techniques, so that the production cost is further lowered. Although, the study has used recycled soda-lime silica glass as the main ingredient, the discussed method lends itself to use other forms and chemistries of recycled glass making it a viable green technology candidate.

CHAPTER 2

PROCESSING AND PROPERTIES OF AERATED CONCRETE

2.1. Aerated Concrete

Concrete is made of approximately one-part Portland cement by volume, two parts fine aggregate (fine limestone or quartz sand), three parts coarse aggregate (course limestone or quartz) and water [2]. Portland cement as the main component of concrete production and considered as the most consumed building material in the world. Its chemical composition encompasses major oxides of CaO, SiO_2, Al_2O_3, Fe_2O_3 and minor oxides of MgO and SO_3 including alkali oxides of K_2O and Na_2O. Limestone, chalk, marl, clays, slags and shale are the main raw materials for the Portland cement production. Its production starts with crushing rocks and mixing the ingredients including iron ore and fly ash. After grounding and homogenizing, the powder mixture is calcined and fused at 1450^{o}C [3].

Aerated concrete (AC) also called cellular concrete or lightweight concrete is formed by entrapping air bubbles in a mortar matrix mechanically or through the reaction of a foaming agent [4]. Low density and low thermal conductivity make AC suitable materials for insulating buildings [4]. It also provides material saving possibilities in structural applications such as side walls and roofs in buildings. Aerated concrete processing also requires much lower processing temperatures (usually processed at room temperature) than cellular ceramic processing such as glass foam that are foamed at an elevated temperature [2].

Aerated concrete production starts with a slurry of silica, Portland cement, lime and water as shown in Figure 2.1. While other siliceous materials such as sandstone, shale ash, fly ash, and their mixtures may replace sand and cement/lime mixtures may replace Portland cement [5]. In an initial step, the raw materials are grinded in order to obtain fine particle size. The method of forming porous structure in the slurry, which is the third step in Figure 2.1, differentiates two types of methods, air-entraining and foaming method. In

the air-entraining method, a gas-forming agent is added to slurry. The reaction of gas-forming agent causes volume expansion and pore formation of slurry. Aluminum powder is the most widely used air-entraining agent. Aluminum flake-shape powder, usually less than 100 μm, and made of foil scrap [1], is added to the slurry in the form of a paste. After mixing the silica sand, lime, cement and water to form a slurry, the slurry is poured into a mold. Upon the addition of Al foaming agent, the following reaction takes place

$$2Al + 3Ca(OH)_2\,(s) + 6\,H_2O\,(l) \rightarrow 3CaO \cdot Al_2O_3 \cdot 6H_2O\,(s) + 3H_2\,(g) \qquad (2.1)$$

The reaction between Al powder and hydrated lime gives rise to tricalcium hydrate and H_2 gas which expands the mortar. In the foaming method, the pores are introduced to the slurry mechanically. Foaming agents like soap, resin and saponin are mixed with the water or mortar in order to obtain pre-formed foaming in matrix [4]. As a final optional step, autoclaving is applied (Figure 2.1). Autoclaving enhances mechanical, shrinkage and absorption behavior of aerated concrete [4, 6].

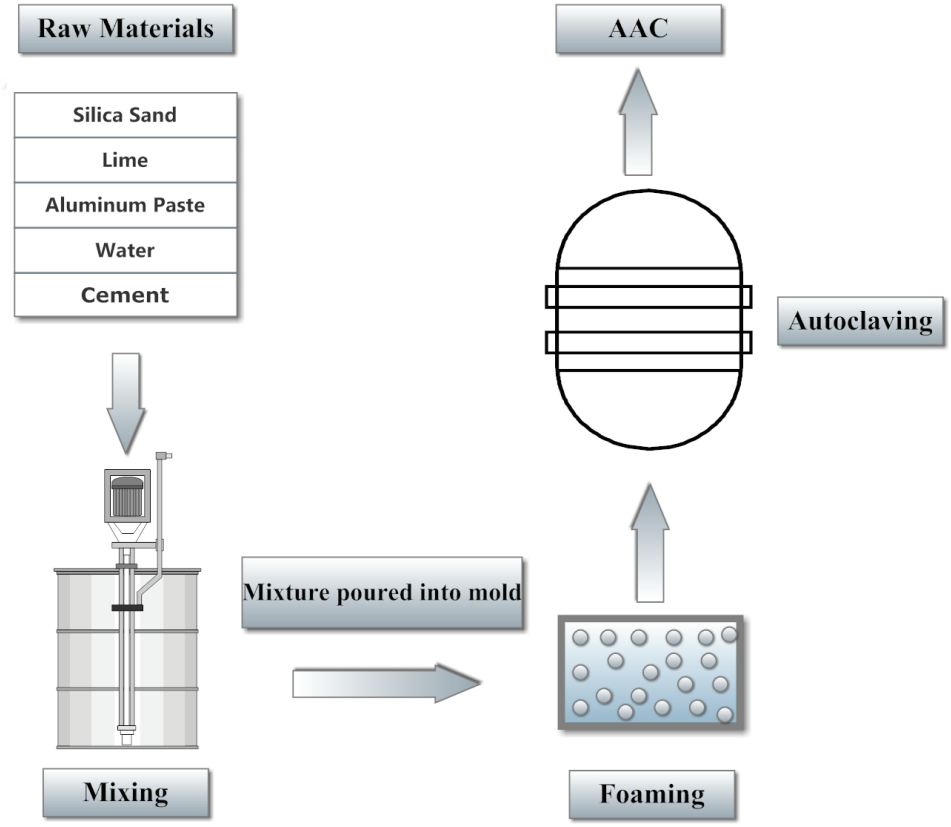

Figure 2.1. Schematic illustration of AAC production

The mechanisms of aluminum powder dispersion in calcium hydroxide solution under controlled hydrogen gas release rate was previously investigated [7]. The reactions between calcium ion, aluminum hydroxide anion and water molecules result in katoite formation and hydrogen release as shown in Figure 2.2.

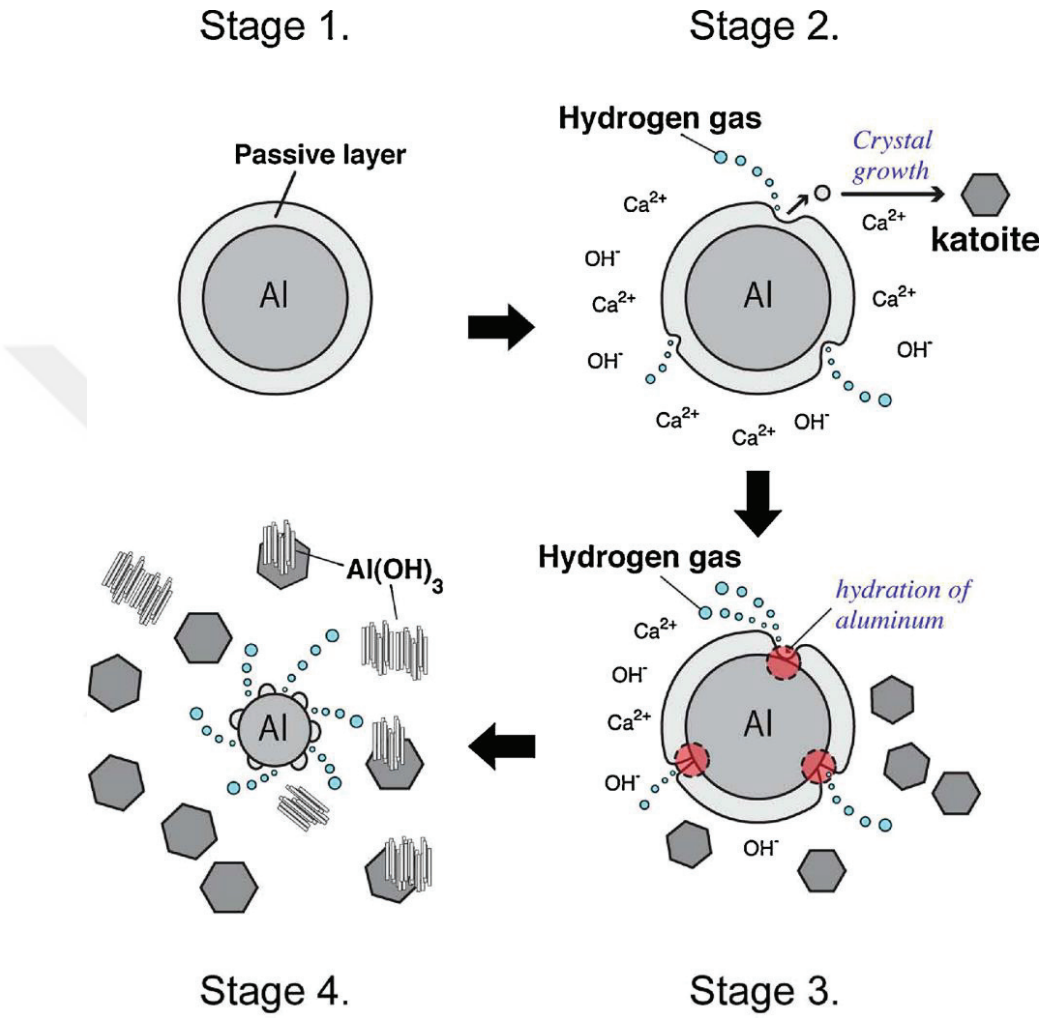

Figure 2.2. Schematic illustration of aluminum dissolution in $Ca(OH)_2$ solution (Source: Kanehira et al., 2013)

The weight ratio of calcium hydroxide was shown to be the most important factor affecting the hydrogen gas release rate [7]. The possible reactions of hydrogen gas release are

$$Al + 3H_2O \rightarrow Al(OH)_3 + 3H_2 \quad (2.2)$$

$$Al + 2H_2O \rightarrow Al(OOH) + 3/2H_2 \quad (2.3)$$

$$Al + 3/2H_2O \rightarrow 1/2Al(OOH) + 3/2H_2 \quad (2.4)$$

The dissolution of aluminum with $Ca(OH)_2$ is accomplished by four stages presented by the reactions given below

$$Al_2O_3 + H_2O \leftrightarrow 2AlOOH \quad (2.5)$$

$$AlOOH + H_2O \leftrightarrow Al(OH)_3 \quad (2.6)$$

$$Al(OH)_3 + OH \leftrightarrow Al(OH)_4^- \quad (2.7)$$

$$3Ca^{2+} + 2\ Al(OH)_4 + 8H_2O \leftrightarrow Ca_3Al_2(OH)_4 + 6H_2 \quad (2.8)$$

Stage 1 starts with the breakage of Al-O-Al bonds by the reaction between thin oxide layer on aluminum and water to form AlOOH (Equation 2.5). Al-O-Al forms two Al-OH for each water molecules in the hydrolysis reaction. Then, the hydration proceeds with the formation of aluminum hydroxide ($Al(OH)_3$) (Equation 2.6). The amorphous $Al(OH)_3$ is thermodynamically more stable than Al_2O_3 in hot water and tends to form $Al(OH)_4^-$ ion (Equation 2.7). In stage 2, $Al(OH)_4^-$ ion reacts with Ca^{2+} ions and water, leading to the growth of katoite (Equation 2.8). In stage 3, the hydrogen release is proceeded primarily by the reactions in Equations 2.2, 2.3 and 2.4 since the passive oxide layer on aluminum is dissolved in the solution. As these reactions proceed, the size of aluminum decreases in stage 4 and hydrogen release is discontinued until the aluminum dissolves in the solution [7].

2.2. Microstructure and Mechanical and Thermal Properties of AAC

During hydrothermal process, the green body is strengthened by autoclaving under steam pressure. As a result of autoclaving, nearly one nanometer size tobermorite and crystallized C-S-H are formed as the main binding phases [8]. Besides tobermorite and crystalline C-S-H, xonotlite, jennite and other calcium silicate hydrates may form as secondary phases depending on bulk CaO/SiO_2 ratio, autoclaving temperature and time [9]. Although, autoclaving is essential for the formation of crystalline phases, prolonged autoclaving was reported to inhibit the formation of tobermorite after 8 h [8]. The pore structure of autoclaved aerated concrete (AAC) is composed of several levels of pore sizes between 50 nm and 60 μm [4]. The pores bigger than 60 μm are considered macro pores mainly formed by the expansion of mortar (Figure 2.3(a)). Micro pores are formed

in the vicinity of the cell walls of macro pores (Figure 2.3(b)). And inter-particle pores form on the cell walls, near micro pores (Figure 2.3(c)).

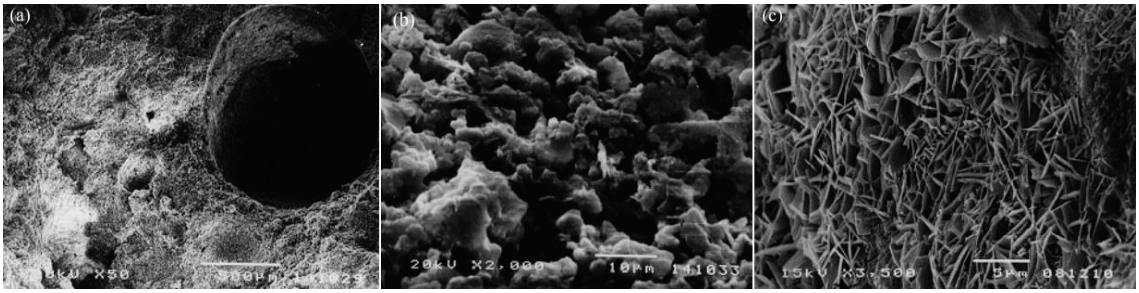

Figure 2.3. Pores in AAC (a) artificial air pore, (b) inter-cluster pore and (c) inter-particle pore (Source: Narayanan and Ramamurthy, 2000)

The method of foaming of AAC determines the microstructure and mechanical and thermal properties. The typical mechanical and thermal properties of AAC is tabulated in Table 2.1 as function of density. As the density increases both compressive strength and elastic modulus increase. The similar increase in thermal conductivity is also seen. As with other ceramic foams, the compressive strength shows a power-law or nearly linear strengthening with increasing density [8, 10].

Table 2.1. The mechanical and thermal properties of AAC (Source: Ergul et al., 2009)

Dry Density (kg m^{-3})	Compressive Strength (MPa)	Elastic Modulus (GPa)	Thermal Conductivity (W m^{-1} K^{-1})
400	1.3-2.8	0.18-1.17	0.07-0.11
500	2.0-4.4	1.24-1.84	0.08-0.13
600	2.8-6.3	1.76-2.64	0.11-0.17
700	3.9-8.5	2.42-3.58	0.13-0.21

The compressive strength of AAC is affected by admixture addition [1]. It was reported that the compressive strength increased with fiber substitutes and the highest compressive strength increase was found in carbon fiber reinforced AAC [12]. In another study, both fracture load and toughness of AAC increased with the increase of Poly-olefin fibrillated fiber content [13]. The presence of fibers prevents the premature fracture and improve the post-cracking stiffness and ductility. The compressive strength of AAC was shown higher than that of short polymer fiber added AC, while the ratio of residual

strength to peak strength of polymer fiber added AC was much higher than that of AAC [14]. Although AAC did not provide much crack resistance under flexural or tensile loading, polymer fiber added AC absorbed high amounts of energy as a result of crack bridging action of fibers (Figure 2.4). The flexural toughness of short polymer fiber added AC was found 100 times higher than of that of AAC due to the role of fibers in bridging the micro and macro cracks.

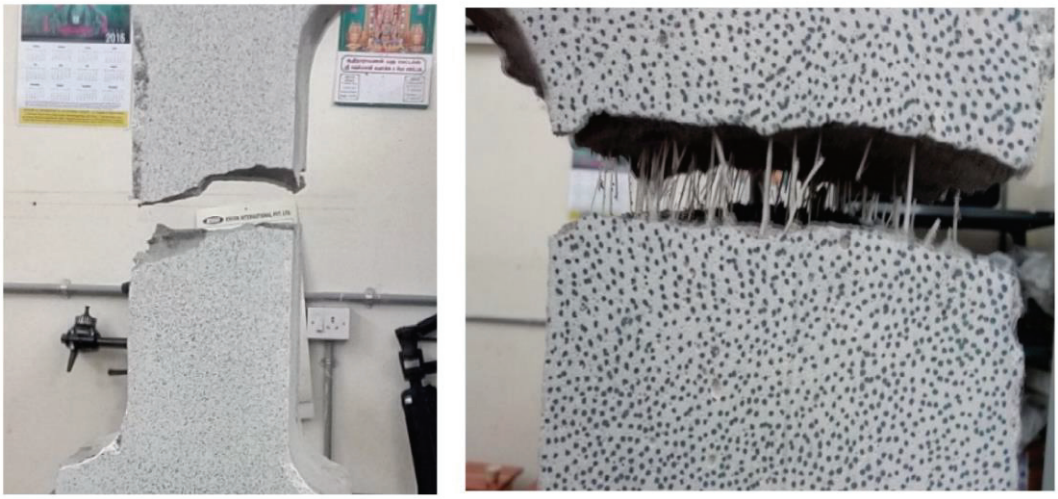

(a) Controls (b) Fiber reinforced specimen

Figure 2.4. The fracture pictures of (a) AC and (b) fiber added AC test specimen showing crack bridging of fibers (Source: Bonakdar et al., 2013)

Moisture content affects the compressive strength of AAC. Aerated concrete usually contains 25-45 wt% water after autoclaving. The compressive strength after autoclaving is lowest; as the water content decreases the compressive strength increases particularly below 10wt% of water (Figure 2.5) [2]. The strength also varies with the direction of applied force. During foaming the bubbles rise normal to slurry surface. The density in the foaming direction, normal to slurry surface, is therefore lower than that of transverse direction, which induces anisotropy in mechanical and thermal properties. The creep behavior of AAC materials is function of the applied stress, moisture content, ambient temperature and relative humidity [5].

The thermal conductivity of AAC becomes important when used as insulator [15]. The heat transfer mainly occurs by conduction, convection and radiation. Thermal conductivity of AAC is influenced by the density and moisture content; ACCs with finer pores have lower thermal conductivities [4].

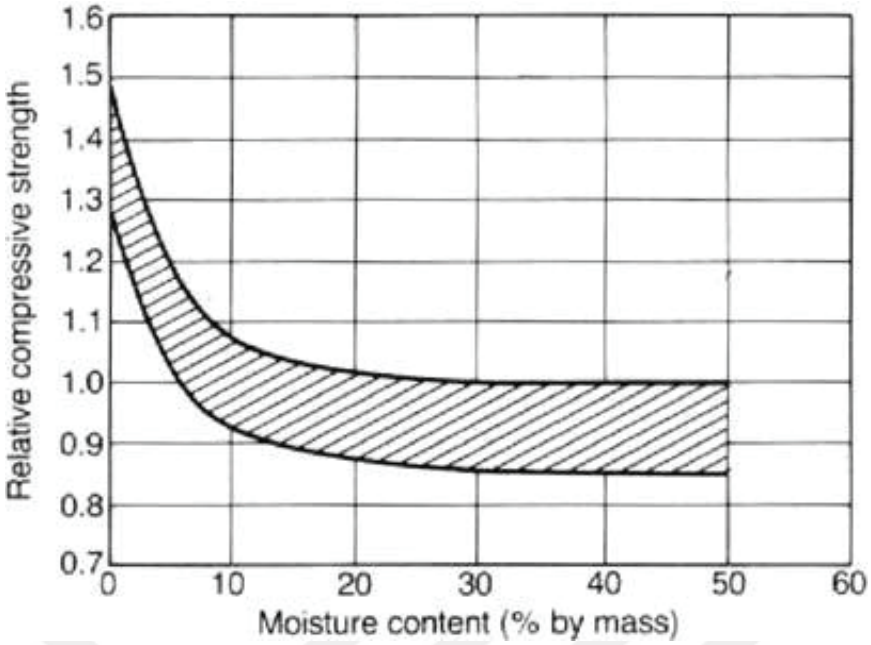

Figure 2.5. The effect of moisture content on relative compressive strength (Source: Scheffler and Colombo, 2005)

CHAPTER 3

MANUFACTURING METHODS AND PROPERTIES OF GLASS FOAMS

3.1. Brief History of Foam and Nodulated Glass Processing

Glass foam production dates back to the 1930s. Long [16] patented "glass product and method of manufacturing sponge-like glass" in 1934. A batch containing silica or sand, alkali metal salts and other metal compounds such as zinc oxide, aluminum hydroxide together with boric acid or borax and carbonaceous materials was melted. The melt was then cooled down to the softening temperature (500-700 ^{o}C) and maintained at that temperature until the spongy glass was formed. In a method patented in 1932, the dissolved air or gas in molten glass was drawn out by applying vacuum (Figure 3.1(a)) [17]. This induced a porous structure after solidifying the vacuumed glass melt contained gas bubbles. The foam glass produced by this method was reported inhomogeneous in pore size and porosity distribution. In order to obtain relatively homogeneous pore size and porosity distribution, a gas forming agent such as SiC powder was mixed with molten glass inside a mold; then, the air surrounding the mold was evacuated (Figure 3.1(b)) [18]. The decomposition of SiC powder resulted in the release of CO_2 which expanded the molten glass. The evacuation of air facilitated the growth of gas bubbles in the molten glass.

The foam glass processing using ground glass or glass powder was patented in 1934 [19]. The ground glass powder was mixed with a foaming agent powder, and then powder mixture was heated to the softening point of glass powder (Figure 3.1(c)). The sintering of glass particles enclosed foaming agent powder and prevented the escape of the gas formed by the decomposition of the foaming powder. Heating to a higher temperature to the decomposition temperature of foaming agent powder expanded the softened glass powder. Diatomaceous earth powder which contained air inside nano-porous frustules was also used as foaming powder agent [20]. The density of the foam glass processed by this method ranged 350-400 kg m^{-3}. In order to reduce the density of foam

glass, porous vermiculate or diatomaceous earth powder (1-8 wt%) was added to ground window glass and foaming agent ($CaCO_3$ (0.5-2 wt%)) powder mixture [21]. The mixture was heated to 650 ^oC to sinter the glass particles and then to 815-912 ^oC to decompose $CaCO_3$ into CO_2 and soften the glass sufficiently to permit the decomposition gas to expand. The vermiculate or diatomaceous earth remained unchanged and embedded in the cell walls (Figure 3.1(d)). In order to increase resistance to water and water vapor at elevated temperatures, flint (10-40 wt%) was added to the mixture of glass and foaming agent powder. During heating, the flint entrapped into the foam glass cell walls without interacting with glass and foaming agent powder.

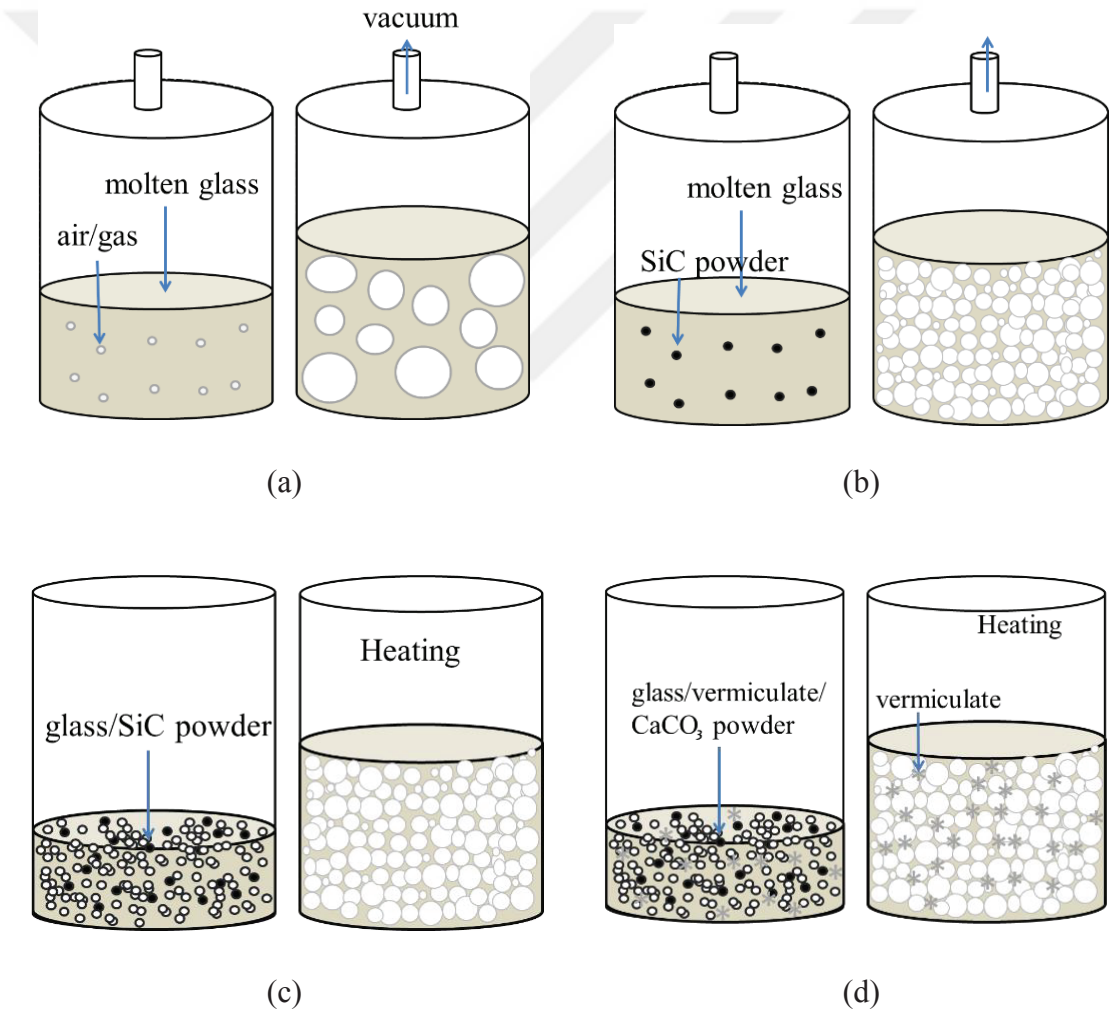

Figure 3.1. Foam glass processing (a) vacuuming molten glass, (b) mixing molten glass with foaming agent powder, (c) heating glass powder/foaming powder agent and heating glass powder and foaming agent powder with (d) vermiculate

Nodulated cellular glass and method of forming were patented in 1954 [22]. The soda lime glass or borosilicate glass powder was pulverized in a ball mill with 0.1-2 wt% carbonaceous foaming agent powder (e.g. carbon black, coal or coke) (Figure 3.2(a)). The pellets or nodule were then formed using the pulverized glass and foaming agent powder mixture and a suitable binder (water, urea solution or colloidal silica solution) in a briquetting machine. The pellets were then heated in furnace to give cellular nodular structure. Heating consisted of two stages: 1) sintering the glass powders in the pellets at 700-787 ^{o}C and 2) foaming the pellets at 871-926 ^{o}C. The process yielded cellular nodules in various diameters with dense outer skins. Alternatively, the ball milled glass powder-foaming agent mixture was sintered together to give sintered glass powder masses (Figure 3.2(b)). Then, the sintered glass powder mass was crushed in a crushing machine. The sorted sintered glass masses were then foamed in a rotary furnace to obtained cellular glass nodules.

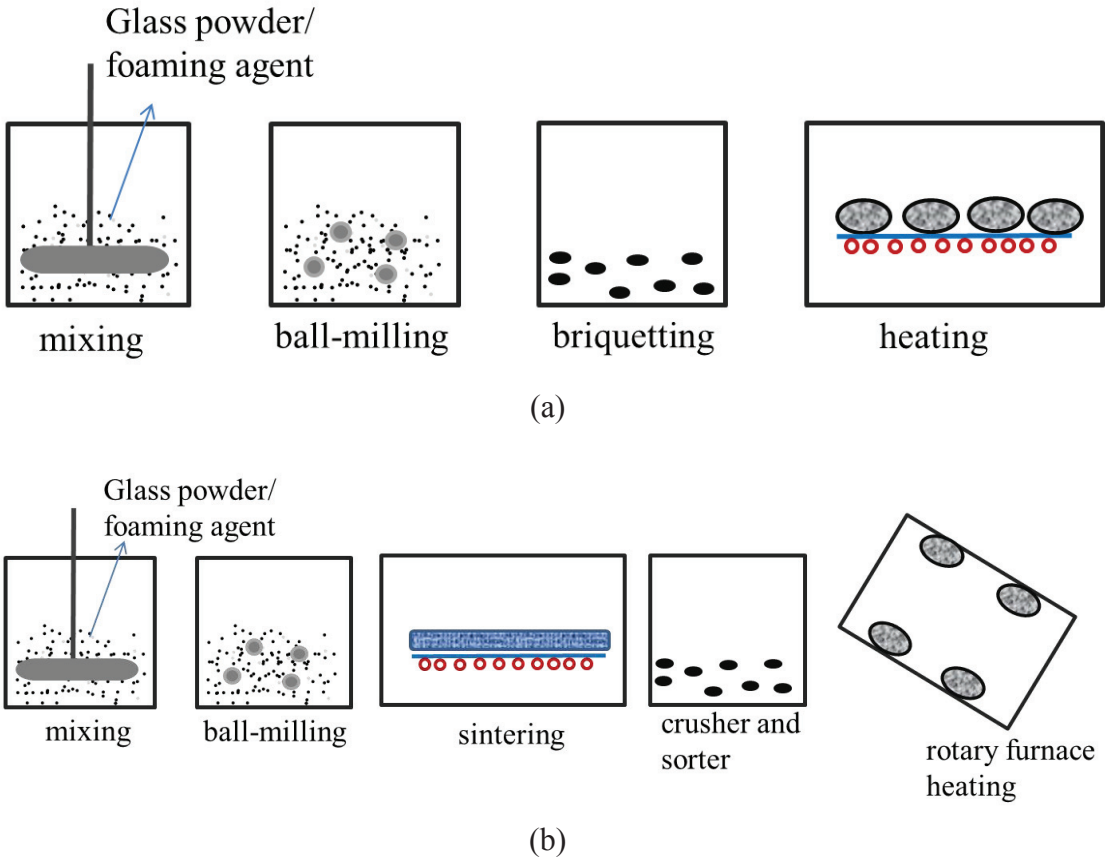

Figure 3.2. Nodulated cellular glass and method of forming based on (a) briquetting and (b) crushing sintered powder mixture

3.2. Current Foam Glass and Granule Processing

Currently glass foams are produced by several companies. The properties of commercial foam glass products and trade names are tabulated in Table 3.1. Glass foam are either available in block form for thermal insulation or in aggregate/granules form for filling or sound insulation. The properties listed in Table 3.1 indicates that the important properties of glass foams which include lightweight, rigid, thermally insulating, freeze-tolerant, nonflammable, chemically inert and nontoxic, insect and bacteria resistant and water resistant. These special properties make glass foam beneficial for construction applications such as insulation of roofs, walls and floors [2]. The density of glass foams ranges 105-500 kg m^{-3}. As also noted in Table 3.1, the block form of glass foam has no water absorption property.

Table 3.1. The properties of commercial foam glass products
(Source: Scheffler and Colombo, 2005)

Properties	Pittsburgh Corning	Pittsburgh Corning	Cell-u-Foam	Misapor	Millcell	Liaver	Liaver	Geofil Bubles
	Wallboard Block	Foamglass F Block	Ultra-Cuf 1031 Block	Loose aggregate 10 - 50mm	Loose aggregate	Reapor sound insulation	Glass Granules 2 -4mm	Glass Granules 2- 25mm
Specific Heat (kj/kg.K)	0.84	0.84	0.83					
Thermal Diffusivity (m^2/s at 0°C)	4.4 x 10^{-7}	3.5 x 10^{-7}	4.9 x 10^{-7}					
Product density (kg/m^3)	105	165	128	225	100 to 300	290	300 to 500	450 to 1850
Bulk Density (kg/m^3)						190		250 to 1100
Porosity (%)						85-86		14-50
Water absorption (m%)	0	0	0			50-60		0.1-55
Hygroscopicity	0	0	0	0				
Permeability	0	0	0	0				
Capillarity	0	0	0					
Surface water adhesion (m^{-3})				70 l/				
Fire	Non-combustible			V1 (DIN A1)	Non-Combustible			

Specifically formulated pristine glasses were used to produce glass foams in 1930s. However, this process was more expensive than currently used methods due to the glass type used and the high sintering temperatures. Today, waste glass or cullet is commonly used for glass foam production. The amount of waste glass generation annually in 1998 was reported about 0.9 million tons in EU and 1.98 million tons in Japan [23]. About 74% of the container glass production was used as waste glass in Japan [23]. The cullet generation was estimated 0.5 million ton per year in UK [24]. A study reports that only 20% of the collected waste glass are returned to glass factories for re-melting [25]. The current waste glass-based foam glass manufacturing seems to be one of the most economical ways of recycling large quantities of waste glasses generated. Recycling of glass products such as container and flat glasses, borosilicate glasses, and fluorescent lamp glass can generate different types of waste glasses. The mixture of pristine glass and waste glass can also be used together in glass foam production [2].

The composition of glass cullet in different countries are tabulated in Table 3.2. Despite small variations between glass cullet of different countries, on the average they have 70% SiO_2 and 14% Na_2O as major compounds. In addition to waste glass, fly ash, which is produced as a by-product of the coal combustion, is also used in glass foam production [26-28]. Cathode ray tubes (CRTs) in televisions and computer display monitors include 50-85 wt% glass. Cathode ray tubes are valuable sources as a recycling glass material [29-30]. The composition of the CRTs is further tabulated in Table 3.3. Cathode ray tubes contains lesser amount of SiO_2 and Na_2O and additional compounds such as PbO.

Table 3.2. The composition of container and sheet glass cullet in different countries (Source: Bobkova et al., 2007)

	Mass Content								
Country	**SiO_2**	**Al_2O_3**	**Fe_2O_3**	**CaO**	**MgO**	**Na_2O**	**K_2O**	**SO_3**	**MnO**
USA	71.36	0.79	0.12	8.89	0.32	15.38	0.62	0.51	-
Holland	70.92	2.26	0.27	11.41	1.50	12.78	1.04	-	-
Scotland	70.18	2.59	1.25	9.30	0.86	14.07	0.68	0.26	0.13
France	70.40	1.80	-	9.60	1.20	15.00	0.20	-	-
Japan	73.30	2.11	0.10	7.43	0.48	17.50	0.82	-	-
Germany	69.90	1.15	1.29	10.47	1.04	15.01	0.37	0.53	-

Table 3.3. CRT glass compositions in wt%
(Source: Bobkova et al., 2007)

Compound	Black and White Glass		Color Screen Glass		Color Funnel Glass	
	Range	Standard Content	Range	Standard Content	Range	Standard Content
Network Formers						
SiO_2	64-66	65	60-63	62	52-56	52
Sb_2O_3	0.3-0.6	0.45	0.25-0.50	0.35	0.1-0.3	0.25
ZrO_2	0-0.5	0.25	0-2.5	1.5	-	-
As_2O_3	0-0.3	0.25	0-0.2	0.02	0-0.1	0.01
Intermediaries						
Al_2O_3	3-5	3	2-3.5	2.2	3.5-5	4
PbO	2.8-4.4	4	0-3	-	19-23	22
ZnO	0-0.1	0.05	0.4-0.6	0.5	0-0.1	0.05
TiO_2	0.1-0.2	0.15	0.4-0.6	0.5	0-0.1	0.05
Network Modifiers						
Na_2O	6.5-8	7	7.8-9	8	6-8	6.8
K_2O	6-7.5	7	6-7.5	7.5	7.5-8.5	7.8
Li_2O	0-0.6	0.3	0-0.5	0.2	0-0.1	-
CaO	0-1	0.5	0-2	0.5	2-4	3.8
MgO	-		0-1	0.2	1.2-2	1.8
Fe_2O_3	0.05-0.2	0.12	0.07-0.12	0.08	0.05-0.07	0.06
SrO	0-2	1	6-10	8.5	0-1	0.5
BaO	9-12	11	9-11	10	0-2	1
CeO_2	0.1-0.2	0.18	0.2-0.3	0.25	-	

3.3. Foaming Agents

Foaming agents are grouped in two types. The foaming agents decompose upon heating and release a gaseous product (CO_2) are grouped as *neutralizers.* The examples include $CaCO_3$ and $CaMg(CO_3)_2$. The foaming agents which form gaseous products of CO_2, CO or N_2 depending on the composition of the used foaming agent through reacting with glass are classified *redox* agents. The examples of redox agents are C, SiC and Si_3N_4 [32]. The reactions of various foaming agents are tabulated in Table 3.4.

Various types of glass powders and blowing agents were previously investigated for the processing of foam glass. The glass particles polishing wastes containing SiC

particles were used as blowing agent for foaming soda-lime glass powder [33] and the powder mixture of soda-lime glass and glass fiber [34]. The glass cullet mixed with 20 wt% fly ash was foamed using marble polishing plant sludge (mainly composing of calcite and dolomite) and using SiC as blowing agent [28]. The dismantled waste CRT glasses were foamed using $CaCO_3$, SiC and TiN as blowing agents and hydrothermal hot-pressing [35-41]. Borosilicate glasses were reported to be effectively foamed using SiC and Si_3N_4 over a wide range of temperatures [42]. Water and liquid hydrocarbons were further investigated as blowing agents in foam glass processing; the latter were recommended to retard the effect of combustion reaction rate [43-44].

Table 3.4. Foaming agents and their decomposition reactions

Foaming Agent	Decomposition Reaction
Dolomite $CaMg(CO_3)_2$	$CaMg(CO_3)_2(s) \rightarrow CaCO_3(s)+MgO(s)+CO_2(g)$ $CaCO_3(s) \rightarrow CaO(s)+CO_2(g)$
Carbon	$C(s)+O_2(g) \rightarrow CO_2(g) \rightarrow$ $2C(s)+O_2(g) \rightarrow 2CO(g)$
SiC	$SiC(s)+ O_2(g) \rightarrow SiO_2(s)+CO_2(g)$ $SiC(s)+MnO_2(s) \rightarrow SiO_2(s)+MnO(s)+CO_2(g)$
Si_3N_4	$Si_3N_4(s)+3O_2(g) \rightarrow 3SiO_2(s)+N_2(g)$ $Si_3N_4(s)+MnO_2(s) \rightarrow 3SiO_2(s)+MnO(s)+N_2(g)$
AlN	$4AlN(s)+3O_2(g) \rightarrow 2Al_2O_3(s)+2N_2(g)$ $4AlN(s)+3O_2(g) \rightarrow 2Al_2O_3(s)+MnO(s)+2N_2(g)$

3.4. Foaming Kinetics and Mechanical Properties

It was shown that there existed a relationship between the particle size distribution of glass powder to be foamed and the pore size and density of the foam glass [2]. The pore diameter increased with the increase of the glass powder particle size as shown in Figure 3.3 for a glass foam foamed using 5 wt% SiC. The foaming temperature increased cell size at the same final foaming time (Figure 3.4) [45].

The apparent density of foamed glass was also shown to increase with increasing glass powder particle size [46]. Figure 3.5 shows the effect of mean glass particle size and heating rate on the apparent density of foam glass. Both mean particle size and heating rate increase the apparent density.

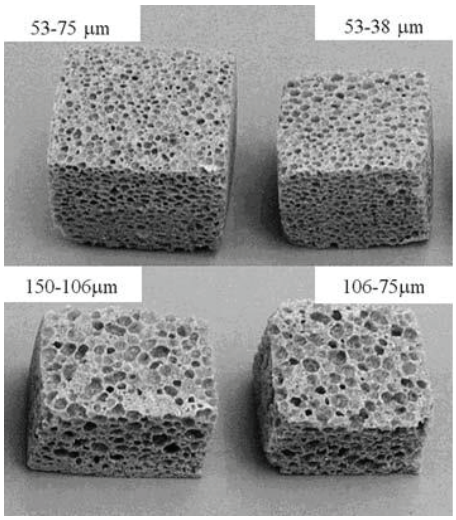

Figure 3.3. The influence of glass powder particle size on the microstructure of a glass foam foamed with 5 wt% SiC foaming agent
(Source: Scheffler and Colombo, 2005)

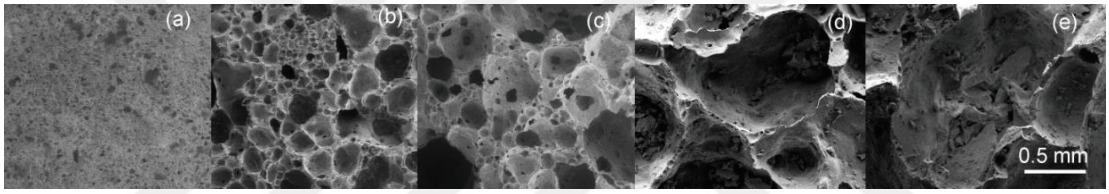

Figure 3.4. The pictures of cells of foam glass processed at (a) 750 (b) 800, (c) 850, (d) 900 and (e) 950 ºC (Source: Attila et al., 2013)

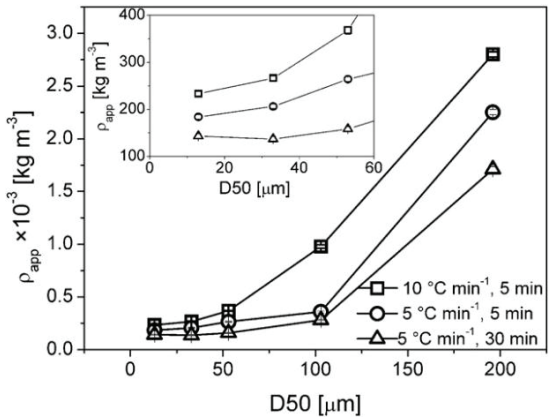

Figure 3.5. The effect of particle size (D50) on the apparent density of foam glasses prepared at same temperature with different heating rate
(Source: König et al., 2016)

The foam glass foaming and its cellular structure evolution may be considered composing of several consecutive stages [45]. Figure 3.6(a) shows the volume expansion-

temperature and volume expansion-time graphs of foamed glass compacts heated to 900 ^{o}C. In Region 1 of Figure 3.6 (a), the glass powder sintered as the compact temperature increased and slight expansion in this region was due to the thermal expansion of the compact. The expansions of the glass powder compacts started at the temperature between 670 and 680 ^{o}C when the glass powder was melted in Region 2. The volume expansion reached a maximum value at about 866-872 ^{o}C. The expansion in Region 3 was nearly constant and thereafter decreased slightly in Region 4 as the temperature of the foamed compact reached the temperature of the furnace. The transition from Region 1 to Region 2 indicated the temperature at which the glass powder transformed partially or completely into a viscous liquid. Although the decomposition of the blowing agent started before the softening of glass particles, the sintering of the particles through neck regions prevented the escape of the gases before the melting of the glass powder, causing the rapid expansion of the briquette upon the sintering and/or partial melting of the glass particles. Figure 3.6(b) shows the volume expansion-temperature and volume expansion-time curves of glass powder briquettes heated to the final temperatures between 700 and 900 ^{o}C with different heating rates. The heating rate as seen in this figure increased the maximum expansion. The slow heating lead to early release of the gas from the foaming agent before the viscosity of the glass was low enough to allow the glass to expand rapidly [42].

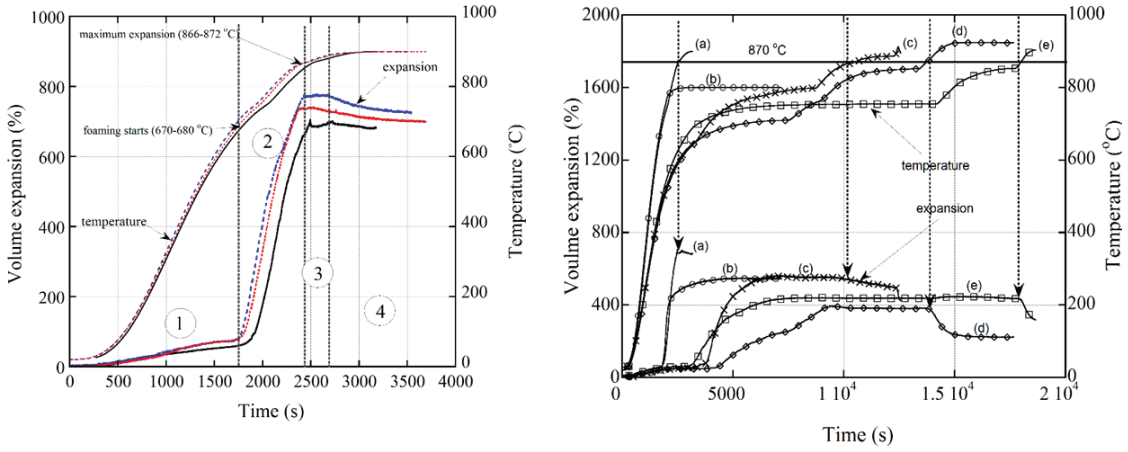

(a) (b)

Figure 3.6. The volume expansion-time and temperature-time graphs of (a) three glass powder compacts heated with the same rate and (b) glass powder compacts heated to different temperatures with different heating rates, the numbers corresponding to the different stages of compact expansion (Source: Attila et al., 2013)

3.5. Mechanical Properties of Glass Foams

Glass foams show typical stress-strain behavior of other brittle foams. In compression, they show catastrophic failure following a maximum or collapse stress [10]. The collapse stress of brittle cellular structures is given as [10]

$$\sigma_f=\sigma_s\left[C\sigma\varphi\rho_{rel}^{\frac{3}{2}}+(1-\varphi)\rho_{rel}\right] \tag{3.1}$$

where, σ_s is the strength of glass, C is a constant, ρ_{rel} is the relative density of foam and ϕ is the volume fraction of the solids contained on plateau borders [47]. The relative density is $\frac{\bar{\rho}}{\rho_s}$, where $\bar{\rho}$ is the density of the foam and ρ_s is the density of the solid. The values of C is given as 0.2. The value of φ is given as [10]

$$\varphi=1-\frac{3t(l-2W_p)^2+6t\sqrt{3}(l-(2/\sqrt{3})W_p)^2}{11.31l^3\rho_{rel}} \tag{3.2}$$

where l, W_p, and t are the cell wall length, plateau border thickness and cell wall thickness, respectively (Figure 3.7).

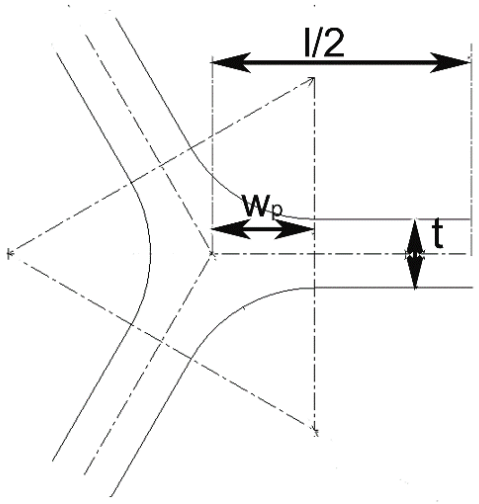

Figure 3.7. Geometry of the cross-section of a tetrakaidecahedral cell edge with plateau borders (Source: Gibson and Ashby, 1997)

Figure 3.8 shows the experimental and Equation 3.1 (glass collapse stress was taken 70 MPa) collapse stresses as function of density [45]. It was shown that the

experimental collapse stresses of glass fall between φ values of 0.7 and 1 for the foam densities up to 300 kg cm^{-3} and between 0.7 and 0.9 above the foam density of 300 kg cm^{-3}. This confirmed that glass foams exhibited near open cell foam behavior. This was attributed to relatively thicker cell edges. Results from the literature are also provided for comparison. These results are taken from the references 1-[48], 2-[48], 3-[24], 4-[49], 5 -[50], 6-[51],7-[28],8-[34], 9-[52],10- [53], 11-[54],12[45], respectively.

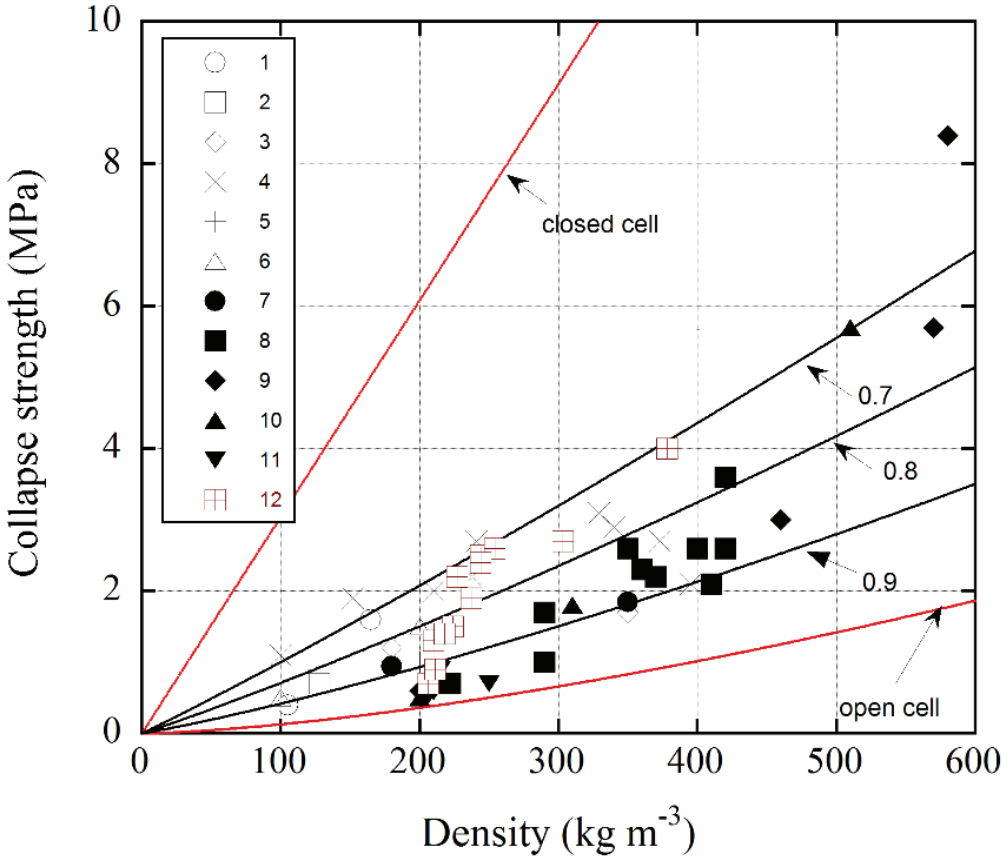

Figure 3.8. The fitting of glass foam compressive strength with Equation 3.1

The compressive strengths of the glass foams prepared using SiC or TiN at 750-850 °C for 60-120 min varied between 4 to 267 MPa depending on their porosity as seen in Figure 3.9 [38]. A similar effect of porosity is also seen on flexural strength, as the porosity increased flexural strength decreased. In another study, it was shown that the amount of foaming agent initially decreased compressive strength and then increased the compressive strength as seen in Figure 3.10 [39]. The effect of cell size on the tensile, compressive and bending strength of glass foams were also investigated [55]. The results revealed that the strength of glass foams increased for small cell size samples.

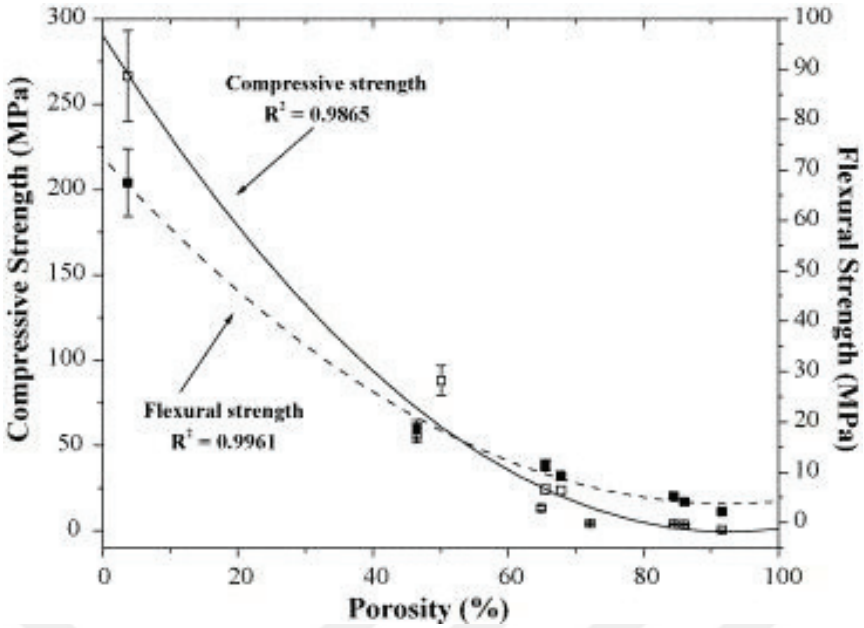

Figure 3.9. Compressive and flexural strength vs. porosity of different samples (Source: Mear et al., 2007)

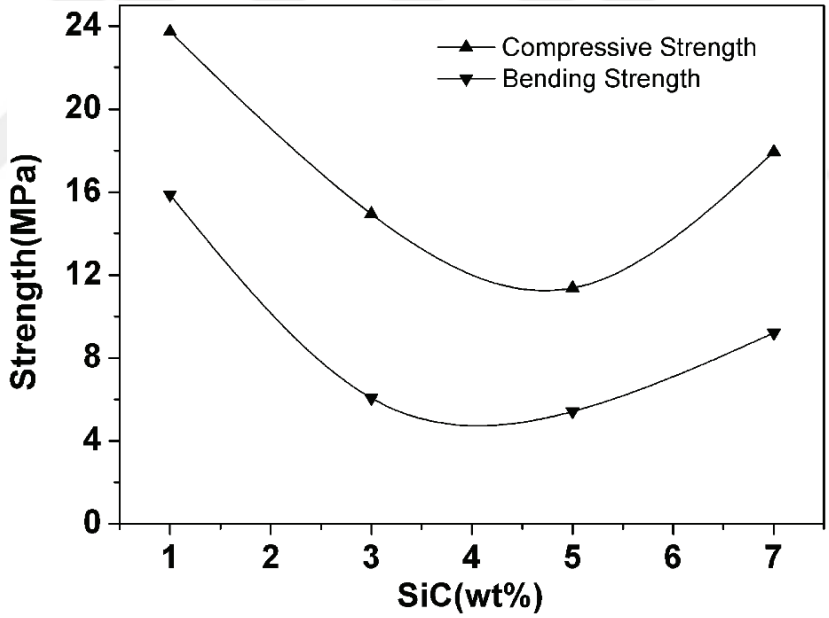

Figure 3.10. Compressive and bending strength as function of SiC amount (Source: Guo et al., 2010)

3.6. Thermal Conductivity of Glass Foams

The thermal conductivities of the glass foams as function of density were reported in the current literature [31, 38, 48, 50]. The thermal conductivities of glass foams increased

with increasing foam density and varied between 0.048 and 0.079 W K^{-1} m^{-1}. For the foam densities ranging between 100 and 200 kg m^{-3}, the conductivities were between 0.04 and 0.05 W m^{-1} K^{-1}. Usually, closed-cell foams have lower thermal conductivity. It was reported that foaming agent affected the thermal properties of glass foams [56]. Thermal conductivity of sintered and melt-quenched glass foams of CRTs foamed using MnO_2 and Fe_2O_3 increased with increasing wt% of foaming agent (Figures 3.11(a) and (b). The effective thermal conductivity (λ_{eff}) is given as

$$\lambda_{eff}=\alpha\ \rho\ C_p \tag{3.3}$$

where, α is the thermal diffusivity, ρ is the bulk density and C_p is the heat capacity. The thermal conductivity of melt quenched, and sintered samples provided upper and lower limits.

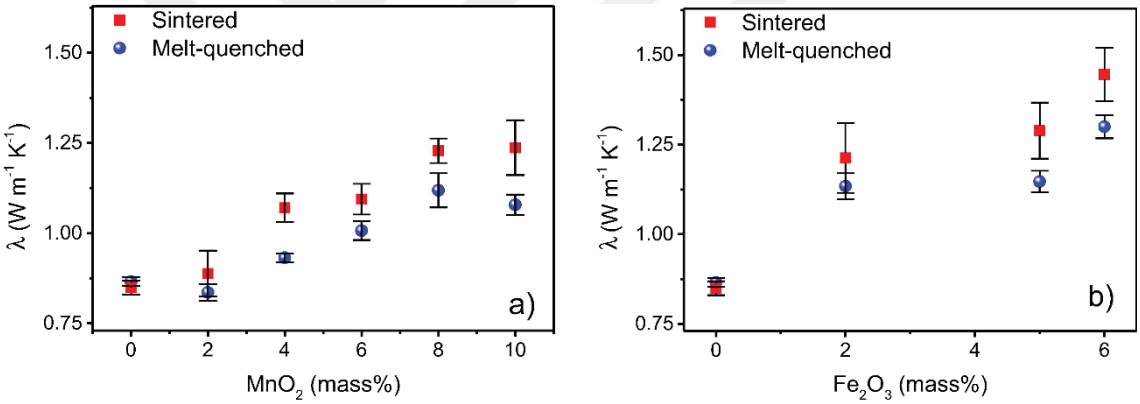

Figure 3.11. Thermal conductivity of sintered and melt-quenched samples with different foaming agents and amounts (Source: Østergaard et al., 2017)

3.7. Current Situation in Glass Foams

There are approximately 170 scientific articles published in the literature. However, the total number of patents related to manufacturing of glass foams is 390 until 2015 which implies the importance of need for new methods. Figure 3.12 the number of foam glass related patent publications comparing total publications and publications of countries between 1930 and 2015. In the period of 1930 and 2015, total 161 patents were published by the USA, 135 patents by China, 31 patents by European countries, 25 patents

by Japan and 38 by Russia (Figure 3.13). The patent publications by China started in 1990s and gained an increase after 2000s.

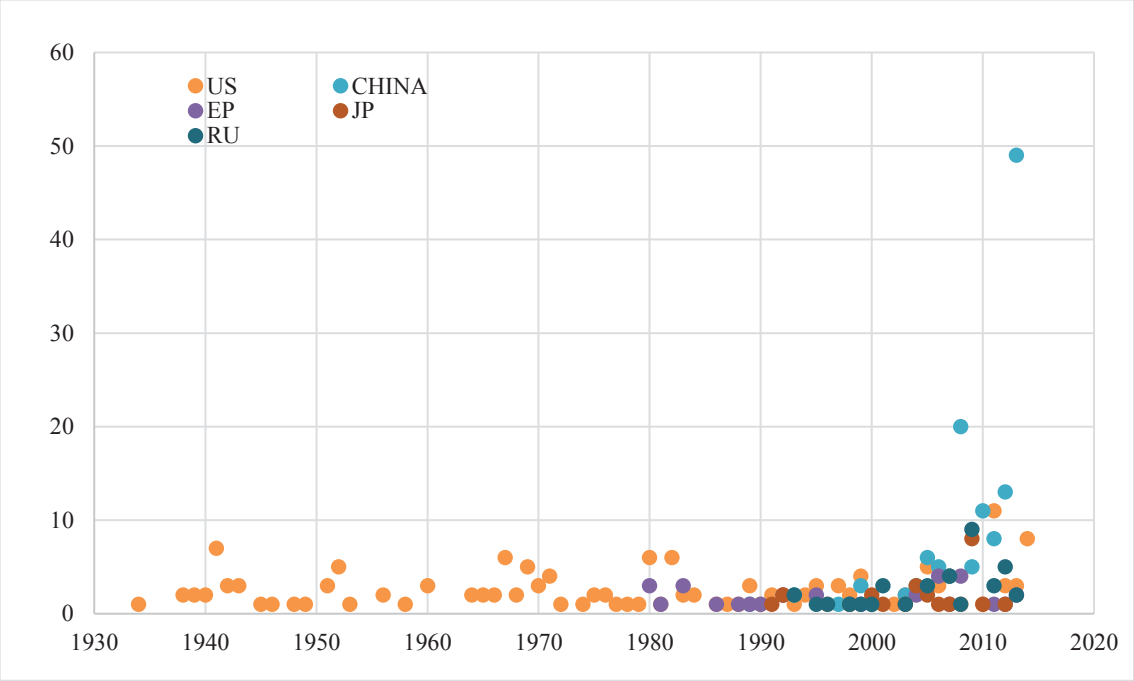

Figure 3.12. Number of foam glass related patent publications

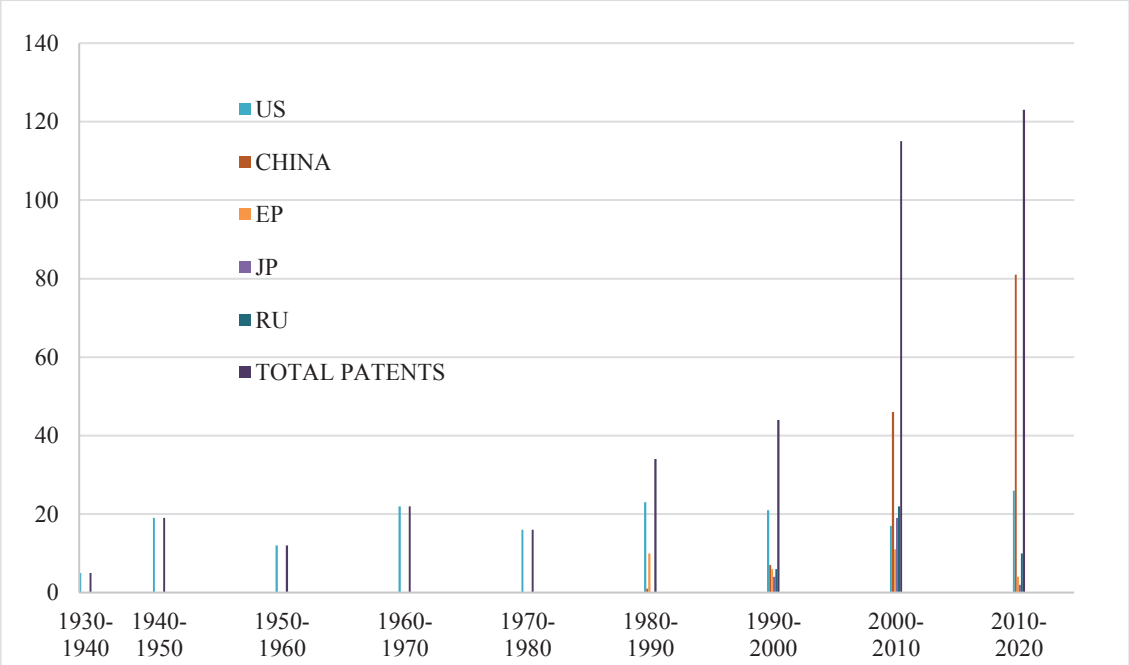

Figure 3.13. Number of foam glass related patent publications comparing total publications and publications of countries

CHAPTER 4

FOAM STABILITY

4.1. Background of Cellular Structures

Belgian Physicist Joseph Plateau formulated the structure of soap films in 1873. Plateau showed that each bubble has constant mean curvature, triples of surfaces meeting along curves at 120^o angles and these curves meet in groups of four at equal angles. The last rule was mathematically proved by Taylor in 1976 on the stability of foams [57]. The properties of cellular solids, which can be made of polymers, metals or ceramics, are dependent on the properties of their solid structure, the topology and shape of the cells and relative density [2].

The foams containing relatively low amount of liquid are called dry foam. It consists of polyhedral cells with curved walls (Figure 4.1). As opposite, wet foams accommodate a high amount of liquid and hence the bubbles are spherical and behave like a liquid. Consequently, wet foams do not support shear forces. Draining out liquid phase from cell walls due to gravitational and capillary forces transforms a wet foam into a dry foam [57-58].

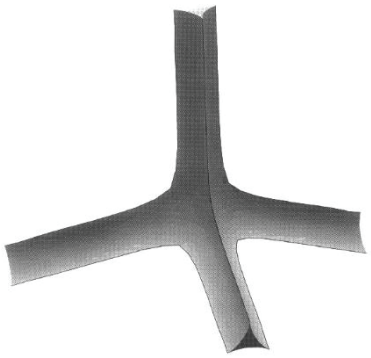

Figure 4.1. Tetrahedral vertex at the intersection of four Plateau borders
(Source: Waire and Phelan, 1996)

Gas bubbles induce the cell formation in a foam structure and, the main components of cells are the cell walls, Plateau borders and nodes. The intersections of cell walls are the Plateau borders and the intersections of the Plateau borders are the nodes

as seen in Figure 4.2. The cell geometry depends on two conditions. The internal energy and internal surface should be as small as possible and the gathering of cells has to be space filling [58]. The cell wall thickness in foams varies between 10^{-9} and 10^{-4} m depending on the prevailing stabilization mechanisms. In aqueous foams, the dry cell wall thickness is typically 10^{-9} m, forming the lower limit for cell wall thickness. As seen in the radioscopy picture of an aluminum foam in Figure 4.3, nearly all liquid is located on the Plateau borders in dry foam [58]. The thicker white lines in the same figure represent the Plateau borders, while cell faces are not clearly seen as they are very thin.

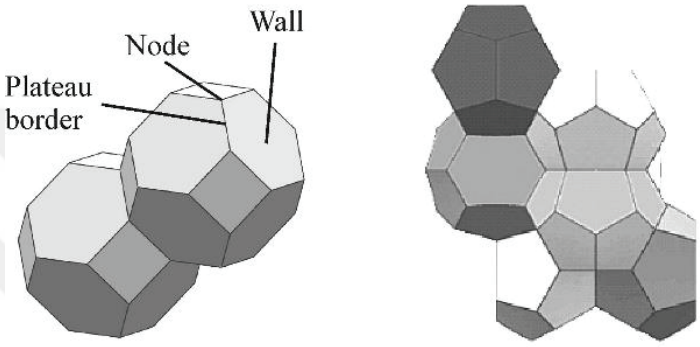

Figure 4.2. Cell parts: Left Tetrakaidecahedra cell with walls, right: Weaire-Phelan cells (Source: Koerner, 2017)

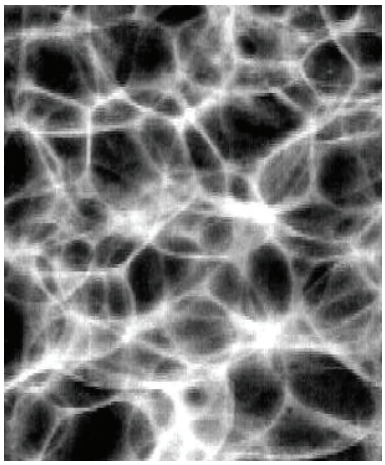

Figure 4.3. Radioscopy of aluminum foam showing Plateau borders (Source: Koerner, 2017)

Foaming by in-situ gas generation proceeds with several sequential/simultaneous stages. These stages are shown in Figure 4.4 for a foamable Al compact which contained a foaming agent in it. Upon heating, the compact is melted, and the foaming agent

decomposes and releases gases. At this early stage, the compact is expanded by the nucleation of gas bubbles. As expansion continuous, the formed gas diffuses into the bubbles, increasing the amount of gases in the bubbles and resulting in growth of bubbles. Later, these stages are followed by the stages of the combination of coarsening and decay. Coarsening is due to the growth of larger bubbles at the expense of smaller ones. This may be reason of pressure differences between two adjacent bubbles or simply due to rupture of the cell wall of two adjacent bubbles. Decay occurs mostly by drainage which is the downward flow of the liquid metal through the cell edges due to gravitational forces. Drainage results in formation of thick dense layer of liquid metal at the bottom and cells with thicker walls in the middle [59]. Particulate addition to the foams is known to have a stabilizing effect. The presence of particles on the cell walls increases the viscosity of the liquid; therefore, tends to reduce the liquid metal flow.

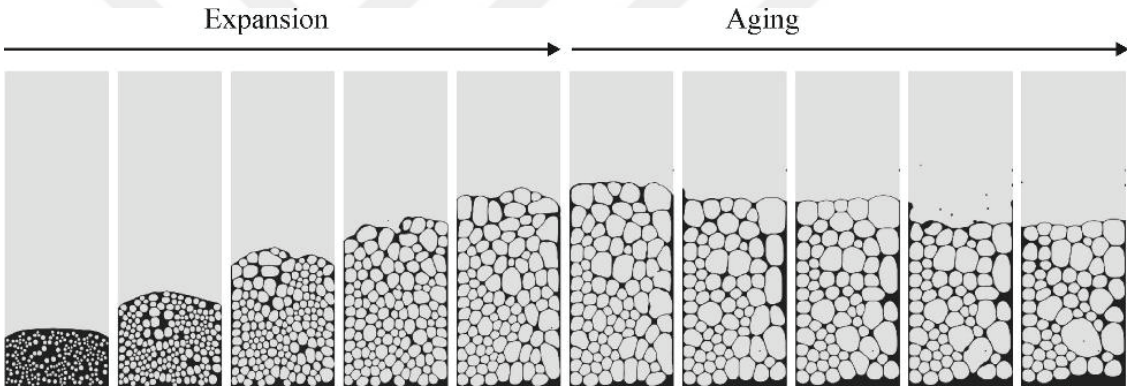

Figure 4.4. Foaming stages: nucleation, growth, coarsening and decay
(Source: Koerner, 2017)

Foam is a two-phase system of fluid and gas phase. The dynamics of gas phase may be neglected due to the large density difference between liquid and gas phase. The dynamics of an incompressible fluid is shown by Navier-Stokes equations [60]. In these equations, mass and momentum conservation are expressed as

$$\partial_\alpha \vartheta_\alpha = 0 \tag{4.1}$$

$$\partial_t \vartheta_\alpha + (\vartheta_\beta \partial_\beta)\vartheta_\alpha = -\frac{1}{\rho}\partial_\alpha p + v\partial_\beta^2 \vartheta_\alpha + g_\alpha \tag{4.2}$$

where, ρ is the density, ϑ is the velocity, p is the pressure, v is the viscosity and g is the gravitational acceleration [58, 60]. The gas pressure (p_i) in the bubble is

$$p_i = \frac{n_i R\, T}{V_i} \tag{4.3}$$

where, R is the ideal gas constant, n_i is the mole of gas, T is the temperature and V_i is the volume of bubble. The momentum transfer between gas and liquid phase occurs at the gas-fluid interface (Γ). At the interface, the velocities of fluid (ϑ_f) and gas (ϑ_g) equal

$$\vartheta_f(x) = \vartheta_g(x),\ \forall x \in \Gamma \tag{4.4}$$

The force balance at the fluid-gas interface is shown in Figure 4.5. The gas pressure at the interface is balanced by the capillary pressure, fluid pressure and viscous forces. Since the gas has only normal forces, the boundary conditions split into two components, normal and tangential component, as

$$p - 2\rho\vartheta\partial_n\vartheta_n = p_i - 2\sigma K \tag{4.5}$$

$$\partial_n\vartheta_t + \partial_t\vartheta_n = 0 \tag{4.6}$$

where ϑ_n and ϑ_t are the normal and tangential component of velocity. The term in Equation 4.5, $2\sigma K$, is the capillary pressure. K is average curvature and σ is the surface tension [60].

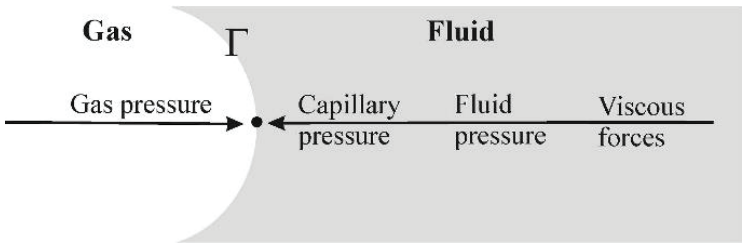

Figure 4.5. Force balance at the fluid-gas interface
(Source: Koerner, 2017)

The expansion kinetics of an isolated bubble with radius R in an incompressible liquid with a pressure of p_0 is given by the Rayleigh equation as

$$\rho R\ddot{R} + \frac{3}{2}\rho\dot{R}^2 + 4\rho v\frac{\dot{R}}{R} + \frac{2\sigma}{R} = p_i - p_0 \tag{4.7}$$

$$(\dot{R}=\frac{dR}{dt},\ \ddot{R}=\frac{d^2R}{dt^2}) \tag{4.8}$$

where p_i is the bubble pressure, R is the bubble radius, $\rho R\ddot{R}+\frac{3}{2}\rho\dot{R}^2$ is the inertial pressure, $4\rho v\frac{\dot{R}}{R}$ is the viscous pressure, $\frac{2\sigma}{R}$ is the capillary pressure and p_i-p_0 is the bubble overpressure. Equation 4.7 indicates that inertial, viscous and capillary pressure play a great role for the expansion of a single bubble. The bubble volume growth rate ($\dot{V}$) is

$$\dot{V}=4\pi R^2\dot{R}, \text{ where } \dot{R} \text{ is constant} \tag{4.9}$$

The time to reach the final radius (t_f) is

$$t_f=\frac{R_f}{\dot{R}} \tag{4.10}$$

Considering a single bubble in a fluid, the bubble rises due to gravity and achieves a stationary velocity of ϑ. At this velocity, drag force and buoyancy reach equilibrium and the velocity is given by Stokes' law as

$$\vartheta=\frac{gR^2}{3v} \tag{4.11}$$

where, *g* is the gravity constant. While bubbles are expanding and moving, bubble-bubble interactions occur (Figure 4.6, gray scale indicates the velocity field).

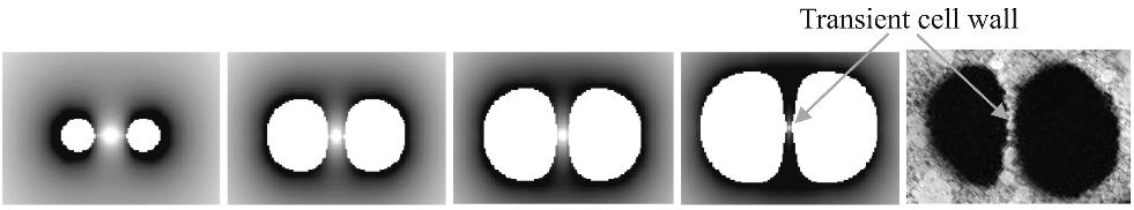

Figure 4.6. Transient cell wall formation
(Source: Koerner, 2017)

Because of the velocity field of two expanding bubbles, the bubbles become deformed asymmetrically during the expansion (Figure 4.6). The surface tension and viscosity of liquid and the growth velocity and size of bubbles determine the formation of transient cell walls [58].

Drainage due to capillary forces affects the cell wall thickness. The pressure difference between cell walls and Plateau borders induces a fast cell wall thinning. As seen in Figure 4.7, the Plateau borders are under lower pressure (-) and the cell walls are under over pressure (+), which drains the liquid from cell walls [58, 60].

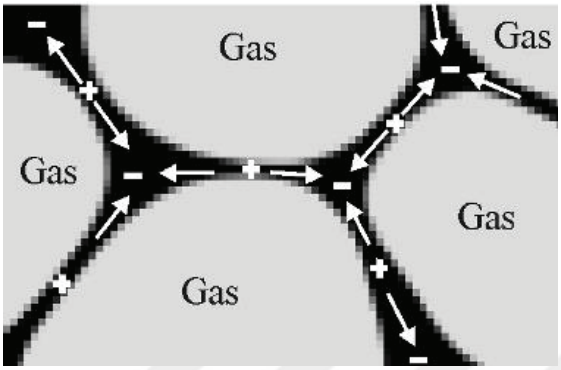

Figure 4.7. Drainage in cell walls
(Source: Koerner, 2017)

4.2. Foam Stability

Thermodynamically, foams are unstable due to high interfacial energy. Kinetically, foams are grouped in two types. These are unstable/transient and metastable/permanent foams. In unstable foams, surfactants or particles prevent drainage, and foam formation is resulted from Gibbs-Marangoni effect [58]. If there are not external disturbances, evaporation, vibrations, temperature gradients or diffusion of gas, foam is stable infinitely [58]. In metastable foams, the cell wall thinning time is shorter than its lifetime.

Particles increase foam stability. For instance, silica particles stabilize aqueous foams without surfactant molecules [61]. Particles to be added may be spherical, oblate and cylindrical in shape and have irregular surface roughness as shown in Figures 4.8(a) and (b). The foam stabilization may be achieved by the particles absorbed at the interface (Figure 4.8(c)), distinct hydrophilic particles aggregated or gelified particles in the foam channels (Figure 4.8(d)), aggregated particles adsorbed at the interfaces (Figure 4.8(e)) and in the bulk and large aggregates or individual particles in Plateau borders (Figure 4.8(f)) [62].

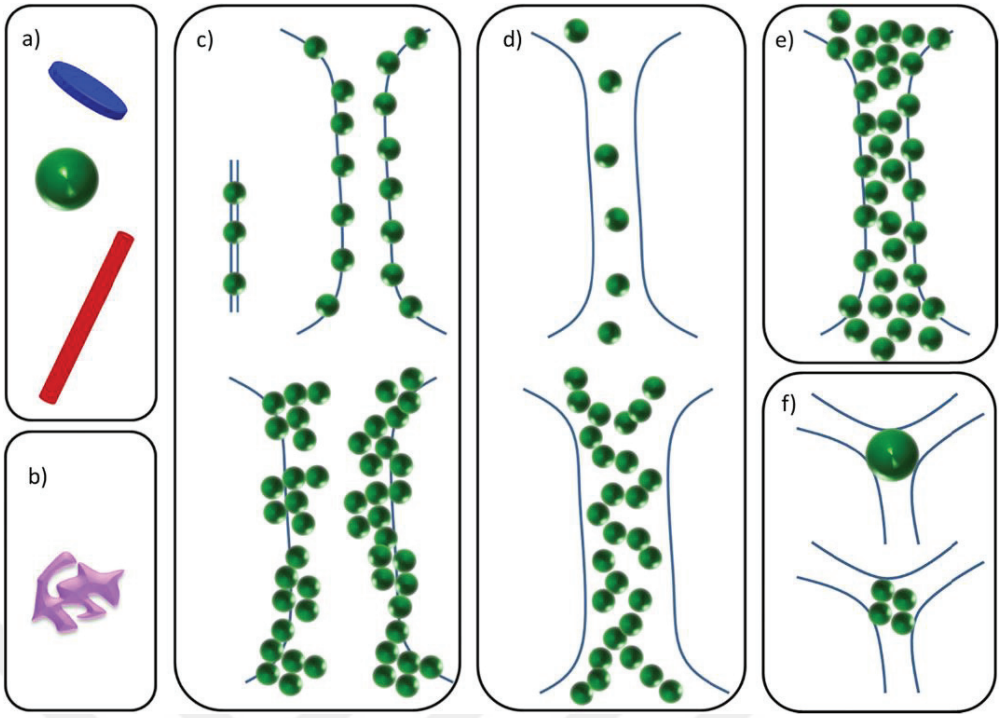

Figure 4.8. Foam stabilization with particles: a) particles with different shapes, b) surface roughness of particles, c) particles absorbed at the interface, d) individual hydrophilic particles, and aggregated or gelified particles in the foam channels, e) aggregated particles adsorbed at the interfaces and in the bulk and f) large aggregates or individual particles in Plateau borders (Source: Fameau and Salonen, 2014)

Hydrophobicity or hydrophilicity of particles affects the way in which they interact with bubbles. The particles with hydrophilicity or having intermediate wettability stabilize foams [62]. A particle is attached to the interface between liquid and gas phase, if the particles is partially wetted. Smaller particles tightly bound to interfaces. Partially wetted particles bridge the liquid as shown at the top of Figure 4.9 ($\theta<90$) while wetted particles stabilize the foam ($\theta>90$) as shown at the bottom of Figure 4.9 [63]. In many cases, the particles are much smaller than film thickness; therefore, Figure 4.9 is not applicable [63]. The pressure difference (Δp) at the Plateau borders controls the flow of liquid out of film between the particle and liquid phase. The value of pressure difference was proposed as [64]

$$\Delta p \propto (R_{PB})^{-1} - (R_F)^{-1} \tag{4.12}$$

where R_{PB} is the Plateau border radius, and R_F is the film radius. R_F is infinite for flat films and when R_{PB} is small, Δp becomes very large (Figure 4.10). The particles on the

cell wall increase the values of R_F and when $R_{PB}=R_F$, Δp becomes very small and therefore, capillary driven flow is prevented, and the film is stabilized (Figure 4.10) [63-64].

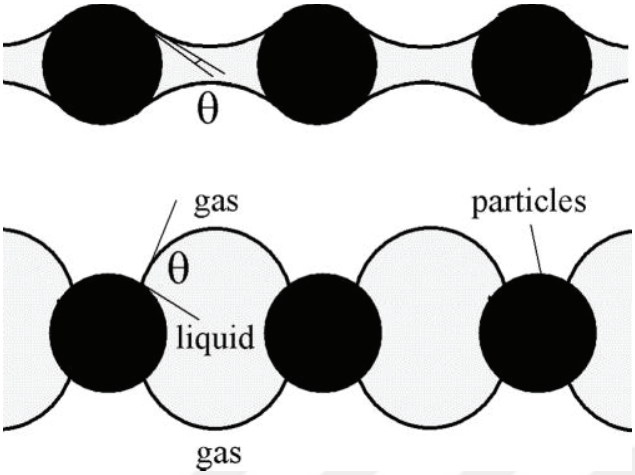

Figure 4.9. Wetting angle effect on the foam stabilization, top partially wetted particles and bottom wetted particles (Source: Banhart, 2006)

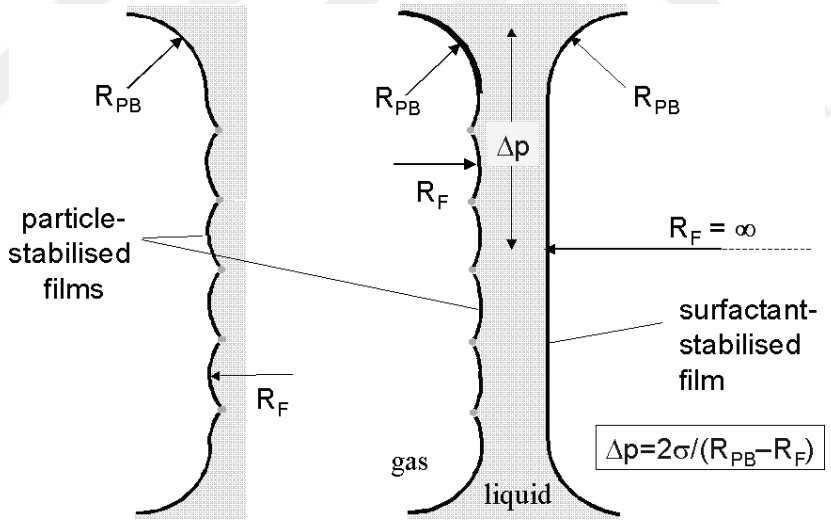

Figure 4.10. Stabilization of foams (Left: poorly wetted, right: wetted particles) (Source: Banhart, 2006)

The presence of static stabilizing forces is another way of foam stabilization. Foam films drain slowly due to gravitational or capillary forces. Since the capillary forces reduce the film thickness, an additional force called "disjoining pressure" Π balances the capillary forces. Disjoining pressure emerges when interaction of the film surfaces begins [58]. The disjoining pressure is

$$\Pi=\Pi_{el}+\Pi_{vdW}+\Pi_{st} \quad (4.13)$$

where Π_{el} is repulsive electrostatic double layer repulsion on two surfaces, Π_{vdW} is short range attractive van der Waals interactions and Π_{st} is steric or structural interaction. Cell wall stability is provided as long as $\partial\Pi/\partial d<0$ [60]. A typical example of the relationship between disjoining pressure and cell wall thickness is shown in Figure 4.11. The cell wall rupture occurs when $d<d_{crit}$ and capillary pressure exceeds Π_{max}. The stability criteria of a cell wall are [58, 65]

$d>d_{crit}$:	$\partial\Pi(d)/\partial d<0$	Stable
$d=d_{crit}$:	$\partial\Pi(d)=\partial d=0$	Metastable
$d<d_{crit}$:	$\partial\Pi(d)/\partial d>0$	Unstable

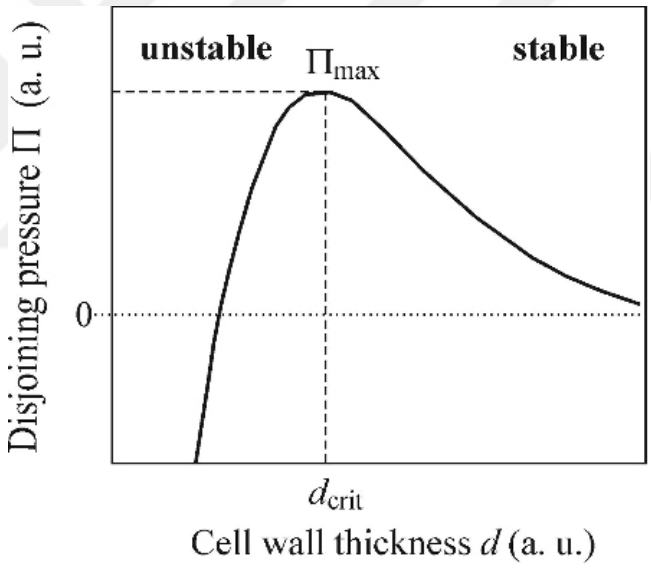

Figure 4.11. A typical example of cell wall thickness and disjoining pressure (Source: Koerner, 2017)

Particle size and particle content are two important parameters in foam processing. Figure 4.12 shows the preferred particle size and particle volume range for successful Al-SiC composite processing [66]. When the particle size is too small (in nanometer level) it is difficult to mix the particles with liquid aluminum and if it is too large it settles on the bottom of liquid aluminum. When particle volume content is too low, the foam is not stabilized and if it is too high the viscosity increases significantly. A volume fraction of

10% and a particle size of 5μm was proposed for the Al-SiC foams having homogeneous cell size distribution [63, 66].

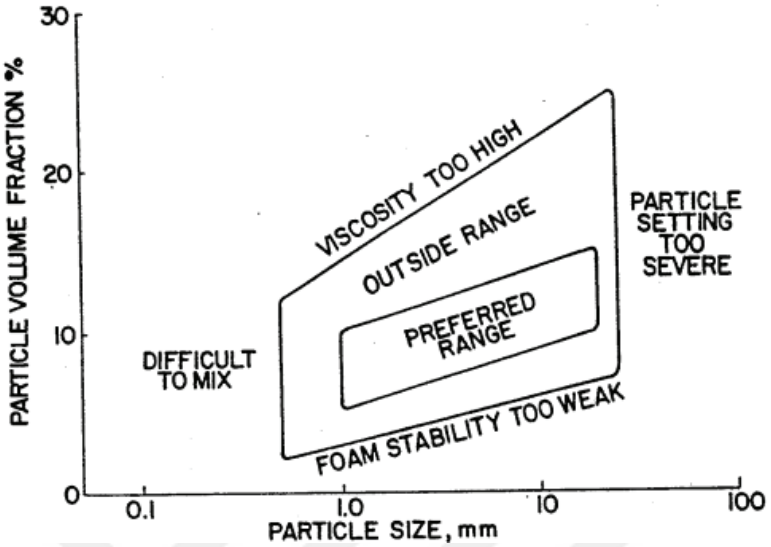

Figure 4.12. Al foam processing parameters
(Source: Jin et al., 1992)

CHAPTER 5

COLLOIDAL CERAMICS AND RHEOLOGICAL PROPERTIES OF SLURRIES

5.1. Colloidal Ceramics

The term colloid is a homogeneous system containing molecules or particles in between 1 nm and hundreds of microns, dispersed through a medium [67]. Since the contact area between particles and the medium is very large, the suspension behavior is affected by the forces between particles or surfaces [68]. Ceramics, especially clay-based materials, have been processed with colloids since the ancient times. In clay-water system, which is the basis for many traditional ceramic processing, clay particles have negatively charged faces and positively charged edges and dispersed in a polar solvent water (Figure 5.1(a)). The plasticity of clay suspensions tends to aggregate the clay particles (Figure 5.1(b)) [68].

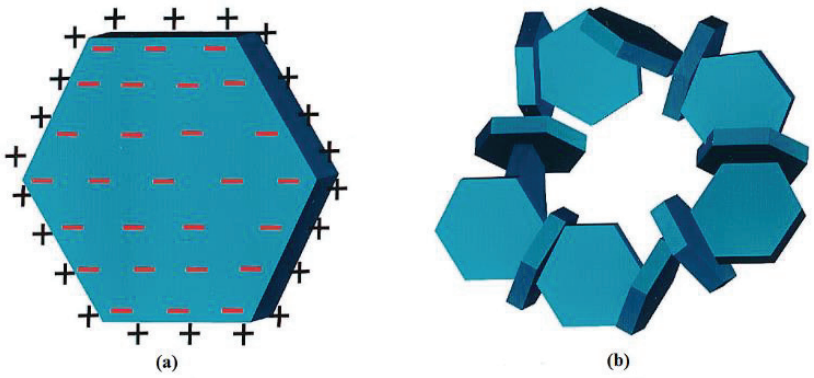

Figure 5.1. Clay particles suspended in water a) individual particle b) aggregated particle due to the attractional forces between the particles (Source: Lewis, 2000)

5.2. Particle-Particle Forces

Colloidal suspension may be found as dispersed, weakly flocculated or strongly flocculated dependent on the interparticle forces (Figure 5.2). In dispersed state, particles

repel each other as repulsive barrier is higher than k_bT (k_b is the Boltzmann constant). In weakly flocculated state, aggregated particles are separated by an equilibrium distance corresponding the secondary minimum, well depth in around 2–20 k_bT (Figure 5.2). The strongly flocculated or coagulated particles correspond to primary minimum state and result in the formation of individual clusters of particles in the suspension [68].

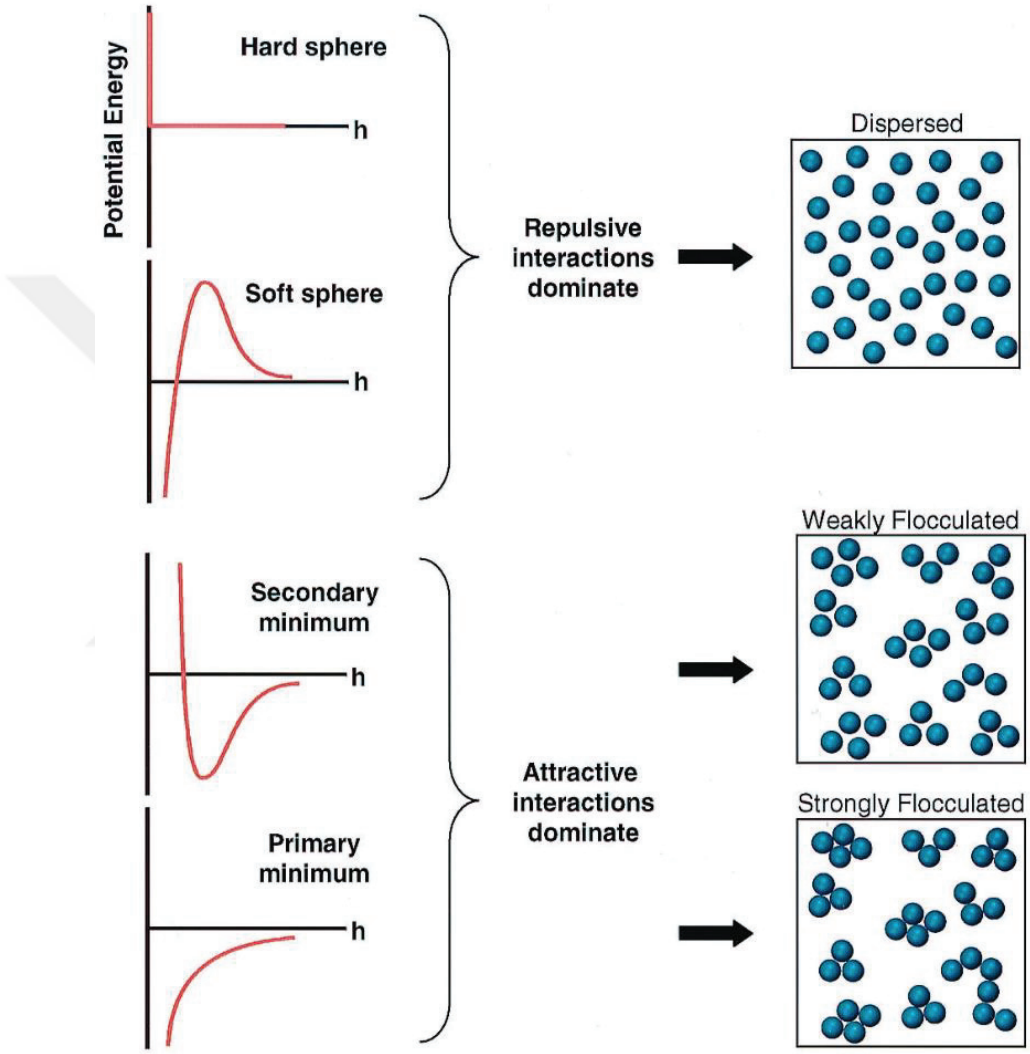

Figure 5.2. The relationship between interparticle potential energy and the subsequent colloidal structure (Source: Lewis, 2000)

Colloidal stability is provided by the total interparticle potential energy, V_{total}, given as

$$V_{total}=V_{vdW}+V_{elect}+V_{steric}+V_{structural} \quad (5.1)$$

where V_{vdW} is the attractive potential energy due to the van der Waals forces between particles, V_{elect} is the repulsive potential energy between charged particles, V_{steric} is the repulsive potential energy due to the steric interactions between particle surfaces coated with polymers and $V_{structural}$ is the potential energy due to the unabsorbed species in solution [68]. Van-der Waals forces are long-range forces and attractive between particles. Hamaker expression defines the V_{vdW} for equal sized spherical particles as [68]

$$V_{vdW}=-\frac{A}{6}\left(\frac{2}{S^2-4}+\frac{2}{S^2}+\ln\frac{S^2-4}{S^2}\right) \tag{5.2}$$

where S is given as

$$S=\frac{2a+h}{a} \tag{5.3}$$

In above equation, A is the Hamaker constant, h is the minimum separation between particle surfaces and a is the particle radius [68]. The Hamaker constants for some ceramics in vacuum and eater medium are tabulated in Table 5.1.

Table 5.1. Non-treated Hamaker constants for ceramic materials interacting under vacuum and across water at 298 K (Source: Lewis, 2000)

		Hamaker Constant (x10^{-20} J)	
Material	**Crystal Structure**	**Under Vacuum**	**Across Water**
α-Al_2O_3	Hexagonal	15.2	3.67
$CaCO_3$	Trigonal	10.1	1.44
SiO_2 (quartz)	Trigonal	8.86	1.02
SiO_2	Amorphous	6.5	0.46
ZnO	Hexagonal	9.21	1.89

Dielectric properties of suspension medium and the surface potential resulting from the interaction of particles also affect the total interparticle potential energy. This effect is called electrostatic potential, V_{elect}. For equal sized spherical particles, it is given as [68]

$$V_{elect}=2\pi\varepsilon_r\varepsilon_0 a\Psi_0^2\ln[1+\exp(-kh)] \tag{5.4}$$

and is applicable when $k\alpha > 10$. When $k\alpha < 5$, V_{elect} is given as

$$V_{elect}=2\pi\varepsilon_r\varepsilon_{r0}a\Psi_0^2\exp(-kh) \tag{5.5}$$

where, ε_r is the dielectric constant of the solvent used, ε_0 is the permittivity of vacuum, Ψ_0 is the surface potential and k is the Debye-Hückel screening length. The values of k are given as

$$k=\left(\frac{F^2\sum_i N_i z_i^2}{\varepsilon_r\varepsilon_0 kT}\right)^{1/2} \tag{5.6}$$

where N_i and $z_i$are the number density, and i is the counterions, and F is the Faraday constant [68].

Electric double layer is a phenomenon in electrostatic stabilization of colloids. Colloidal particles gain negative electrical charge when negatively ions of dispersion medium are adsorbed on particle surface. Therefore, negatively charged particle attracts the positive counterions surrounding particle (Figure 5.3).

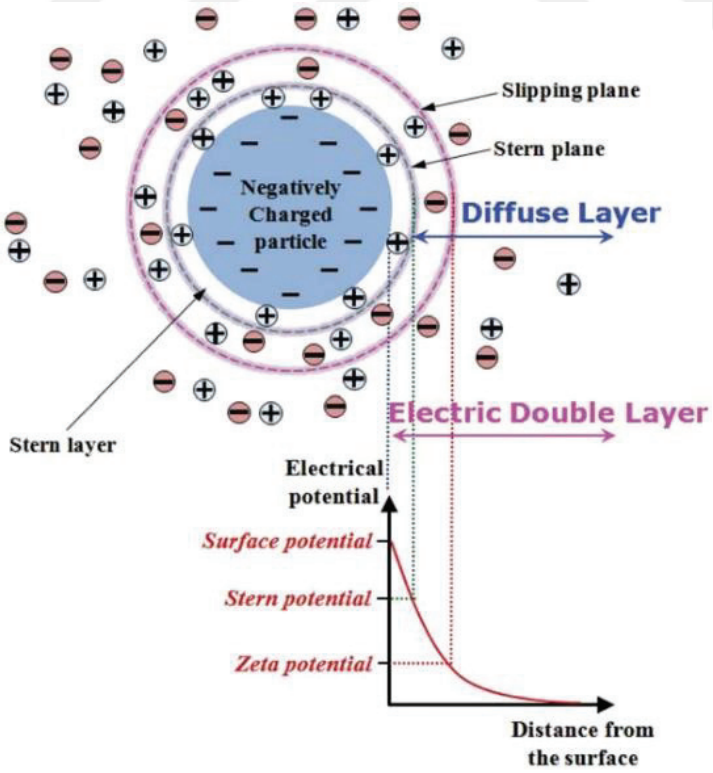

Figure 5.3. Electric double layer diagram
(Source: Park and Seo, 2011)

As shown in Figure 5.3, an electric double layer consists of three regions, surface charge, stern layer and diffuse layer. Surface charge means charged ions adsorbed on the particle surface. Stern layer means counterions attracted to the particle surface. Diffuse layer means a film of dispersion medium containing higher concentration of counterions. Stern layer is the electric double layer having the maximum value on the particle surface. Slipping plane (shear plane) is the plane occurred by the motion between the colloidal particles and the dispersion medium [69].

According to the DLVO theory, ionic strength and changing pH to the isoelectric point (IEP) make dispersions unstable [68]. For instance, weakly attractive alumina suspensions were formed in aqueous environment at pH conditions below the IEP and yield strength increased with the increase of electrolyte concentration [60, 62-63].

In steric stabilization the adsorbed organic molecules initiate steric repulsion to prevent flocculation and vdW attraction between adsorbed layers [68]. Different polymer systems are used for steric stabilization. Figure 5.4 (a-d) sequentially show the stabilization ceramic surfaces by homopolymer, diblock copolymer, comb-like copolymer and functional polymer. Polyelectrolyte species are also used to provide electrostatic and steric stabilization for colloidal dispersions [68].

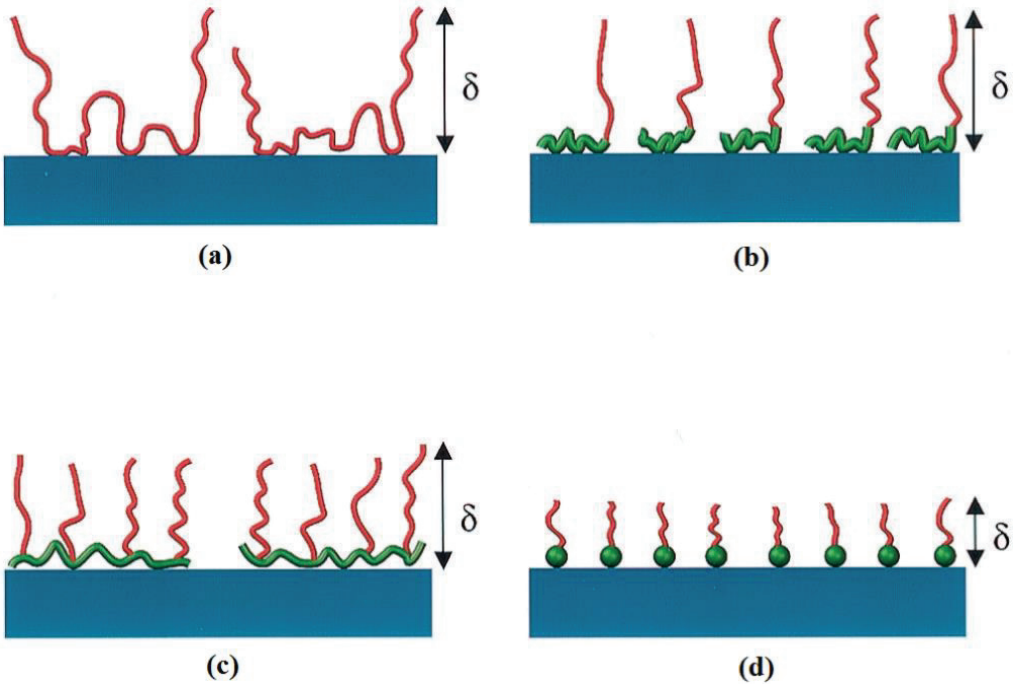

Figure 5.4. Schematic representations of different types of polymers adsorbed in ceramic surfaces: a) homopolymer b) diblock copolymer c) comblike copolymer and d) Functional polymer (Source: Lewis, 2000)

5.3. Rheology

Rheology is the study of the flow of matter and provides information on the flow and deformation properties for processability of materials. Preparation of suspensions with desired flow properties and having stability against sedimentation, aggregation and agglomeration can be succeeded by understanding the rheological behavior of the suspension.

Fluidity of materials under specific flow conditions can be characterized by a dimensionless number which is called the Deborah Number (D_e), which is given as [70]

$$D_e = \frac{t_c}{t_p} \tag{5.7}$$

where, t_c refers to the characteristic flow time and t_p refers to the stress relaxation time. If the Deborah number of a material is lower than 1, the material is defined as liquid-like material. If the Deborah number of a material equals to 1, the material is defined as viscoelastic material. If the Deborah number of a material is higher than 1, the material is defined as solid-like material.

Ideal solids are defined by Hooke's and Newton's law. Liquid-like and viscoelastic materials are categorized as Newtonian and Non-Newtonian, respectively. In Newtonian fluids, viscosity is independent of shear rate. The relationship between shear stress and shear rate is

$$\tau = \eta \frac{d\gamma}{dt} = n\ \dot{\gamma} \tag{5.8}$$

where τ is the shear stress, η is the viscosity, γ is the deformation and t is the time.

For Non-Newtonian fluids, viscosity is a function of shear rate. Some materials behave as Newtonian at lower shear rates. However, their viscosities decrease at higher shear rates. These materials are identified as shear-thinning (pseudoplastic) materials (Figure 5.5 (b)). Some materials exhibit Newtonian behavior at lower shear rates, but their viscosities increase at higher shear rates. These materials are called as shear-thickening materials (Figure 5.5 (c)) [71].

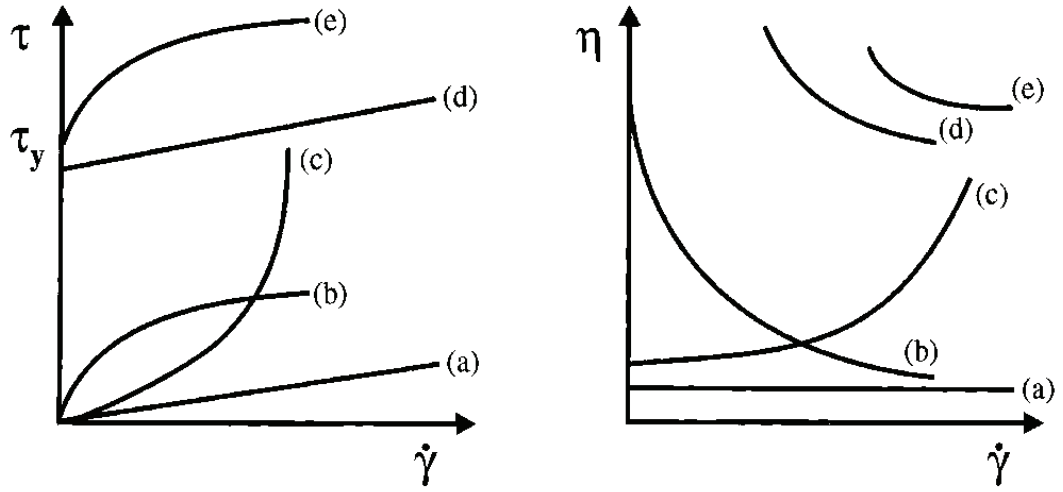

Figure 5.5. Types of rheological behavior a) Newtonian flow, b) shear thinning c) shear thickening d) Bingham plastic and e) pseudoplastic with yield stress (Source: Lewis, 2000)

The most widely used measurement method of suspensions consists of oscillating strain over a range of frequencies and measuring the peak stress, σ_0. In the linear viscoelastic region, stress and strain relationship is as follows [72]

$$G^*=\sigma_0/\gamma_0 \tag{5.9}$$

where G^* is the dynamic modulus which is independent of stress or strain. Dynamic modulus is also expressed as

$$G^*=G'+iG'' \tag{5.10}$$

where G' is the storage modulus, G'' is the loss modulus and i is the complex number which equals to $\sqrt{-1}$ [72].

5.4. Stable Suspensions

Colloidally stable suspensions show a shear-thinning behavior under steady shear because of the perturbation of the suspension structure. At stead shear rates, suspension structure is close to the equilibrium because thermal motion controls over the viscous

forces. At higher shear rates, viscous forces affect the suspension structure, so shear thinning occurs. At very high shear rates, the viscous forces dominate the suspension structure and hydrodynamic forces become effective. Increasing volume fraction of solids increases the degree of shear thinning and the viscosity [72].

A model describing shear-thinning behavior was developed at high shear rates and given as [72]

$$\eta=\eta_{\infty}+\frac{\eta_0-\eta_{\infty}}{b\dot{\gamma}^p} \tag{5.11}$$

where b and p are the fitting parameters, γ is the shear rate and η_0 and η_{∞} are the low shear and high-shear limiting viscosities respectively. The model is applicable at the shear rate region where $b\dot{\gamma}^p>>1$. Figure 5.6 represents the viscosity vs. shear rate of a silicon nitride suspensions at different solid contents. As seen in Figure 5.6, Equation 5.11 is well fitted with the data at higher shear rates and hence well described the steady shear properties of a stable silicon nitride suspension [72].

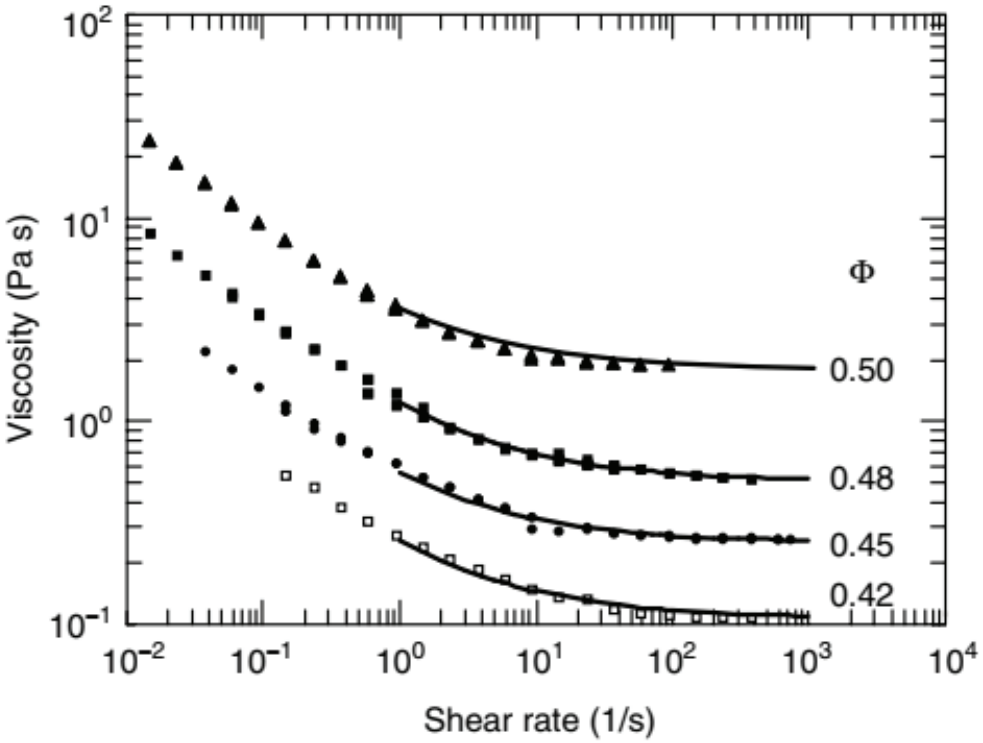

Figure 5.6. Degree of shear thinning of silicon nitride suspension at different solid contents (Source: Bergstrom, 2017)

5.5. The Effect of Solid Content, Particle Size and Particle Shape

The viscosity of suspensions is highly dependent on solid content with the viscosity approaching infinity at a maximum solid volume fraction, $\emptyset_m$. As the average separation distance between particles approaches to zero, particles pack together and flow become impossible. Also, particle size distribution and the particle shape affect the maximum volume fraction. A wide particle size distribution causes higher volume fraction because small particles can fit into the voids between the large particles [72-73].

Non-spherical particles in the suspension cause the rotation of the particles in Brownian motion which results in an excluded volume greater the volume-fraction of the particles. Thus, as the anisotropy increases, this effect increases. Figure 5.7 represents the relationship between the volume fraction of different solids and viscosity. The experimental values were fitted to a modified Krieger-Dougherty Equation given as

$$\eta_r = \left(1 - \frac{\emptyset}{\emptyset_m}\right)^{-n} \tag{5.12}$$

where $\emptyset_m$ and n are used as fitting parameters [74].

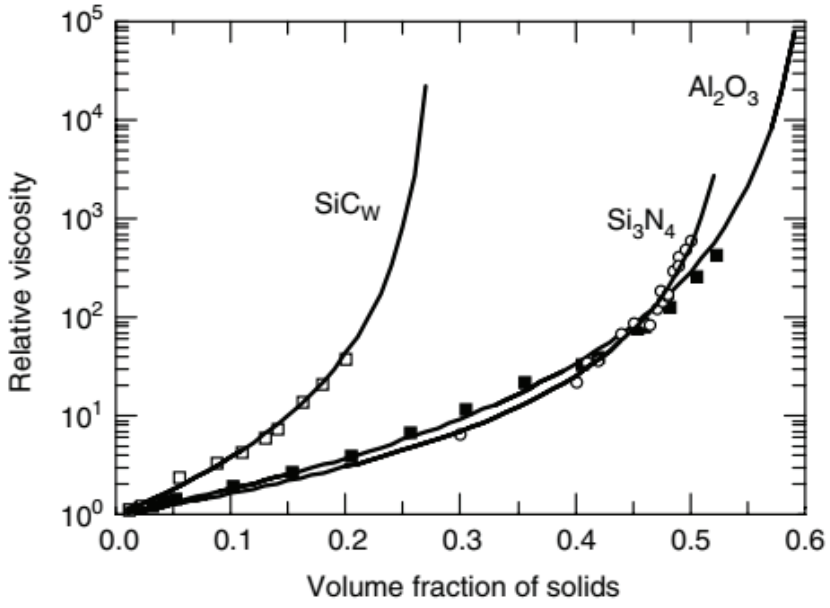

Figure 5.7. The relationship between viscosity and volume fraction of different solids (Source: Sigmund et al., 2000)

CHAPTER 6

MATERIALS AND EXPERIMENTAL PROCEDURE

6.1. Powders

The glass powder used in foaming experiments was obtained from waste glass (cullet) and received from a local supplier in powder form as shown in Figure 6.1. The powder cullet was mainly composed of waste window glass. The average particle size of the powder was determined ~72 μm. As-received glass powder was fractioned for foaming experiments by sieving below 38 μm, between 38 and 45 μm and between 45 and 56 μm. The sieving was performed in a Fritsch Analtysette 3 PRO type vibrational sieving machine. The sieved powders were then coded as fine for the powder particle sizes less than 38 μm, medium for the powder particle sizes between 38 and 45 μm and coarse the powder particle sizes between 45-56 μm. The SEM picture of as-received glass powder is shown in Figure 6.2(a) and the powder particle sizes between 38 and 45 μm, between 45-56 μm and below 38 μm in Figures 6.2(b-d), respectively.

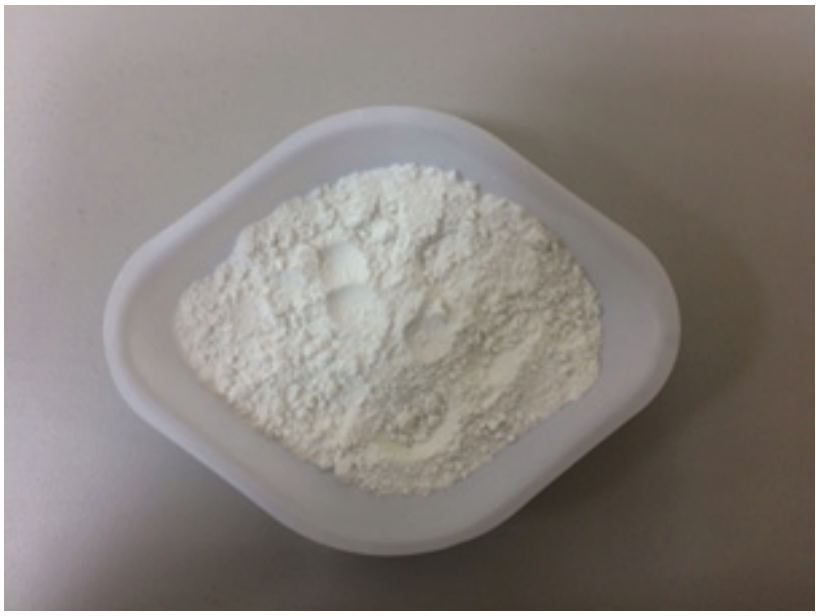

Figure 6.1. The picture of as-received waste glass powder

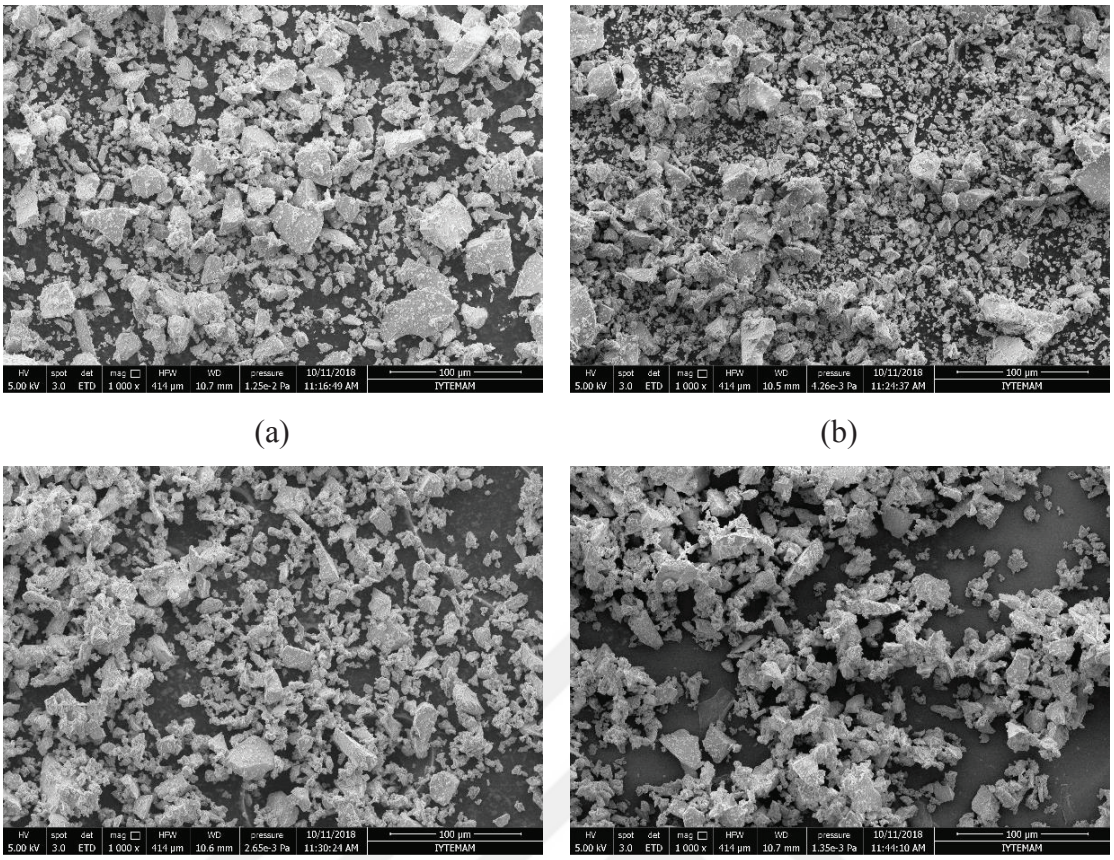

Figure 6.2. a) As-received glass powder and powders sieved between b) 45 and 56 and c) 38 and 45 μm and below d) 38 μm

A commercially available aluminum powder paste and calcium hydroxide (lime) supplied by AKG Gazbeton company of Turkey was used as the foaming agent in the foaming experiments. The same foaming agent is currently used in the production of AAC. In order to prevent the oxidation of Al powder, the surfaces of powder particles were covered with an oil-based paste by the producer. Before microscopic analysis the agglomerated as-received Al powder paste was dispersed in water. A drop of dispersed particles was then deposited on a filter paper and let to dry. Dried powder particles were then analyzed in SEM. The SEM micrographs of aluminum particles in the foaming agent are shown in Figures 6.3(a-d) at increasing magnifications. Aluminum particles are in flake form and mostly angular in shape as seen in the same micrographs. The long and short axes of flakes were 10 μm and 5 μm, respectively. All the slurries prepared for foaming experiments contain 1 wt% aluminum paste and 1 wt% calcium hydroxide.

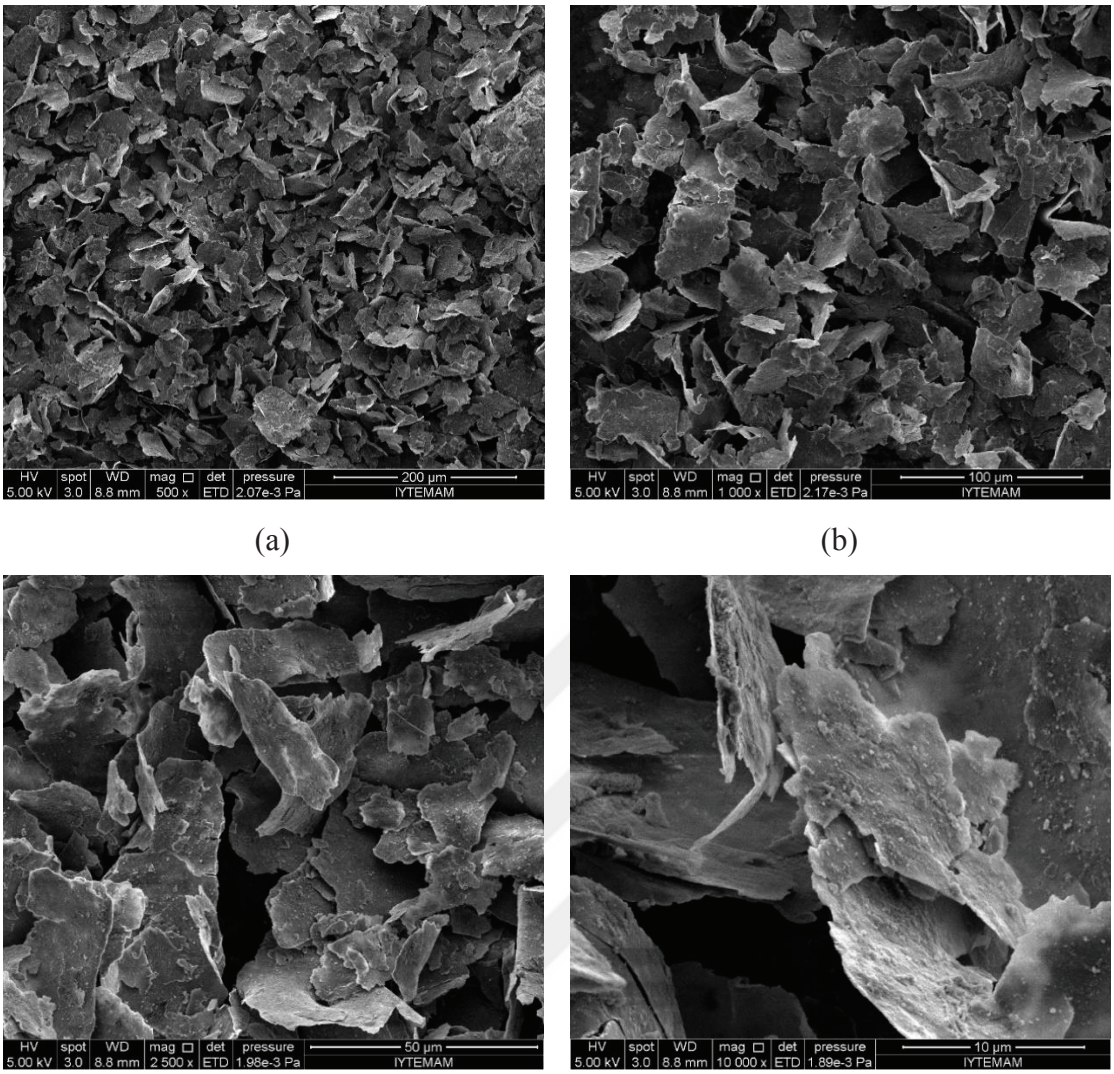

Figure 6.3. The SEM micrographs of Al powder in a) 500x b) 1000x c) 2500x and d) 10000x magnification

6.2. Binder

Sigma Aldrich (419273) sodium carboxymethylcellulose (CMC) was used as a binder. Carboxymethyl cellulose or cellulose gumis a cellulose derivative with carboxymethyl groups (-CH2-COOH) bound to some of the hydroxyl groups of the glucopyranose monomers that make up the cellulose backbone. It is often used as its sodium salt, sodium carboxymethyl cellulose. Carboxymethylcellulose is used in food as a viscosity modifier or thickener, and to stabilize emulsions in various products. Carboxyl groups of the carboxymethyl cellulose interact with the surface of the glass particles

forming steric stabilization of particles. The schematic representation of interaction between the glass particles and CMC is shown in Figure 6.4.

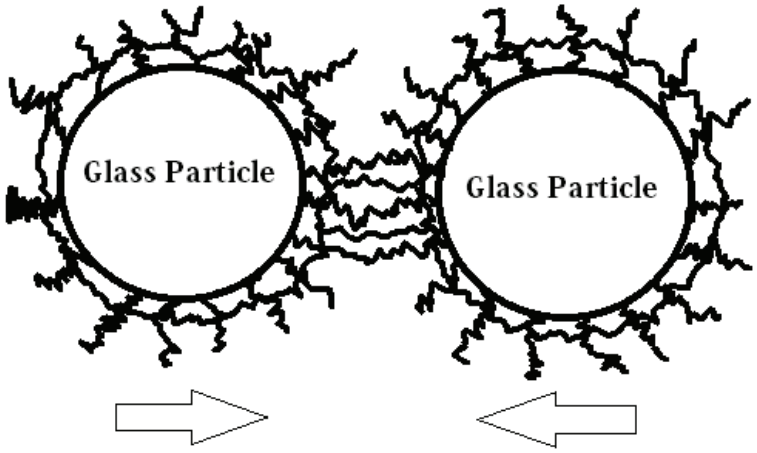

Figure 6.4. Schematic representation of steric stabilization of glass particles provided by CMC addition

6.3. Characterization

The particle size distribution of the glass powder was determined in a Malvern Mastersizer 2000 laser diffractive analyzer. The crystal structure of the powders was determined by Philips X'Pert Pro X-Ray Diffraction (XRD) device (Cu-Kα radiation, λ=1.54 A° and 40 kV). The XRD analysis was subjected between 5 and 80° in 2θ intervals. The elemental composition was determined using a Spectro IQ II X-Ray Fluorescence (XRF) device. Morphological properties of powders and foams were analyzed using a FEI Quanta 205 FEG and Philips XL 30SFEG SEM. Buehler epo-wick fast curing epoxy was used to prepare the samples for SEM analysis. The samples were grinded with SiC grinding papers through 800, 1000, 1200, 2000, and 2400 grids and polished by 9 μm, 6 μm, 3 μm and 1 μm diamond solutions respectively. Density of the green and sintered bodies were determined by measuring the dimensions of samples and the weight.

6.4. Rheological Properties of Slurries

Rheological properties of slurries were studied using a Thermo Electron Corporation Haake Mars II Rotational Rheometer device (Figures 6.5 (a) and (b)). Slurry

was placed to the fixed bottom plate and the top plate were rotated on the sample in order to form shear forces on the slurry. The plates were made of 6 mm diameter titanium. Shear rate versus shear stress and shear rate versus shear stress curves of each slurry were measured for at least 3 times in order to prove the repeatability of properties.

(a) (b)

Figure 6.5. (a) Haake Mars II Rotational Rheometer device and (b) measurement plate where the sample placed

6.5. Slurry Preparation and Foaming Experiments

The stages of the slurry preparation for foaming experiments are schematically shown in Figure 6.6. The process started with the mixing of appropriate amounts of glass powder, foaming agent, lime and CMC solution in distilled water. Mechanical disperser was used to mix the ingredients for 1 minute at 2000 rpm to form a homogeneous slurry. Then the mixture was poured into a cylindrical Teflon© tube which was closed at the bottom for expansion experiments (Figure 6.7 (a)). The tube was placed on a Teflon plate and the bottom side was made airtight using a sealing strip material as seen in Figures 6.7 (a) and (b). The molding tubes were in 40 mm in inner diameter and 5 mm in thickness. Teflon© was used in order to reduce the friction between the slurry and the mold during foaming. However, a transparent plexiglass mold was also used in few foaming experiments in order to record bubble formation and expansion (Figure 6.7 (b)).

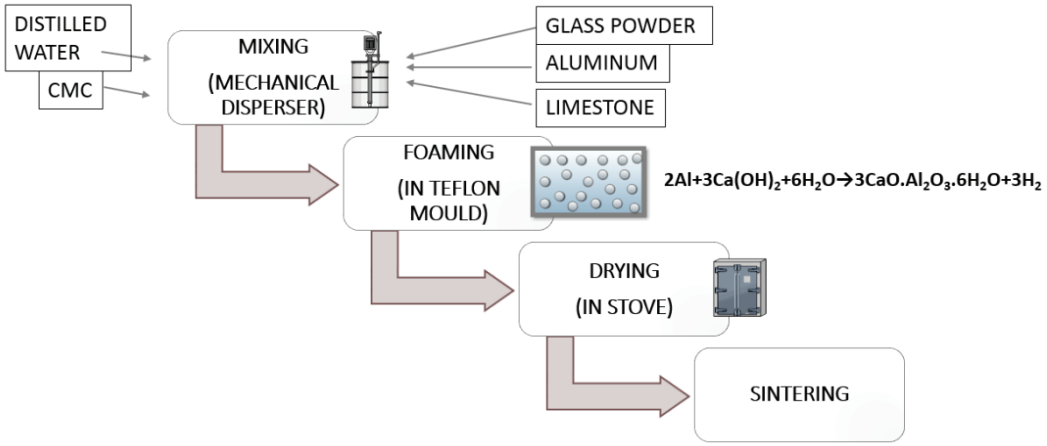

Figure 6.6. Stages of slurry preparation for foaming experiments

(a) (b)

Figure 6.7. The molding tubes used in foaming experiments (a) Teflon© and (b) Plexiglass transparent tube

Preliminary studies showed that foaming of slurry highly was dependent on the rheological properties. The slurries with the solid contents lower than 50 wt% and higher than 60 wt% showed relatively lower expansions sequentially due to relatively low and high viscosities of slurry. Therefore, the solid contents of the slurry in present study were chosen 50, 55 and 60 wt%. The amount of binder was 2, 3 and 4 wt% as lower and higher amount found to be not effective in expansion. The investigated slurries are tabulated in Table 6.1 together with wt% of solid content and binder and glass powder size. Each slurry in Table 6.1 was foamed at least three times and the resultant expansions were averaged. A 3^3 full factorial design was used to determine experimental conditions. By using this method, three factors were studied each at three levels.

Table 6.1. Slurries used in foaming experiments

	Factor 1	Factor 2	Factor 3
Specimen	**A: Solid Content (wt%)**	**B: CMC Content (wt%)**	**C: Particle size of glass powder (µm)**
23	55	3	49.6
15	60	3	31
20	55	2	49.6
19	50	2	49.6
9	60	4	12.4
18	60	4	31
2	55	2	12.4
3	60	2	12.4
14	55	3	31
1	50	2	12.4
26	55	4	49.6
10	50	2	31
8	55	4	12.4
12	60	2	31
27	60	4	49.6
13	50	3	31
11	55	2	31
16	50	4	31
22	50	3	49.6
21	60	2	49.6
4	50	3	12.4
25	50	4	49.6
17	55	4	31
7	50	4	12.4
5	55	3	12.4
6	60	3	12.4
24	60	3	49.6

The foaming setup used is shown in Figure 6.8. The experimental setup mainly consisted of a foaming mold (tube) and a linear expansion measurement system. The linear expansion measurement system consisted of a laser sensor standing above the foaming mold and clamped by a holder, a data logger (Data Taker DT 80) and a computer. The picture and technical drawing of the laser sensor, Micro Epsilon ILR1030-8 (4-20 mA), are shown sequentially in Figures 6.9 (a) and (b). The minimum distance between the measured sample and the laser sensor should be at least 20 cm in order to get measurable signals. The sensor was operated between 4 to 20 mA and was initially calibrated for distance measurement. The calibration was made by determining the

corresponding current difference of a known distance. By dividing known distance to the current difference then the calibration constant was determined as distance/current. Then, the simultaneous length change measured by the sensor was recorded by a data logger.

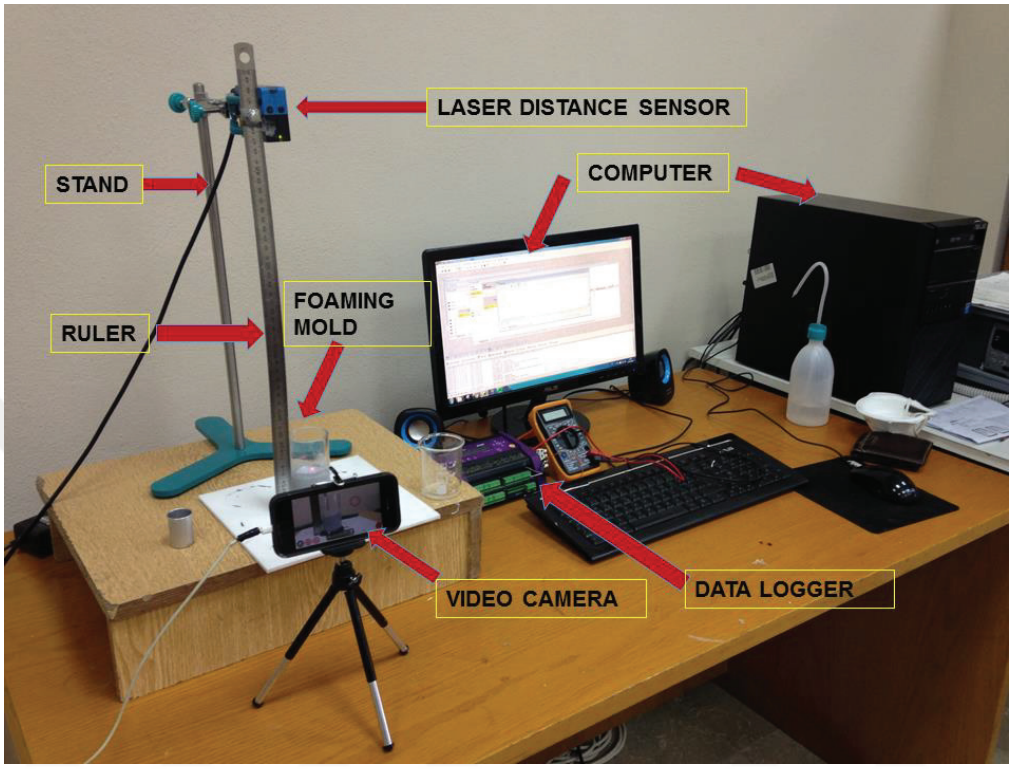

Figure 6.8. Foaming set-up

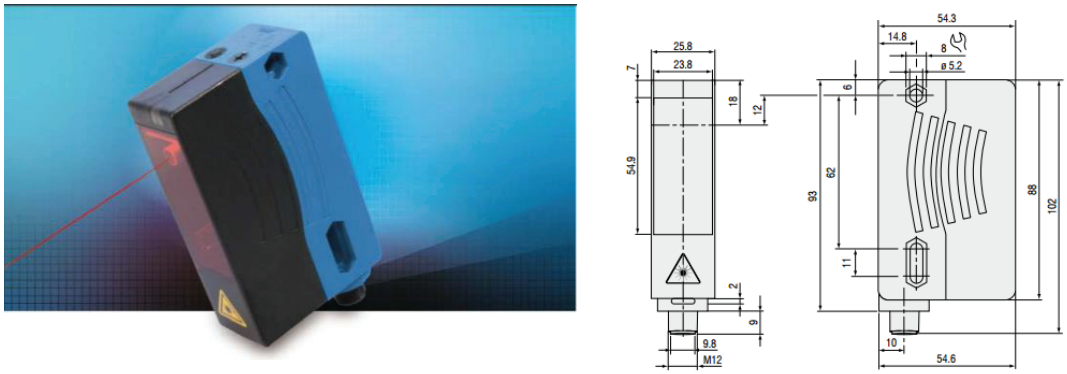

(a) (b)

Figure 6.9. (a) Picture and (b) the technical drawing of Micro Epsilon ILR1030-8 laser sensor

A piece of white paper was inserted on the surface of slurry before foaming experiment started. This paper stayed at the top, as the slurry expanded upward, providing

a white color background at the slurry's surface throughout the expansion and making the expansion measurement possible. The percent volume expansion (V_E%) was calculated using the following relation

$$V_E(\%)=\frac{h_f-h_0}{h_0}x100 \quad (6.1)$$

where, h_f and h_o are the final and initial height of the slurry, respectively. The bubble formation during the foaming was recorded by a Sony RX100ii high resolution camera. High-resolution pictures were taken from the pre-determined points of recorded video and the images were used to measure the bubble size distribution. The measurements were performed using Image J software program. In order increase the contrast, image enhancement techniques including image smoothing, sharpening and threshold were applied. An example of image enhancement is shown in Figure 6.10 (a-b). Foaming images in Figure 6.10 (a) were processed into the images in Figure 6.10 (b) using image enhancement techniques. The white area in Figure 6.10 (b) represents the glass matrix and the black areas represent the bubbles. The pictures were taken at 7, 9, 12, 20, and 30 minutes after foaming started. In the experiment, foaming started after 2 minutes following the foaming agent was added to the slurry. Since the bubble size was very small at these minutes, the bubble size could not be detected from the video records. Therefore, the bubble size was determined after 7 minutes. Therefore, the bubble formation until 7 minutes was not considered in this study.

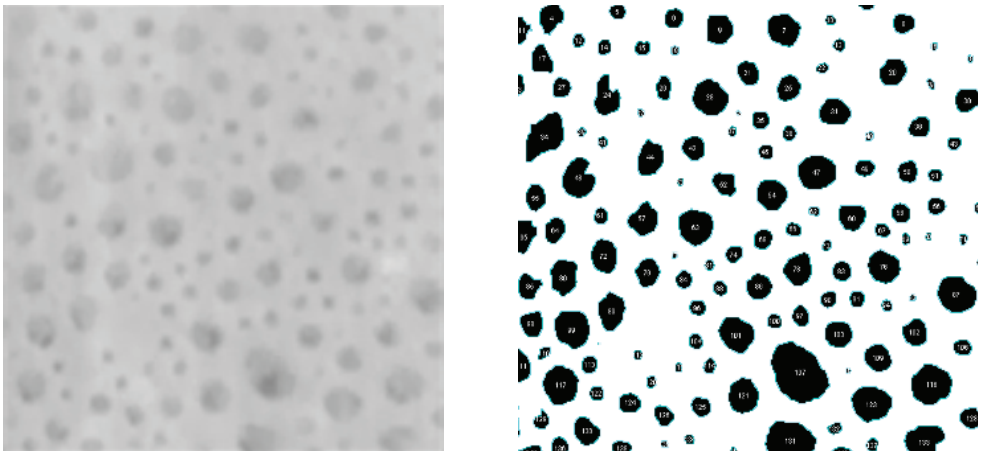

(a) (b)

Figure 6.10. The image of bubbles (a) from video record and (b) after Image J processing

6.6. Sintering of Green Bodies and Preparation for Compression Test and Thermal Conductivity Measurements

The green bodies of foamed samples were sintered in a Protherm Laboratory Furnace Model PLF 130/25. Circular shaped paper box molds were used to minimize the destruction of body while rejecting from the mold and minimize the stress concentration formation at the edges of the mold. The diameter of the mold was 75 mm. Green bodies were sintered at 650, 700, 750 and 800 ^{o}C temperatures. Sintering duration was 30 and 60 minutes and heating rate was 10 ^{o}C min^{-1}.

The cylindrical test samples 20 mm in diameter and 20 mm in length were core-drilled from sintered foam samples. The surfaces of the core-drilled samples were cleaned by applying pressurized air. Before the compression test, the end surfaces of the samples were grounded flat. The compression test samples were weighted and kept inside a desiccator until they were tested. The density of each sample was measured before the compression test. Room temperature quasi-static compression tests were conducted using a displacement-controlled SHIMADZU AG-I universal test machine at the strain rate of $1x10^{-3}s^{-1}$. To compress the samples axially, self-aligned pin-ball compression test platen was used in the tests. A video extensometer synchronized with the test machine was used to record sample axial displacement. The sample deformation until and after fracture was recorded simultaneously during a test using video camera. At least 4 tests were performed for each group of samples. The nominal stress (σ) and strain (ε) were calculated using the following relations,

$$\sigma = \frac{P}{A_s} \tag{6.2}$$

and

$$\varepsilon = \frac{\delta}{L_s} \tag{6.3}$$

where, P, A_s, δ and L_s are the applied load and the initial area, displacement and initial length of the sample, respectively.

Thermal conductivity analysis was performed at C-Therm Thermal Conductivity Analyzer device using 30x10x10 mm rectangular samples (Figures 6.11 (a) and (b)). The device employs a modified transient plane source (MTPS) technique in characterizing

and effusitivity of materials. In this technique, a known current is applied to the sensor's spiral heating element and provides a small amount of heat. A guard rig supports a one-dimensional heat transfer into the sample, as a result of the heat rising at the interface between the sensor and the sample, a voltage drop occurs in the sensor. The rate of increase in sensor voltage is used to determine the thermal properties of the sample [75].

(a) (b)

Figure 6.11. (a) Thermal conductivity measurement device and (b) Glass foam sample for thermal conductivity measurement

CHAPTER 7

RESULTS

7.1. As-Received Glass Powder

The XRD spectrum of as-received glass powder is shown in Figure 7.1. The XRD spectrum shows typical amorphous structure of glass powder. As-received glass powder is composed of 73% SiO_2, 12% Na_2O, 12% CaO, 1.6% MgO and 1.4% Al_2O_3 determined by XRF analyses, which represented the typical composition of soda-lime glass.

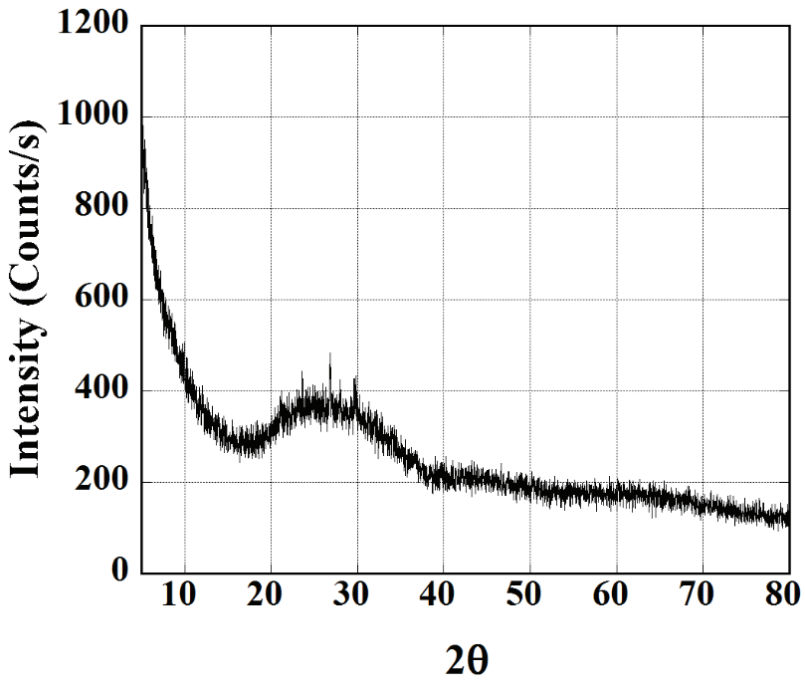

Figure 7.1. The XRD pattern of as-received glass powder

7.2. Rheology of Slurries

Figure 7.2(a) shows three shear stress-shear rate curves of the medium particle size slurry with 50 wt% solid content and no CMC addition. Significant variations in shear stresses between three measurements are noted in the same figure, although the

same slurries are used in the measurements. It was noted that part of slurries flied away between the discs during measurements as they were most likely not stable and hence resulted in differences between the measurements. The same differences are also seen in the viscosity-shear rate curves of three measurements as shown in Figure 7.2(b).

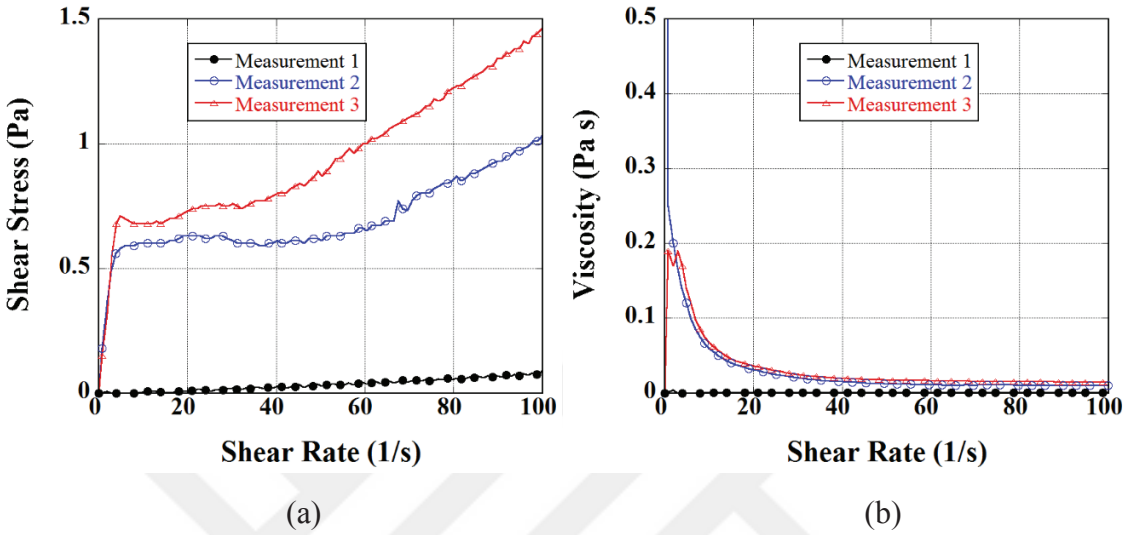

(a) (b)

Figure 7.2. Three measurements of (a) shear stress-shear rate and (b) viscosity-shear rate curves of the slurry with medium particle size, 50 wt% solid content and with no CMC addition

The shear stress-shear rate and viscosity-shear rate curves of three different measurements of the slurry with medium particle size, 50 wt% solid content and 2 wt% CMC are shown in Figures 7.3(a) and (b), respectively. As seen in the same figures, the separate measurements show very much similar shear stress-time and viscosity-time curves with each other. These slurries were stabilized with CMC addition and stayed in between the test discs throughout the measurement. These confirm the critical role played by CMC for the preparation of stable slurries before foaming experiments. As seen in Figures 7.3(a) and (b), the slurry shows a non-Newtonian behavior at the beginning of the measurement; thereafter, the behavior switches into a Newtonian nearly after about 20/s. The separate measurements of the slurry with medium particle size, 55 wt% solid content and 2 wt% CMC also show similar shear stress-shear rate curves (Figure 7.4) with 50 wt% solid content and 2 wt% CMC slurry. Although the slurry shows a non-Newtonian behavior at the beginning of measurements, the behavior switches again into a Newtonian behavior after about 20/s as seen in Figure 7.4. However, the slurry with medium particle size, 60 wt% solid content and 2 wt% CMC addition shows a non-Newtonian shear

thinning behavior (Figures 7.5(a) and (b)). The increase in solid content causes a shift from Newtonian to non-Newtonian behavior. The shear stress-shear rate and viscosity-shear rate curves of fine, medium and coarse particle size slurries with different CMC and solid contents are given in Appendix A. The measured and average viscosities of investigated slurries at 20/s are tabulated in Table 7.1. All viscosity measurements in the thesis were reported at 20/s.

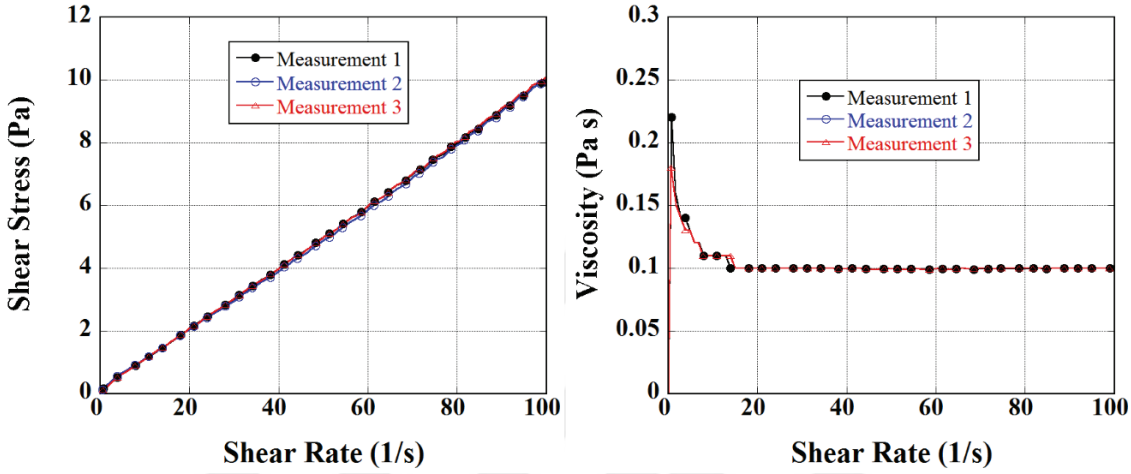

(a) (b)

Figure 7.3. Three measurements of (a) shear stress-shear rate and (b) viscosity-shear rate curves of the slurry with medium particle size, 50 wt% solid content and 2 wt% CMC

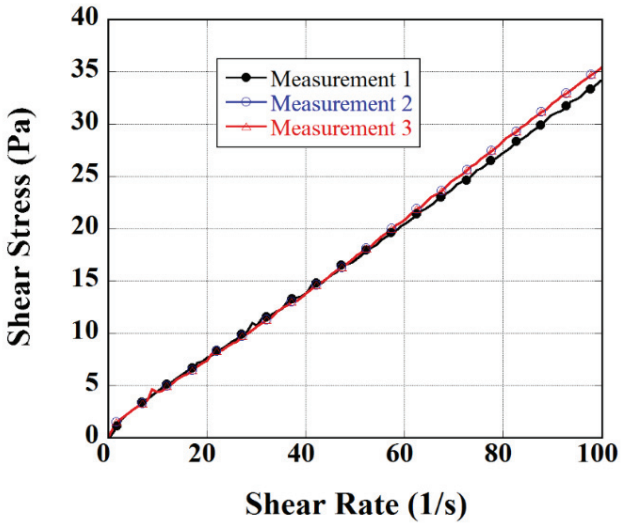

Figure 7.4. Three measurements of shear stress-shear rate curves of the slurry with medium particle size, 55 wt% solid content and 2 wt% CMC

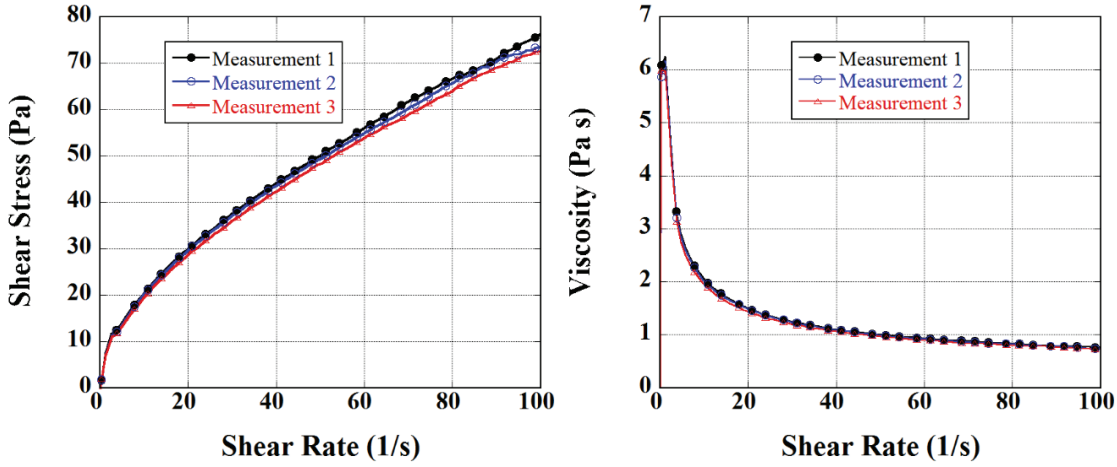

(a) (b)

Figure 7.5. Three measurements of (a) shear stress-shear rate and (b) viscosity-shear rate curves of the slurry with medium particle size, 60 wt% solid content and 2 wt% CMC

Table 7.1. The measured and average viscosities of the slurries

Sample	Viscosity 1 (Pa s)	Viscosity 2 (Pa s)	Viscosity 3 (Pa s)	Average Viscosity (Pa s)
Fine 2% CMC 50% solids	0.1	0.1	0.13	0.11
Fine 2% CMC 60% solids	1.36	1.35	1.3	1.34
Medium 2% CMC 50% solids	0.1	0.1	0.1	0.10
Medium 2% CMC 60% solids	1.36	1.35	1.3	1.34
Coarse 2% CMC 50% solids	1.1	1.06	1.06	1.07
Coarse 2% CMC 60% solids	0.24	0.24	0.25	0.24
Fine 3% CMC 50% solids	2.88	2.62	2.47	2.66
Fine 3% CMC 60% solids	4.59	4.21	4.07	4.29
Medium 3% CMC 50% solids	3.65	3.49	3.45	3.53
Medium 3% CMC 60% solids	4.93	4.73	4.73	4.80
Coarse 3% CMC 50% solids	1.08	1.08	1.08	1.08
Coarse 3% CMC 60% solids	1.66	1.67	1.67	1.67
Medium 4% CMC 50% solids	6.41	6.3	6.19	6.30
Medium 4% CMC 60% solids	28.7	18.2	18.2	21.70
Coarse 4% CMC 50% solids	3.42	3.26	3.34	3.34
Coarse 4% CMC 60% solids	6.48	5.36	5.74	5.86

Figures 7.6 (a), (b) and (c) show the shear stress-shear rate curves of fine, medium and coarse powder size slurries with 50, 55 and 60 wt% solid and 2, 3 and 4 wt% CMC,

respectively. For each slurry, only one representative curve is shown in the same figures. With increasing CMC content, shear stress increases for each powder size slurries. The increase in shear stress is more pronounced in fine powder slurries, particularly when CMC content increases to 4wt% (Figure 7.6(a)). The increase in shear stress is the lowest in coarse powder slurry.

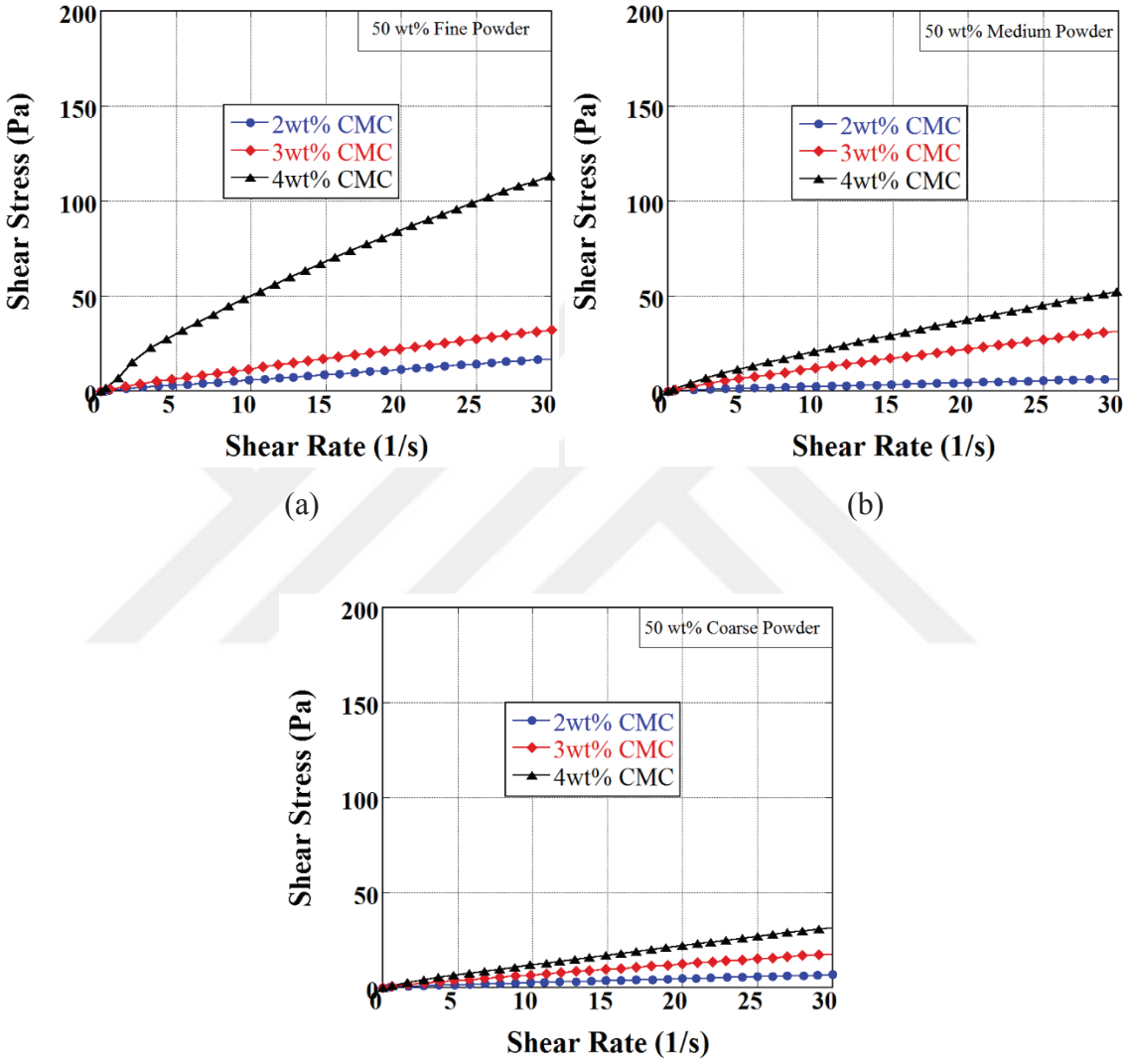

Figure 7.6. The shear stress-shear rate curves of the slurries with 50 wt% solid and 2, 3 and 4 wt% CMC: (a) fine, (b) medium and (c) coarse powder size

When the solid content increases from 50 to 55 wt%, the shear stress of all powder size slurries increases as seen in Figures 7.7 (a), (b) and (c). Note that the shear stress of fine powder slurry with 4wt% CMC increases significantly when the solid content increases to 55 wt%. As seen in the same figures, both solid content and CMC additions

are effective in increasing shear stress. Both medium and coarse powder slurries show similar shear stress-shear rate behavior at 55 wt% solid content.

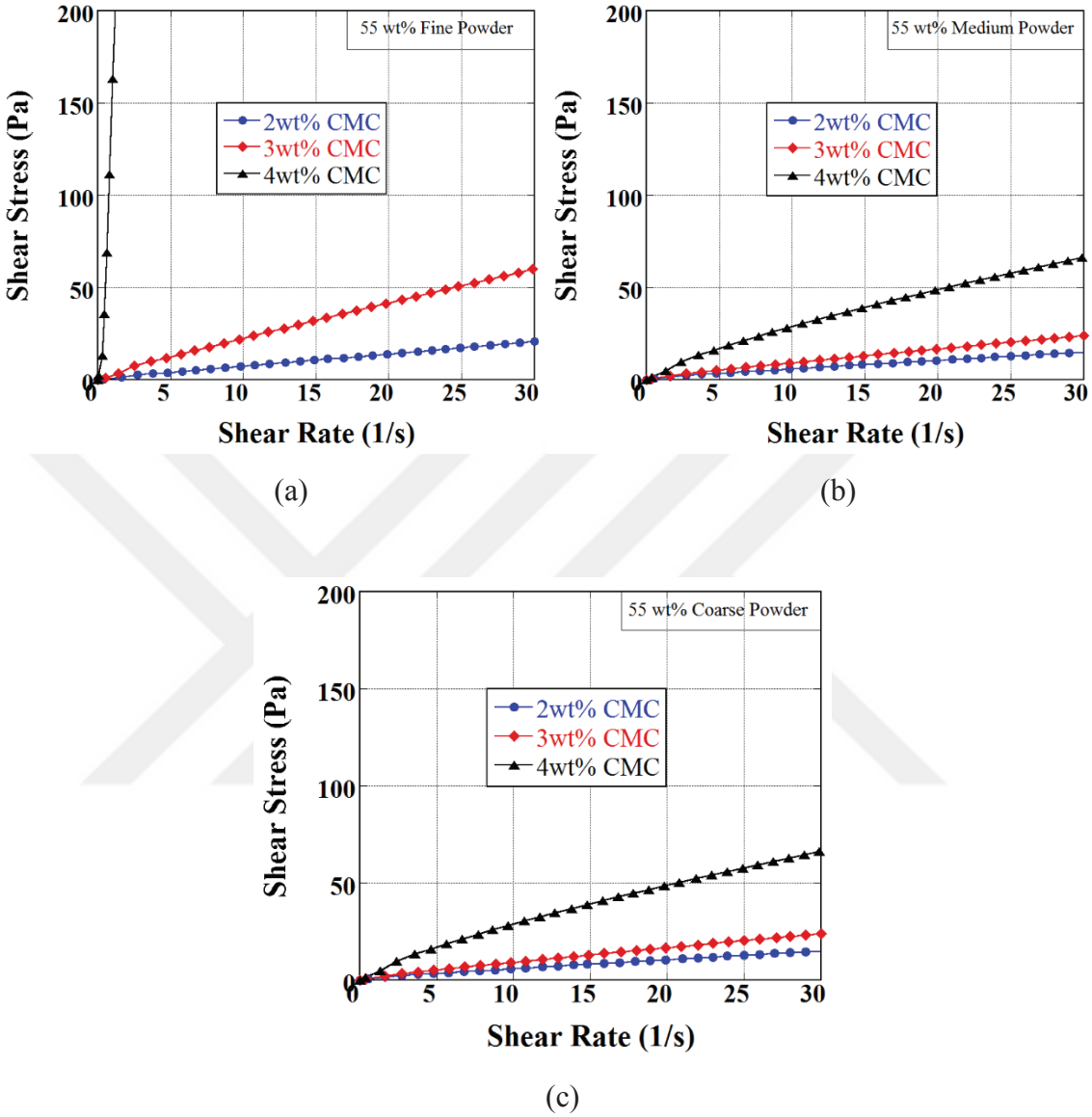

Figure 7.7. The shear stress-shear rate curves of the slurries with 55 wt% solid and 2, 3 and 4 wt% CMC: (a) fine, (b) medium and (c) coarse powder size

Increasing solid content to 60 wt% increases the shear stresses further with increasing CMC addition (Figures 7.8(a), (b) and (c)). At this solid content, fine powder slurry exhibits unmeasurable shear stress increase when CMC addition is 4 wt% (Figure 7.8(a)). Accordingly, the increase in CMC wt% also causes the increase of average viscosities of all slurries with 50, 55 and 60 wt% solid content as shown in Figures 7.9(a), (b) and (c), respectively.

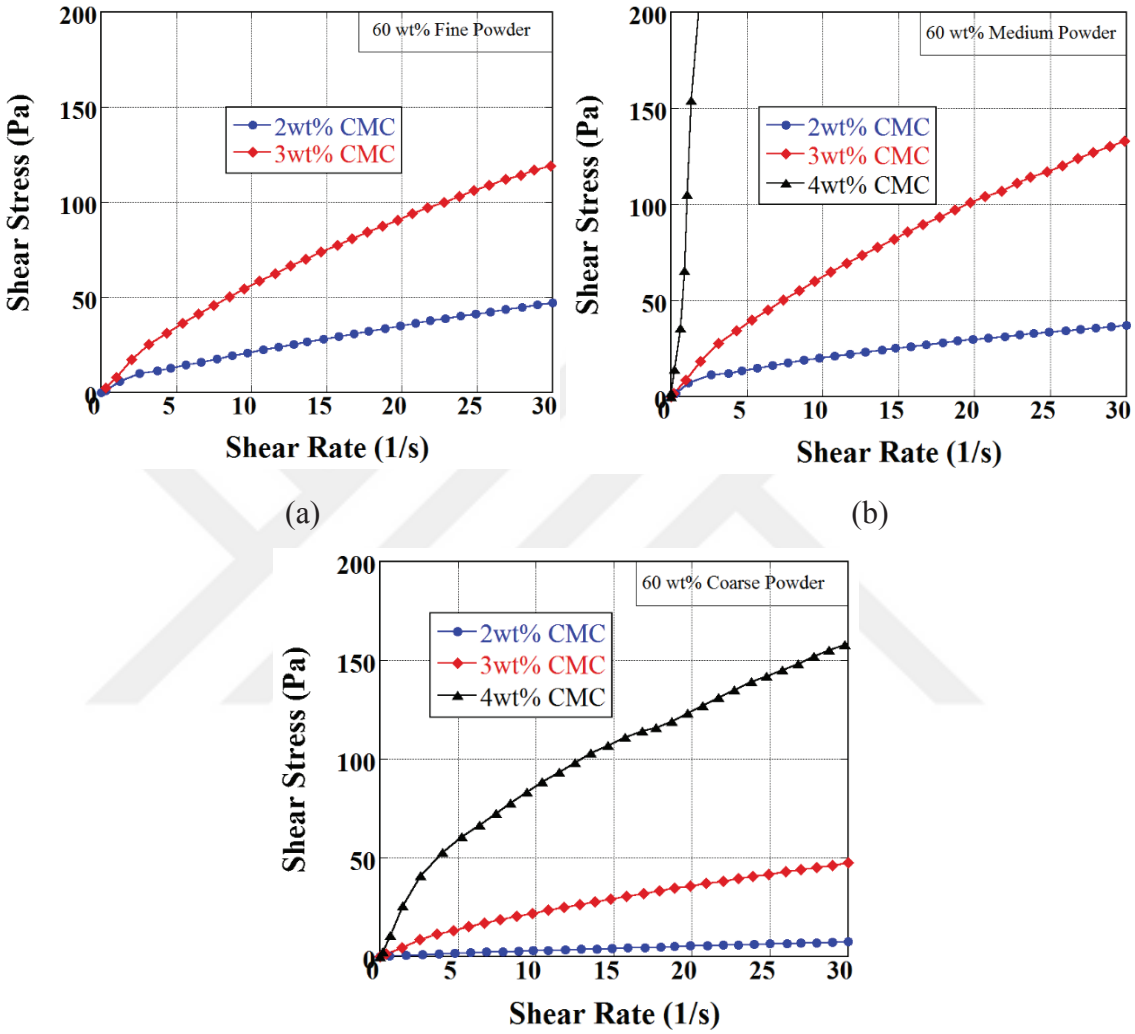

Figure 7.8. The shear stress-shear rate curves of the slurries with 60 wt% solid and 2, 3 and 4 wt% CMC: (a) fine, (b) medium and (c) coarse powder size

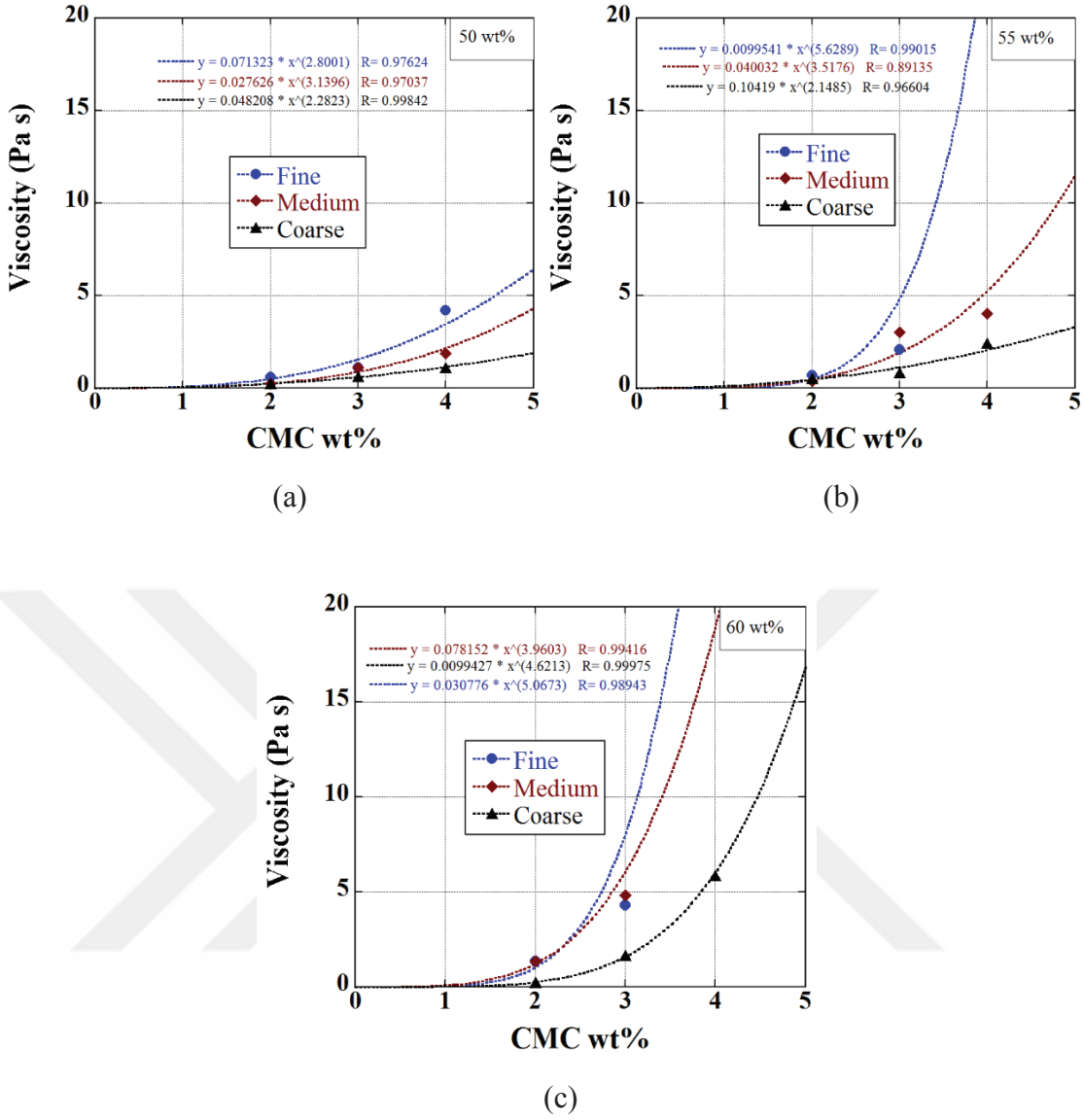

Figure 7.9. The average viscosity vs. CMC wt% of the slurries with (a) 50, (b) 55 and (c) 60 wt% solid content at 20 s^{-1} shear rate

7.3. Characteristics of Foam Expansion

Two types of linear expansion behavior are observed in the foaming experiments which are dominantly dependent on the solid content of the slurries. The expansion and time curve of 50 wt% solid content slurries is basically consisted of 4 foaming stages as marked in the figure 7.10 with the numbers in the circles through 1 to 4. The bubble formation initiates at the stage 1. In the stage 2, expansion rate increases immediately, and bubbles are formed in a steady-state expansion rate. In stage 3, the expansion rate decreases until reaching the maximum expansion point. In stage 4, the final height of the

expanded foam stays stabile for this kind of slurries prepared in 50 wt% solid content. This type of expansion behavior will be defined as “stable” in the following pages.

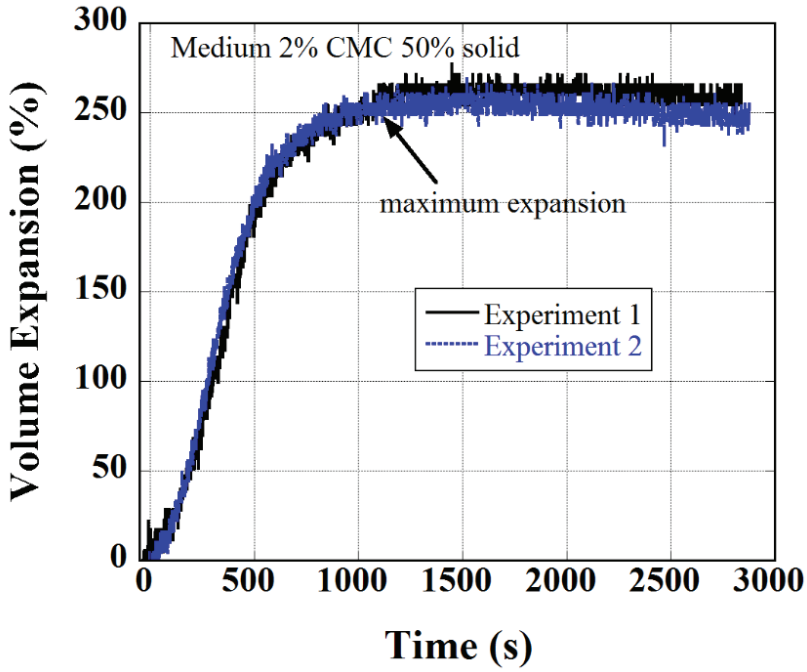

(a)

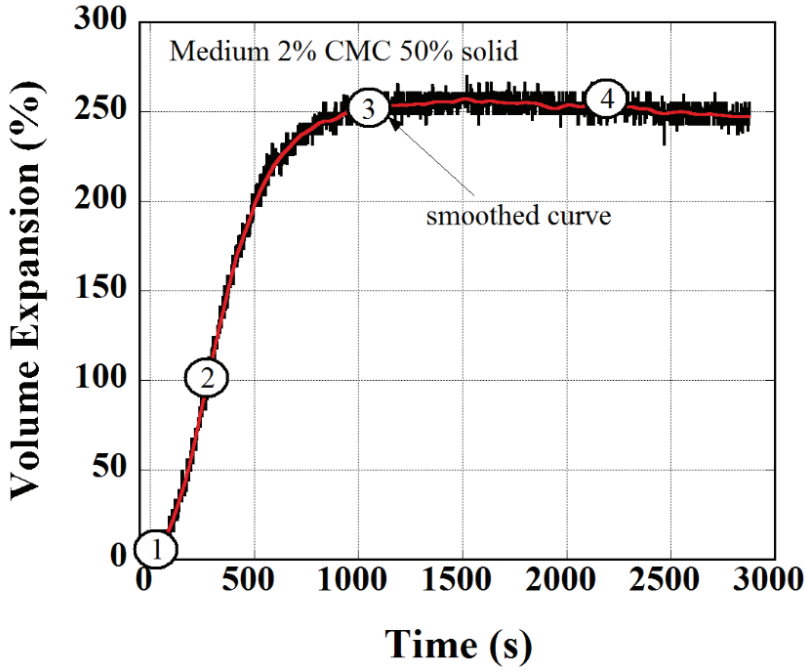

(b)

Figure 7.10. (a) Linear expansion-time curve of two foaming experiments and (b) smoothed and experimental foam expansion curves (medium powder with 2wt% CMC addition and 50% solid content)

Typical linear expansion behavior of slurries prepared in 60 wt% solid content is shown in Figure 7.11. Distinctly from the previous expansion behavior, the expanded foam does not keep its expanded structure and starts to lose its volume with a constant shrinkage rate as can be seen in stage 4. In stage 5, the foam reaches its final length. This type of expansion behavior will be defined as “unstable” in the following pages.

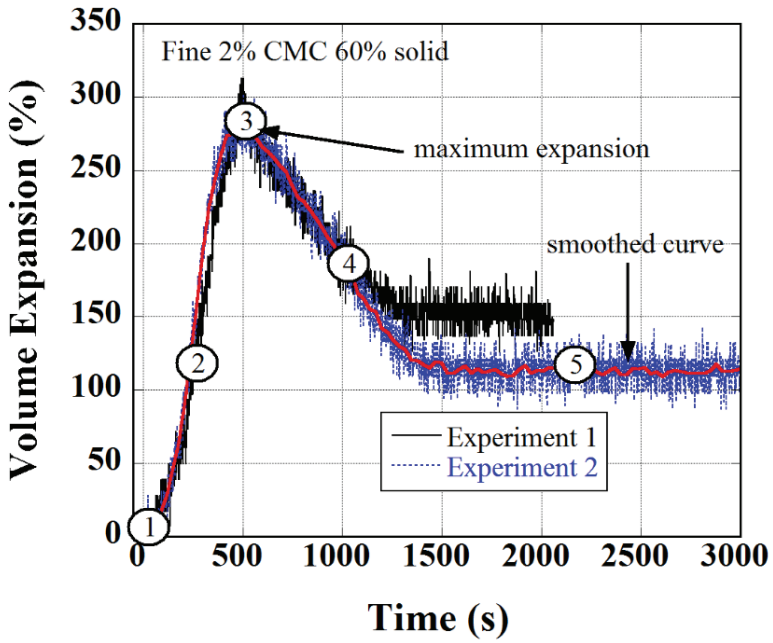

Figure 7.11. Linear expansion-time curve of two foaming experiments and smoothed and experimental foam expansion curves (fine powder with 2wt% CMC addition and 60% solid content)

The expansion behavior of slurries prepared in 55 wt% solid content was found to be in a structure between stable and unstable. Their expansion stages are found to be similar to the expansion behavior of the slurries prepared in 60 wt% solid content.

7.4. The Expansion Behavior of Slurries: Solid content and CMC Addition

The expansion behavior of slurries prepared with different particle sizes in 50 wt% solid content with no CMC addition is shown in Figure 7.12. Two separate experimentation was done for each slurry. However, as a guide to the eye, one representative curve for each parameter was shown in Figure 7.12 and the following linear expansion curves. The foaming was succeeded with no CMC addition as can be seen on

the figure. However, the slurries prepared with these parameters did not keep their expanded structure and were collapsed after drying in the stove since the water was evaporated and nothing could bind the particles. Therefore, CMC binder was used in the following experiments. Varying the particle size resulted in insignificant effect on the foaming for these parameters. Also, it can be expressed that the expansion amount of slurries with no CMC was smaller than slurries with CMC addition, which will be seen on following foaming curves.

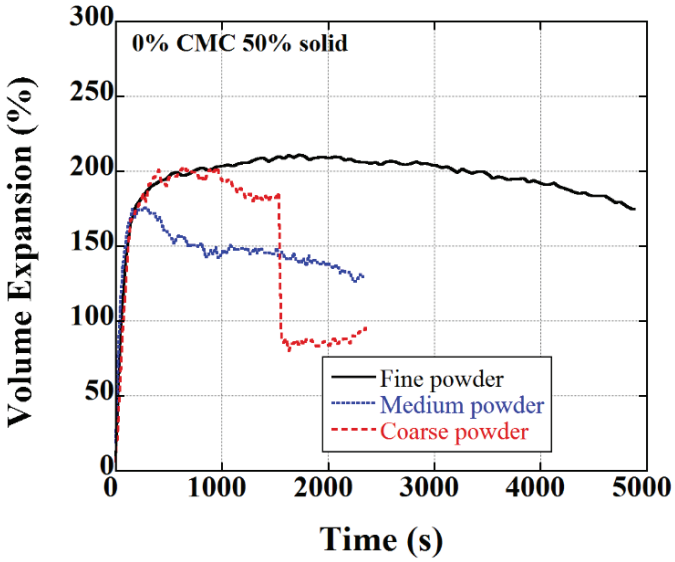

(a)

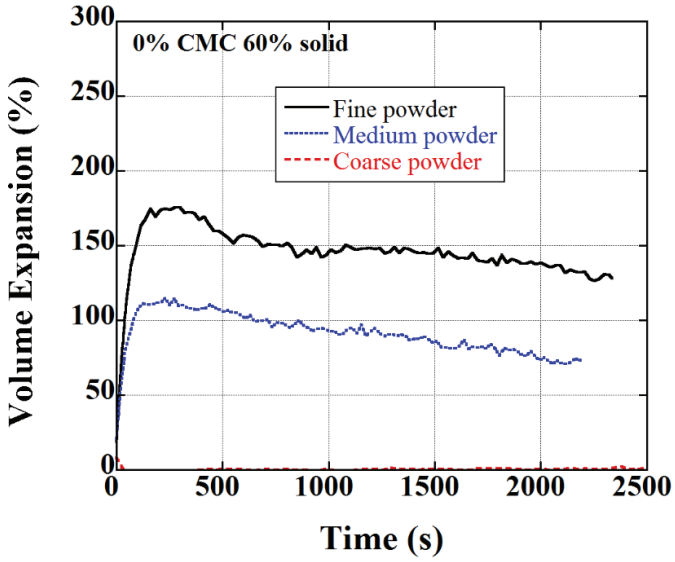

(b)

Figure 7.12. The expansion-time curves of slurries prepared with no CMC addition and different powder sizes (a) 50 and (b) 60 wt% solid content

The expansion behavior of slurries prepared with different particle sizes in 50 wt% solid content with 2, 3, and 4 wt% CMC addition are shown in Figure 7.13. In this state, all the foaming behaviors were found to be stable. The whole powders in different sizes were expanded as close to the each other since their viscosity values were found to be close to each other.

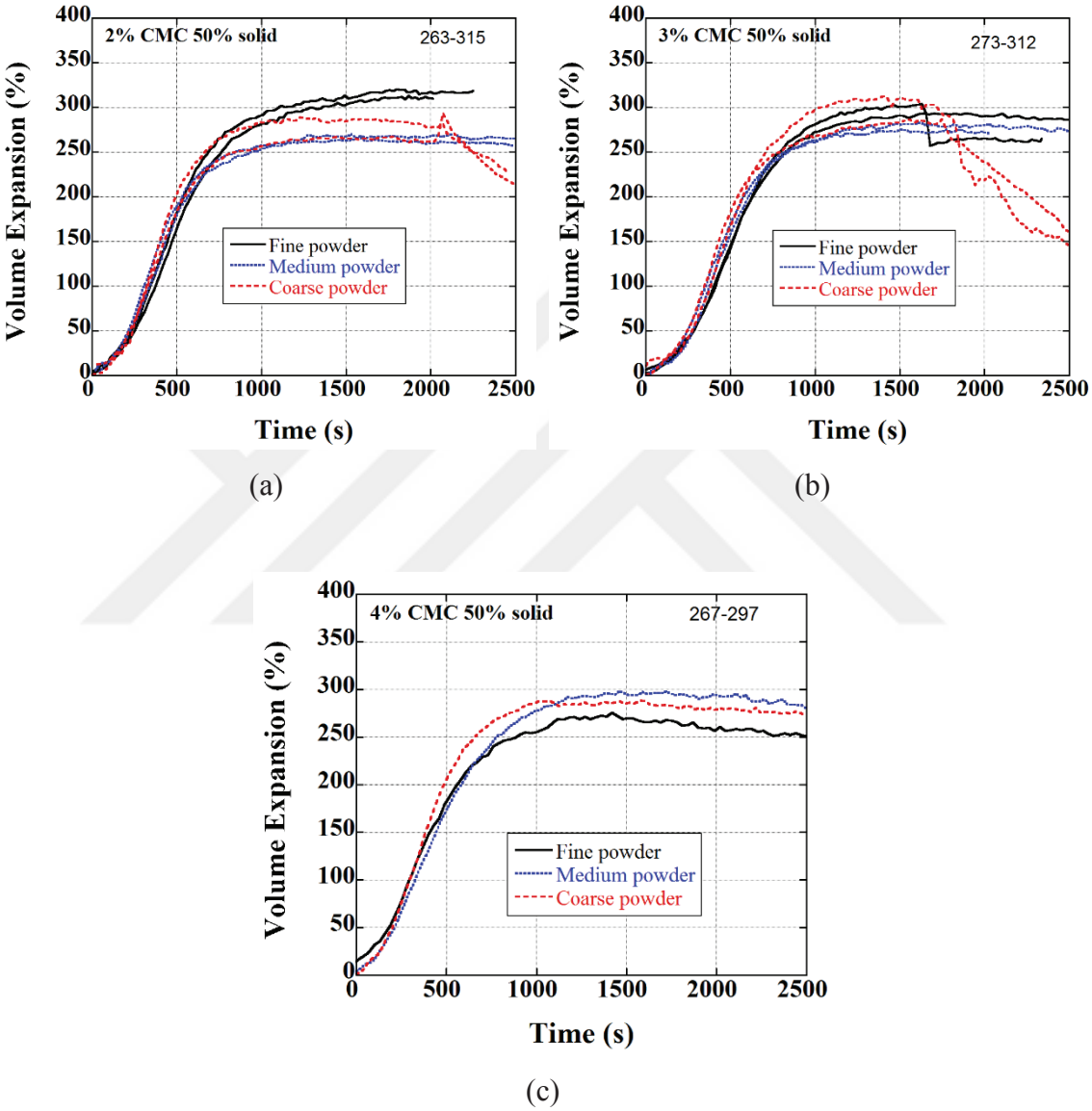

Figure 7.13. The expansion-time curves of slurries with 50wt% solid content (a) 2, (b) 3 and (c) 4wt% CMC

The expansion behavior of slurries prepared with different particle sizes in 55 wt% solid content with 2, 3 and 4 wt% CMC addition are shown in Figure 7.14. The maximum expansion amount was observed in the slurries prepared with medium size particles, but

their expansion amounts were similar to each other. The expansion behavior of these slurries is similar to samples in 50 wt% solid content. A small amount of shrinkage occurs after the reaching the maximum expansion point in these slurries.

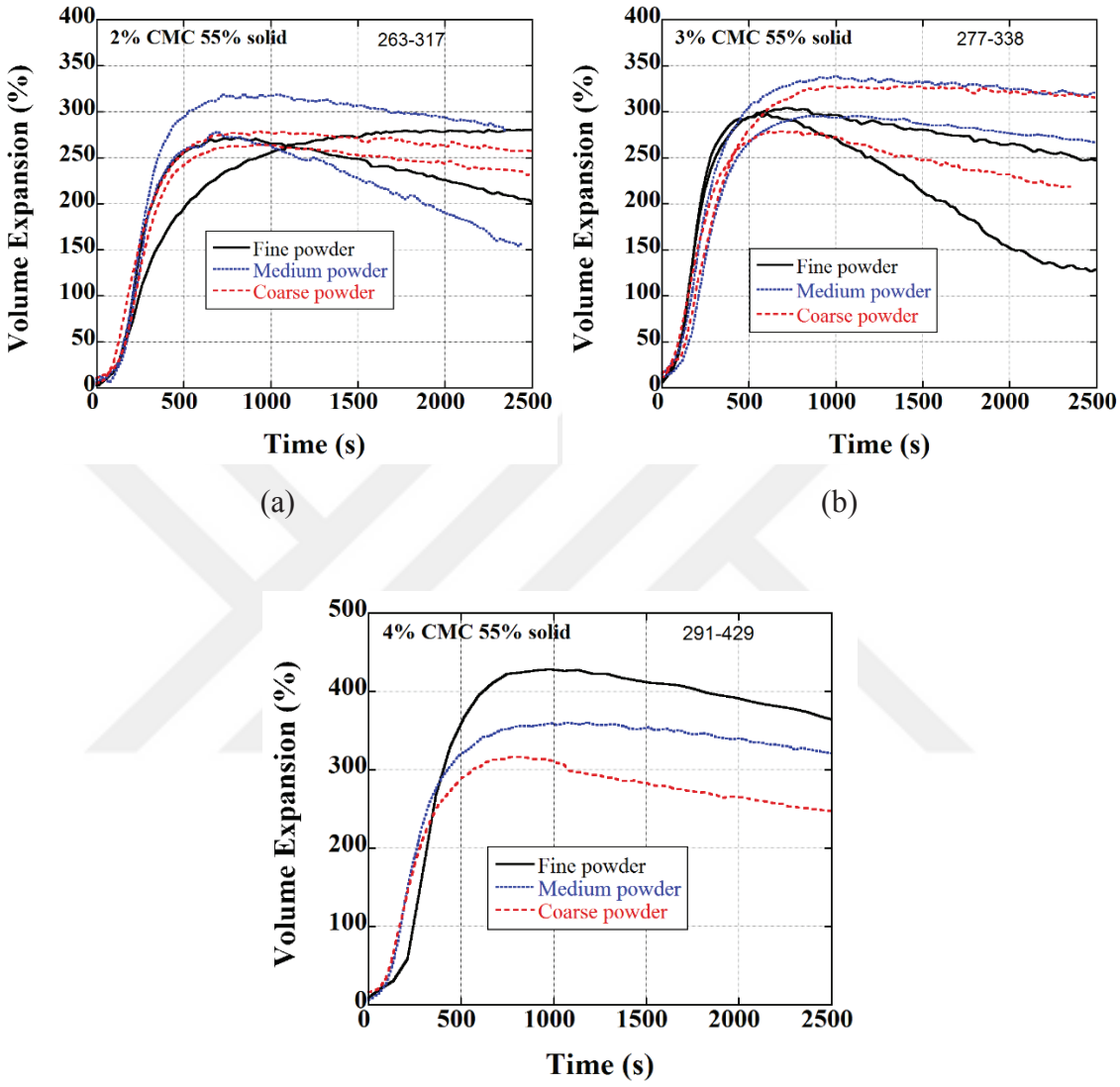

Figure 7.14. The expansion-time curves of slurries with 55wt% solid content (a) 2, (b) 3 and (c) 4wt% CMC

The expansion behavior of slurries prepared with different particle sizes in 60 wt% solid content with 2, 3, and 4 wt% CMC addition is shown in Figure 7.15. In this state, all the foaming behaviors were observed unstable. Shrinkage occurs after the reaching the maximum expansion point in these slurries. Also, expansion rate is higher than the other slurries prepared with 50 wt% and 55 wt%.

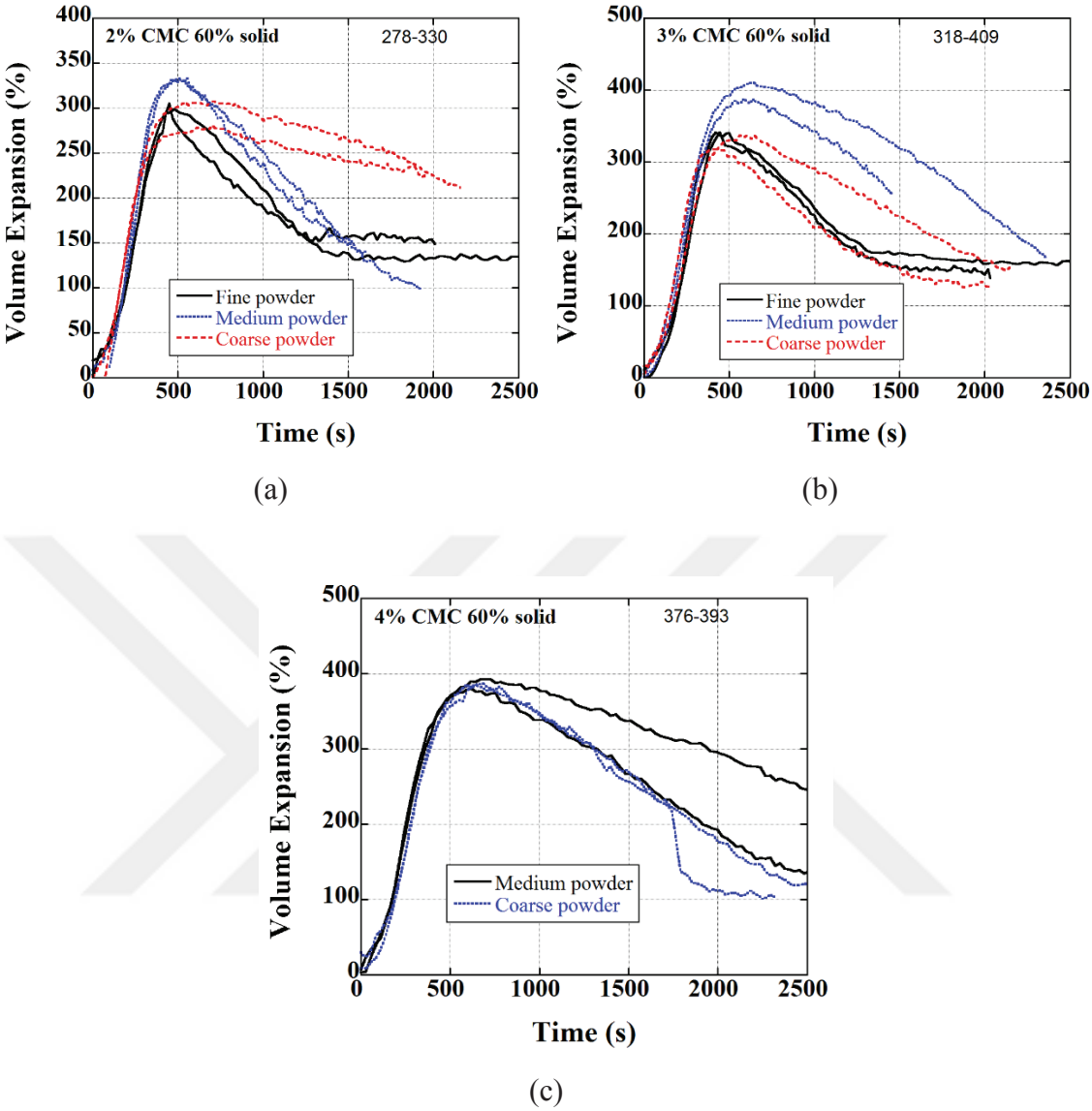

Figure 7.15. The expansion-time curves of slurries with 60wt% solid content (a) 2, (b) 3 and (c) 4wt% CMC

The representative expansion-time curves of fine, medium and coarse powder slurries with different solid and CMC content are shown sequentially in Figure 7.16, Figure 7.17 and Figure 7.18. The numbers inside circles show CMC content in these curves and arrows show solid content. In the same figures, the corresponding expansion-time curves of the slurries without CMC addition are also shown for comparison. These curves are shown in the curves with solid and filled-circle points and the solid contents are shown on the expansion curves.

The addition of CMC increases the expansions of fine powder slurries compared to without CMC added slurries (Figure 7.16). The maximum expansions of 50, 55 and 60% solid content slurries are very similar except the slurry with 55% solid and 4% CMC content. In this slurry the expansion is over 400% and in other slurries it is nearly 300%. Except 50% content slurry, the increase of CMC addition increases the expansions, while the slurry with 60% could not be prepared. Expansion rate of 55 and 60% solid content slurries rate is similar and it is higher than that of 50% solid content slurries.

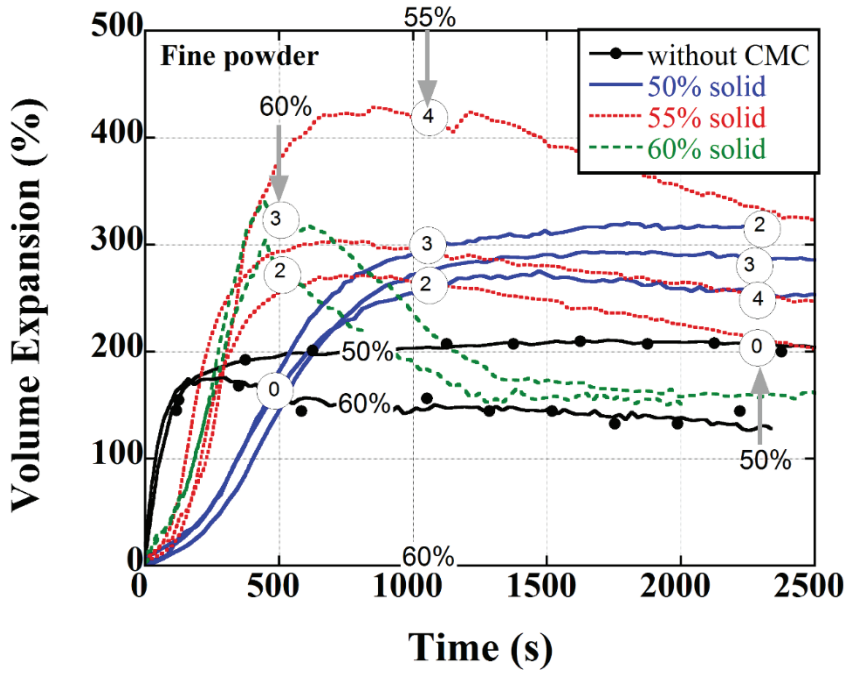

Figure 7.16. The expansion-time curves of fine powder slurries with different solid and CMC content

The maximum expansions of medium size powder slurries increase with increasing both CMC addition and solid content as shown in Figure 7.17. The maximum expansion is seen in 60% solid content slurries with 3 and 4 wt% CMC addition. The maximum expansion is nearly 400% in these slurries, the maximum expansions in 55% solid content slurries with CMC addition are higher than 300% and the maximum expansion of 50% solid content slurries is nearly 300%. Again, a lower expansion rate is seen in 50% solid content slurries compared to 55 and 60% solid content slurries.

When solid content increases to 60%, the expansion rates of the slurries become similar (Figure 7.18). The expansions of 50 and 55% solid content slurries are very similar, over 250 and below 300%, no effect of CMC addition on maximum expansions

are seen in CMC added slurries. The maximum expansion of 60% slurries on the other side increase with increasing CMC content; sequentially 300%, 340% and nearly 400% with 2, 3 and 4% CMC addition.

For all powder slurries, the expansion declines sharply after maximum expansion when the maximum expansion is high, ~400%. In these slurries the expansion rate is also higher. Such slurries correspond to 4% CMM-added 55% slurry in fine powder, 3 and 4% CMC-added 60% slurries in medium powder and 4% CMC-added 60% slurry in coarse powder.

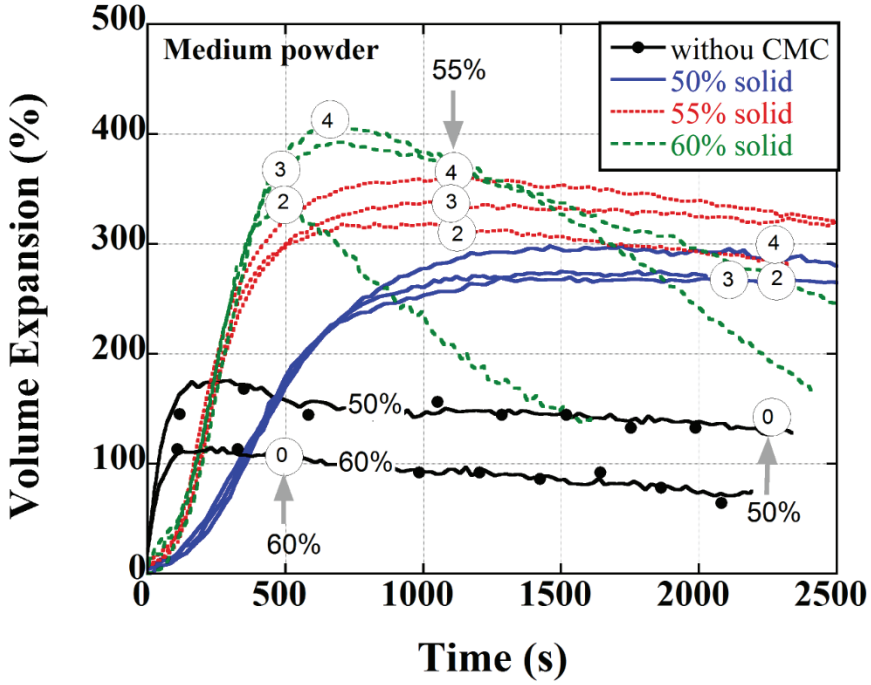

Figure 7.17. The expansion-time curves of medium powder slurries with different solid and CMC content

Figure 7.19 shows the expansion-time curves of medium powder with 4% CMC addition and 55% and 50% solid content and the corresponding foam expansion pictures. A Plexiglas (transparent) mold was used to accommodate slurries in these experiments. Although the expansion values do not represent the real expansions in Teflon mold, they can show the trends of the expansion behavior of the slurries. The rapid rise of 55% solid content slurry is seen in the same figure, within 1000 s the slurry reaches the maximum. While the expansion rate in 50% solid slurry is rather slower and the maximum expansion is reached at about 1500 s.

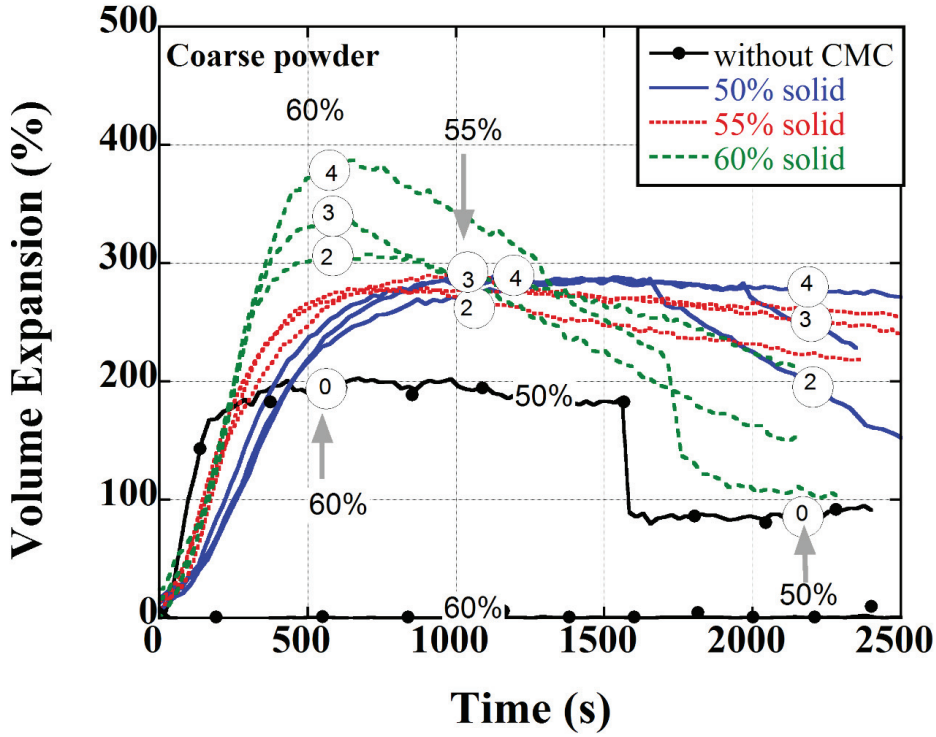

Figure 7.18. The expansion-time curves of coarse powder slurries with different solid and CMC content

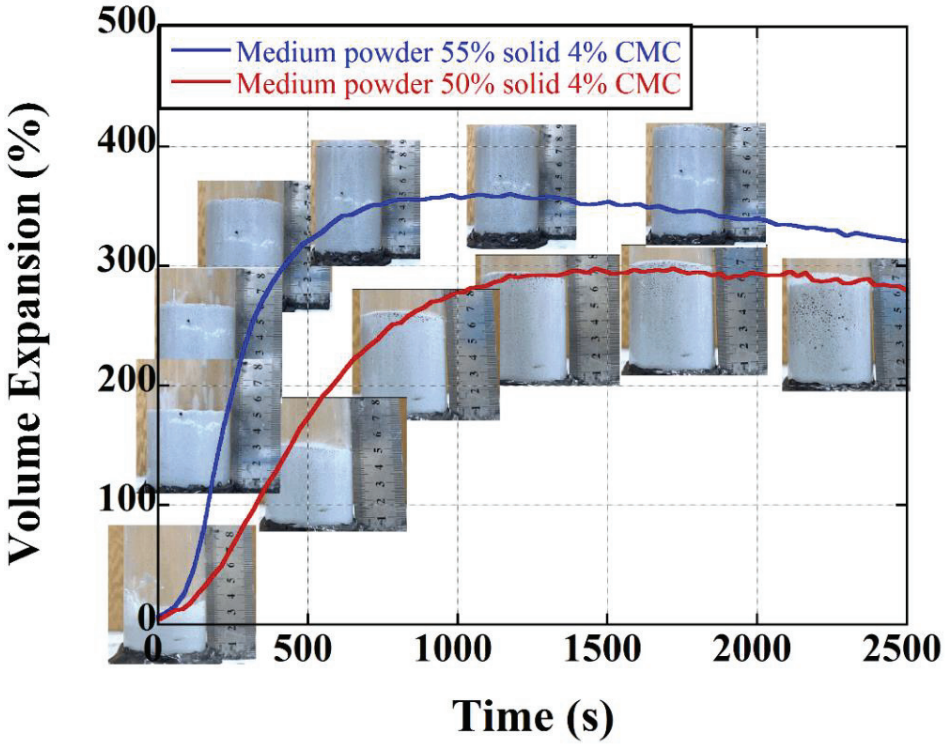

Figure 7.19. The expansion-time curves of medium powder with 4% CMC addition and 55% and 50% solid content and the corresponding foam expansion pictures

The variation of maximum expansion with log viscosity of 50, 55 and 60% solid content slurries are shown in Figure 7.20. The expansion of the slurries with CMC addition is also shown as without CMC addition with a dashed line, 200% on the average. Addition of CMC increases the expansions from 200 to 300% at low viscosities, ~0.22 Pa s. Between this viscosity and ~5 Pa s the expansions increase until about a critical velocity of 5 Pa s. At this velocity and till 50 Pa s the expansions increase over 400%, remaining almost constant. The expansion above this viscosity the slurry cannot be foamed as being very thick.

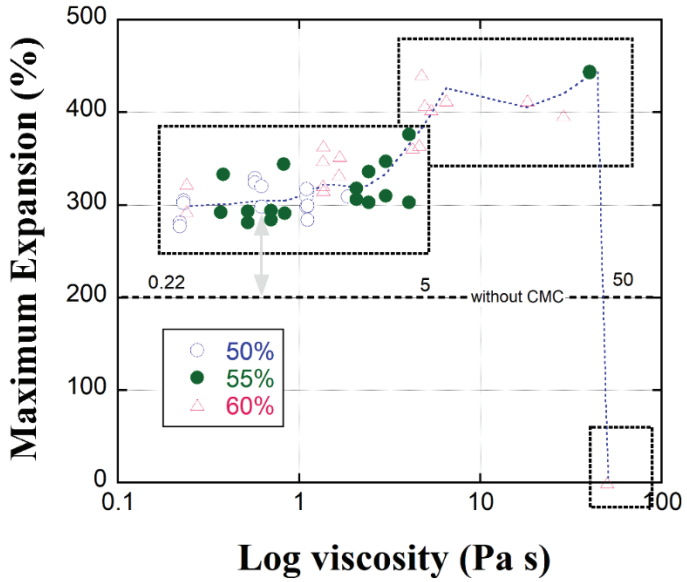

Figure 7.20. The variation of maximum expansion with log viscosity

7.5. Bubble Distribution

The variations bubble diameter of medium powder slurry with 4 wt% CMC addition as function of time are shown in Figures 7.21 (a-c) for 50, 55 and 60 wt% solid contents, respectively. The bubble size in 50wt% solid content slurry is less than 0.5 mm after 7 minutes of foaming (Figure 7.21(a)). As the foaming time increases to 9 minutes, the bubble size increases over 0.5 mm and the size distribution gets wider. Further increase in bubble size and widening in bubble size distribution are seen after 16- and 20-minutes foaming. The bubble size and distribution are seen to saturate after 25 minutes foaming in 50wt% solid content slurry. The bubble size and distribution in 55 and 60wt% solid content slurries are very much similar to each other as seen in Figures 7.21(b) and

(c). At the beginning of foaming, after 7 minutes, the maximum diameter of bubbles is slightly over 0.5 mm. As the foaming time increases to 9 minutes, the bubble size does not change significantly, but after 12 minutes of foaming time the bubble size and distribution are seen to saturate these slurries. Figure 7.22 shows the bubble size distribution in 50, 55 and 60 wt% solid content slurries after 9 and 25 minutes of foaming time. The rapid increase of bubble size of 50 wt% slurry is clearly seen in this figure, while the bubble size increase in 55 and 60wt% solid content slurries are comparatively slower. The bubble size distribution is also wider for 50 wt% solid content.

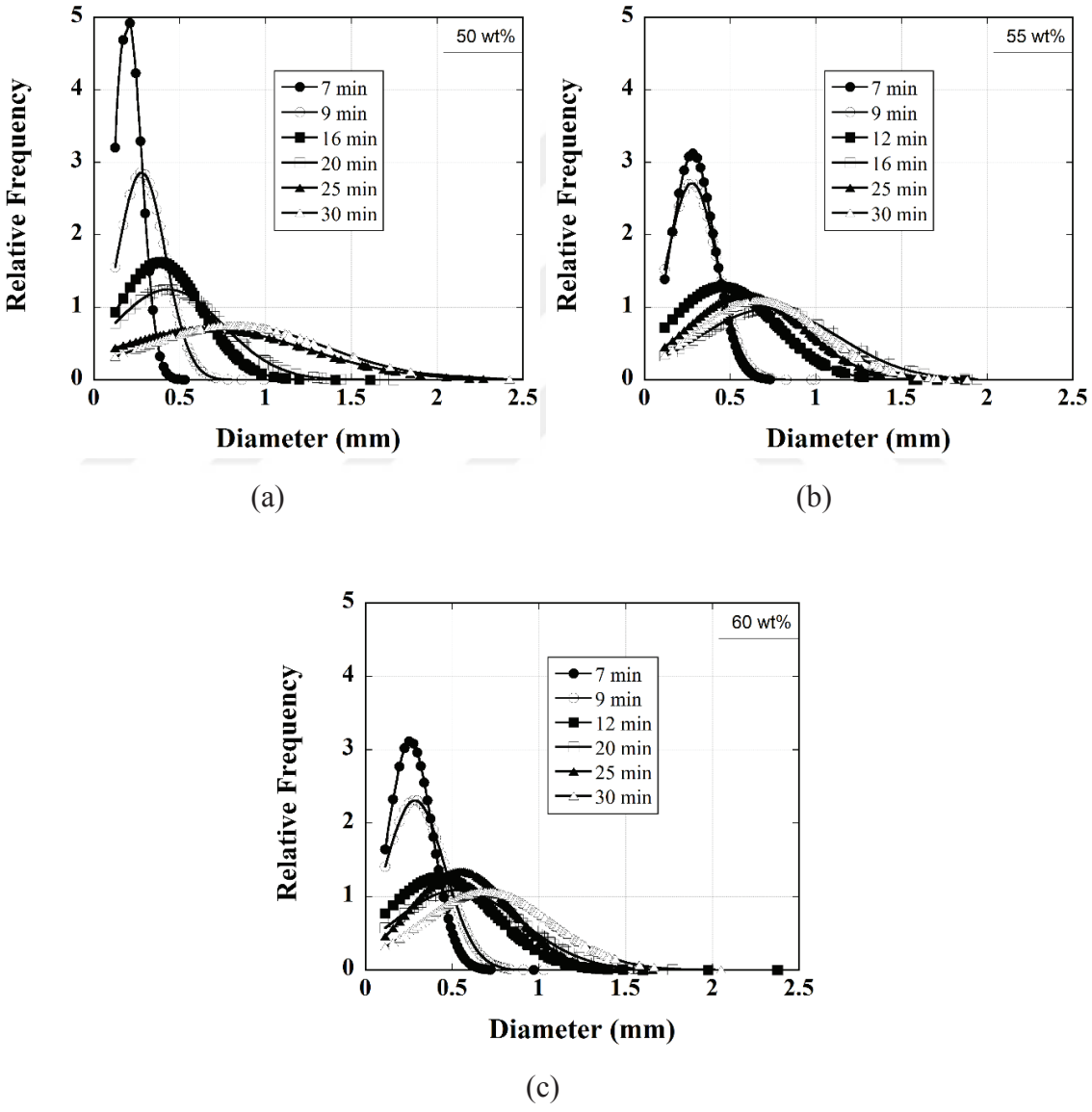

Figure 7.21. The variations bubble diameter of medium powder slurry with 4 wt% CMC at different foaming times a) 50 b) 55 c) 60 wt% percent solid contents

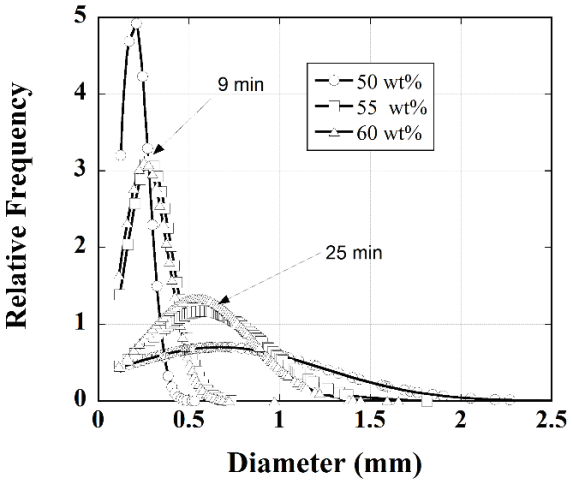

Figure 7.22. The variations bubble diameter of medium powder at 9 and 25 minutes with different solid content

7.6. 3^3 Full Factorial Design of Experiments

The analysis of variance (ANOVA) with a 3-level factorial design was used to determine the impact of factors and their levels on the results. was used in ANOVA. The factors along with their levels and their responses are tabulated in Table 7.2. 3-level factorial design requires 3^3 different experiments to be done. Since, three measurements were performed for each response, the mean values were included in the design. The Design Expert 11 Software was used to determine the significance of each factor. The experimental results of the 27 different types of the specimens, which is suitable for the experimental design theory, can be seen on Table 7.2.

The ANOVA table for Response 1 (maximum expansion) is shown in Table 7.3. The average maximum expansion was 324.31 with a standard deviation 20.27 and a R^2-value of 0.8256. The ANOVA table shows a significant with a p-value of 0.0001. Also, f-value of 8.42 implies that the model is significant. The factors and the levels have an impact on the maximum expansion. There is only a 0.01% chance for this f-value could occur due to noise. P-values less than 0.05 indicate the significant model terms. A, B, AB, A^2 are therefore significant model terms. Values greater than 0.1 indicate insignificant model terms. The ANOVA table also shows that the most effective factor on the maximum expansion is the solid content as it has the lowest p-value, 0.0001. The second effective factor is CMC content with a p-value of 0.0130 and the least effective factor is the particle size.

Table 7.2. Responses of the study with different factors and levels

	Factor 1	Factor 2	Factor 3	Response 1	Response 2
Specimen	A: Solid Content (%)	B: CMC Content (%)	C: Particle Size of the Glass Powder (µm)	Maximum Expansion (%)	Viscosity (Pa.s)
23	55	3	49.6	317.5	0.83
15	60	3	31	424.5	4.8
20	55	2	49.6	287	0.52
19	50	2	49.6	303.5	0.23
9	60	4	12.4	N/A	N/A
18	60	4	31	405	21.7
2	55	2	12.4	289	0.7
3	60	2	12.4	318.5	1.34
14	55	3	31	328.5	3
1	50	2	12.4	326.5	0.57
26	55	4	49.6	319.5	2.42
10	50	2	31	279	0.22
8	55	4	12.4	290	4.2
12	60	2	31	356	1.34
27	60	4	49.6	408	5.86
13	50	3	31	291	1.1
11	55	2	31	312.5	0.38
16	50	4	31	291	1.11
22	50	3	49.6	309	0.62
21	60	2	49.6	308	0.24
4	50	3	12.4	312	1.11
25	50	4	49.6	308	1.11
17	55	4	31	339.5	4.03
7	50	4	12.4	290.14	4.2
5	55	3	12.4	312	2.07
6	60	3	12.4	363.5	4.29
24	60	3	49.6	343	1.67

Table 7.3. ANOVA table for response 1 (maximum expansion)

Source	Sum of Squares	Df	Mean Square	F-value	p-value	
Model	31121.77	9	3457.97	8.42	0.0001	Significant
A-Solid Content	17887.72	1	17887.72	43.53	< 0.0001	
B-CMC Content	3206.30	1	3206.30	7.80	0.0130	
C-Particle Size of the Glass Powder	19.04	1	19.04	0.0463	0.8323	
AB	3857.07	1	3857.07	9.39	0.0074	Significant
AC	0.5626	1	0.5626	0.0014	0.9709	Not significant
BC	839.08	1	839.08	2.04	0.1722	Not significant
Residual	6574.68	16	410.92			
Cor Total	37696.45	25				

The ANOVA diagnostics normal probability plot of residual and predicted vs. actual graphs of maximum expansion are shown in Figured 7.23(a) and (b), respectively. Figure 7.23(a) indicates that the highest maximum expansion is an outlier. One outlier is accepted to be reasonable for statistics. In Fig. 7.23(b), it shown that the model well predicts the experimental data with adjusted R^2-value of 0.8256.

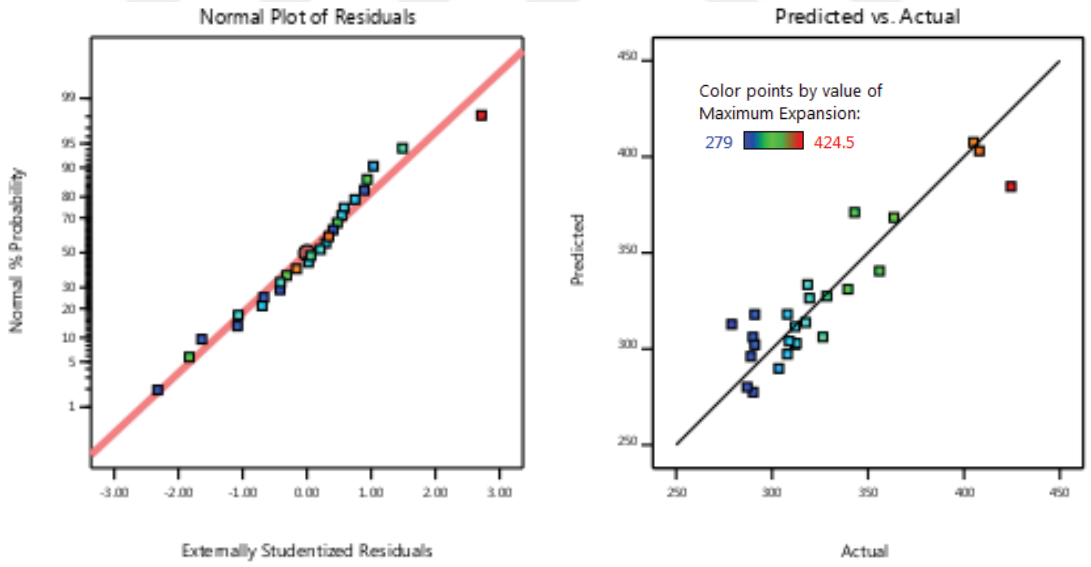

(a) (b)

Figure 7.23. ANOVA diagnostics a) Normality plot of residual b) Predicted vs actual plot according the Response 1 (Maximum Expansion)

ANOVA table for the Response 2, viscosity, is tabulated in Table 7.4. The average viscosity was 2.68 Pa.s with a standard deviation of 3 and an R^2-value of 0.8576. The

ANOVA table shows that the model is significant with a p-value of 0.0029 and with an f-value of 5.07. The factors and the levels are therefore having impact on the viscosity. The chance of being a large f-value due to noise is 0.01%. The ANOVA table shows that the most affective factors on viscosity are the solid content and the CMC content (the lowest p-values, 0.0032. Then, the particle size is less effective on the viscosity with a p-value of 0.1721.

Table 7.4. ANOVA table for response 2 (viscosity)

Source	Sum of Squares	df	Mean Square	F-value	p-value	
Model	273.68	6	45.61	5.07	0.0029	Significant
A-Solid Content	101.83	1	101.83	11.33	0.0032	
B-CMC Content	141.95	1	141.95	15.79	0.0008	
C-Particle Size of the Glass Powder	18.10	1	18.10	2.01	0.1721	
AB	79.73	1	79.73	8.87	0.0077	Significant
AC	4.52	1	4.52	0.5029	0.4869	Not significant
BC	9.32	1	9.32	1.04	0.3212	Not significant
Residual	170.77	19	8.99			
Cor Total	444.45	25				

The ANOVA diagnostics normal probability plot of residual and predicted vs. actual graphs of viscosity are shown in Figs. 7.24(a) and (b), respectively. Figure 7.24 (a) indicates that the highest viscosity is an outlier. In Fig. 7.24 (b), it shown that the model also well predicts the experimental data with adjusted R^2-value of 0.8256.

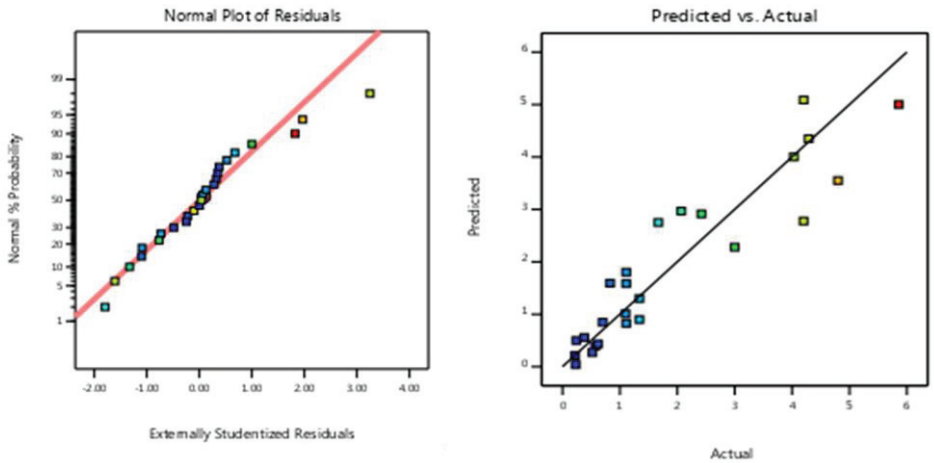

(a) (b)

Figure 7.24. ANOVA diagnostics a) Normality plot of residual and b) Predicted vs. actual plot according the response 2 (viscosity)

Figure 7.25 shows the variation of maximum expansion with viscosity. The maximum expansion is related to the viscosity with a correlation number of 0.811.

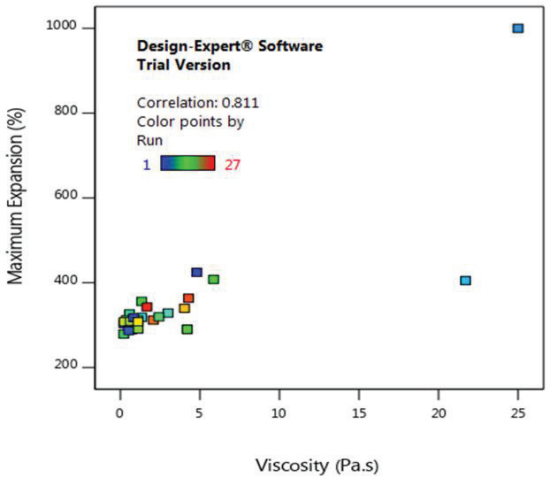

Figure 7.25. Relationship between maximum expansion and viscosity by simulating the results

7.7. Microstructural Analysis

A typical green body of foam glass (medium powder, 55 wt% solid content with 4 wt% carboxymethyl cellulose) after taken from the foaming mold is shown in Figure 7.26. Macro pores are easily seen in this micrograph.

Figure 7.26. Glass foam green body

The SEM images of the polished surface of a foam glass green body in epoxy mold are shown in Figures 7.27 (a-d) at 60, 100, 250 and 1000x, respectively. In these micrographs white areas are the glass particles on the foam cell walls and black areas are the epoxy in the pores of cells. The particles are shown in these figures are not bonded to each other and partial foam structure occurred because of the steric stabilization folding the particles together. These also proves an efficient interaction between carboxyl groups of the carboxymethyl cellulose and the surfaces of glass particles. And, both macro pores inside cells and micro pores in the cell walls are seen in the same micrographs.

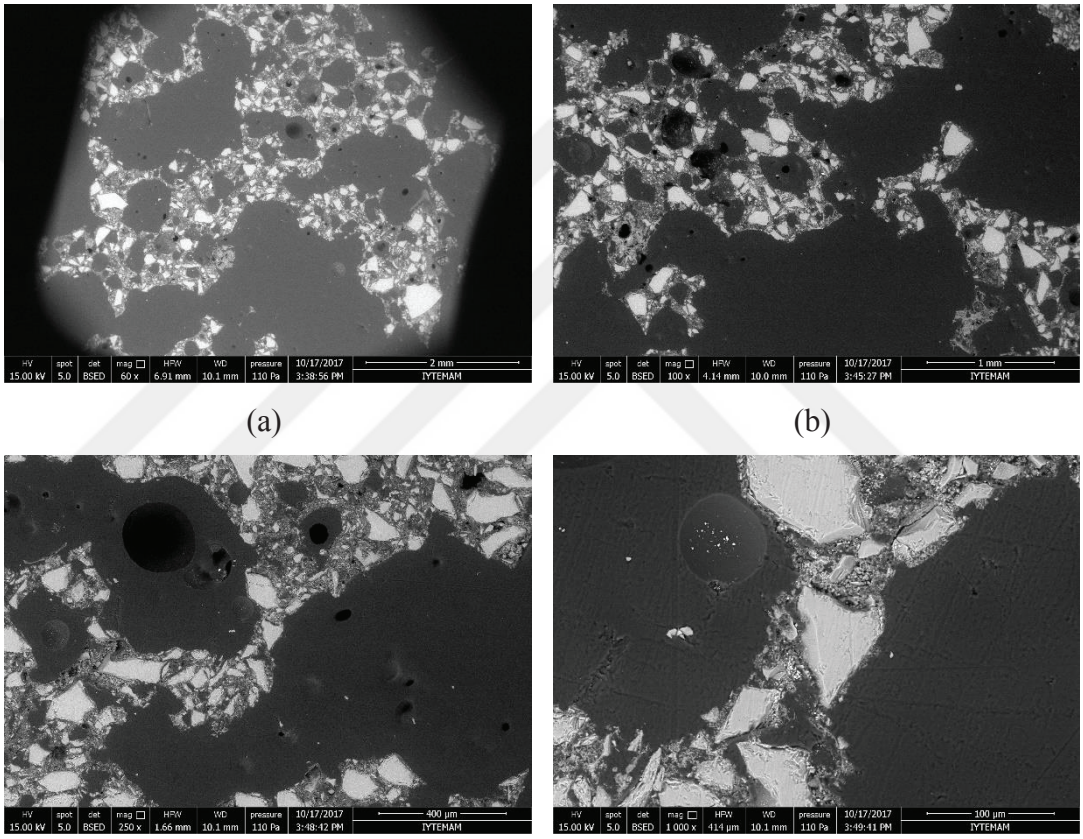

Figure 7.27. SEM images of the polished surface of foam glass embedded into epoxy matrix at different magnifications (a) 60x (b)100x (c) 250x (d) 1000x

The pictures of foam samples before and after sintering at 750 and 800 ^{o}C are shown in Figure 7.28(a-c), respectively. After sintering at 750 ^{o}C, although showed shrinkage (Figure 7.28(b)), the samples sintered at 800 ^{o}C were partially melted and the cells were collapsed (Figure 7.28(c)).

(a) (b) (c)

Figure 7.28. The pictures of foam samples (a) before sintering and after sintering at (b)750 and (c) 800 ^{o}C

The SEM surface images of the foam samples with 60 wt% solid content, foamed for 1800 s and sintered at 700 and 750 ^{o}C are shown in Figures 7.29(a) and (b), respectively. In the same figures, the facture surfaces of both foam samples are seen to contain small and large pores (shown by arrows) within the cell walls. While the amount of these pores is lowered, and the sizes increased in the foam sample sintered at 750 ^{o}C.

The facture in both samples occurs through the cell walls as seen in Figures 7.30(a) and (b). Non-complete sintering of cell walls in the foam sample sintered at 700 ^{o}C is noted in Figure 7.30(a) as large pores inside the cells. The appearance of small pores on the fractures cell walls, shown by arrow in Figure 7.30(a), also proves non-complete sintering of glass powder. It is noted that the cell walls are thicker and completely sintered in the sample sintered at 750 ^{o}C (Figure 7.30(b)). The denser cell walls are therefore separated by cleavage type of fracture as similar with bulk glass. The effect of sintering temperature is therefore to 1) increase cell wall density and 2) reduce the extent of cell wall pores.

Figures 7.31(a) and (b) show the SEM fracture surface images of the foam samples foamed until the same duration (1800 s) and sintered at 750 ^{o}C with 55 and 60 wt% solid content, respectively. A comparison between Figures 7.31(a) and (b) reveals that increasing solid content reduces the cell wall pores and induces the thicker cell walls. The presence of cell wall pores is also noted to be effective in fracture. Figures 7.32(a) and (b) show the SEM fracture surface images of the foam samples sintered at 750 ^{o}C with 55 and 60 wt% solid content, respectively. In both samples, the cracks are seen to originate from cell wall pores, as shown by arrows.

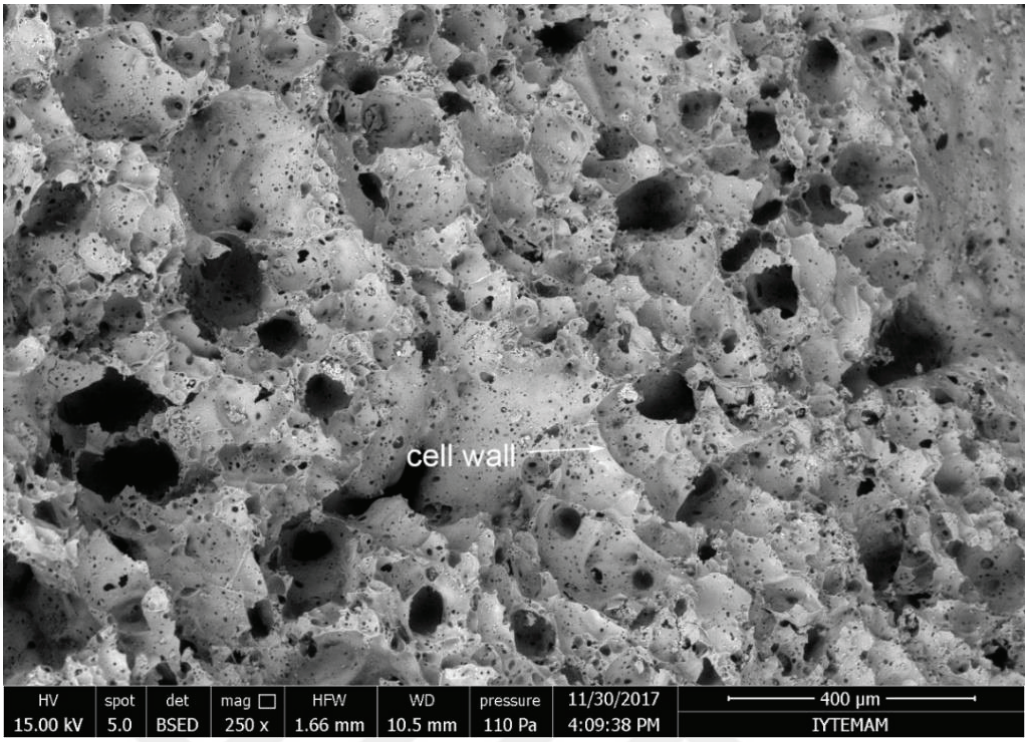

(a)

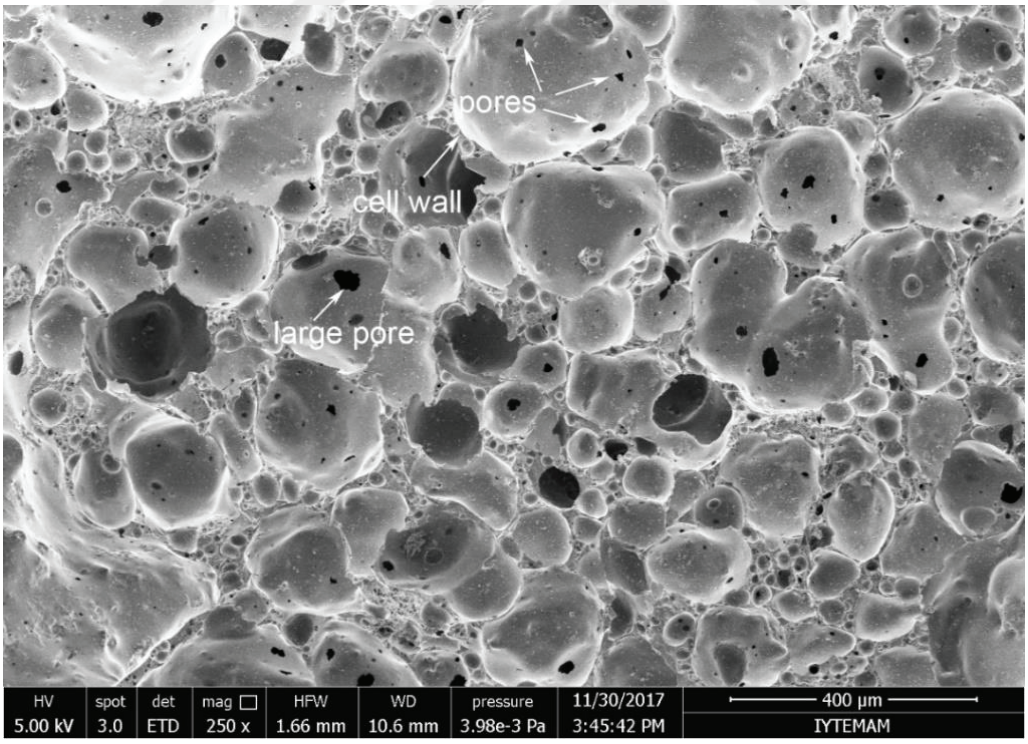

(b)

Figure 7.29. SEM images of sintered samples with 60 wt% solid content sintered at (a) 700 and (b) 750 ºC

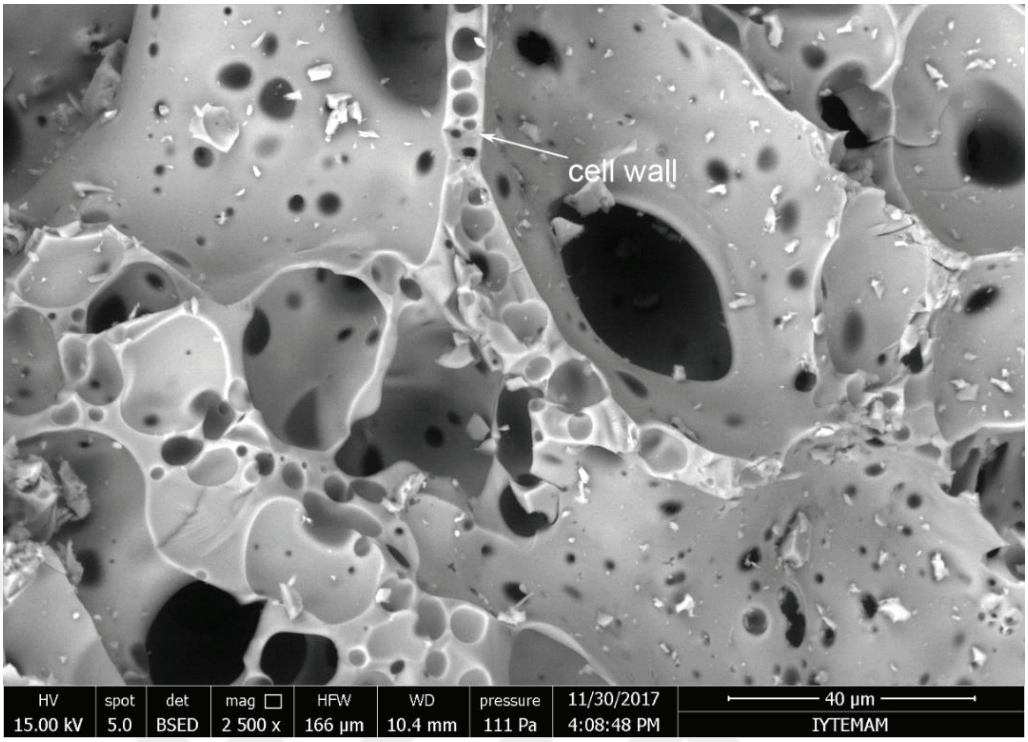

(a)

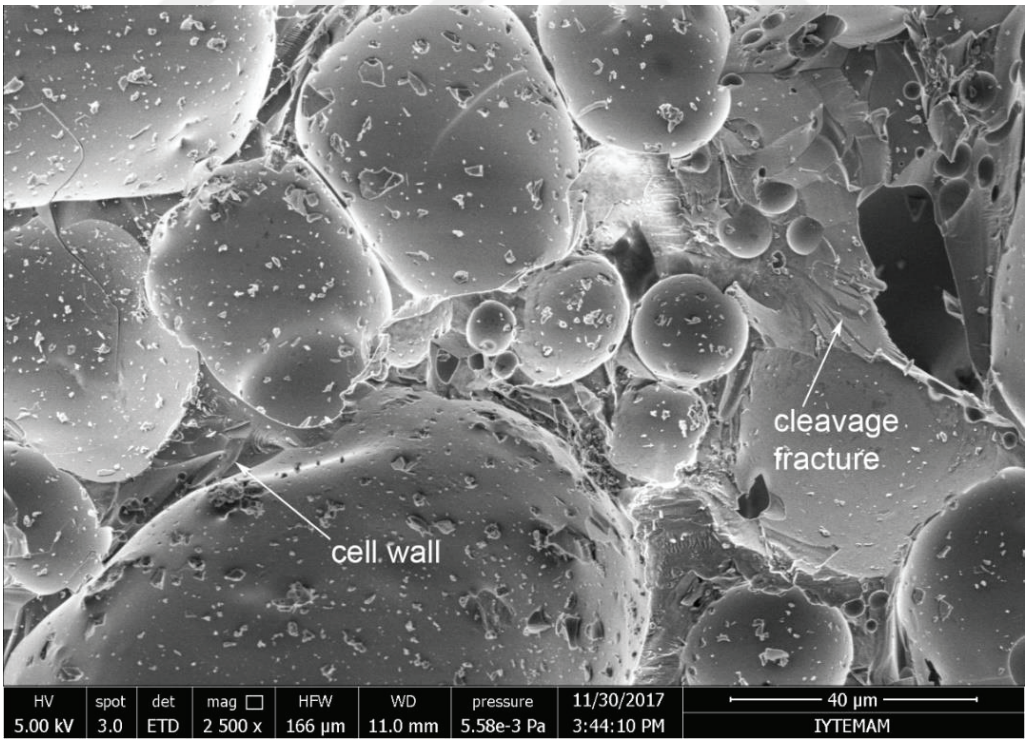

(b)

Figure 7.30. SEM images of sintered samples with 60 wt% solid content sintered at (a) 700 and (b) 750 ^{o}C showing fractured cell walls

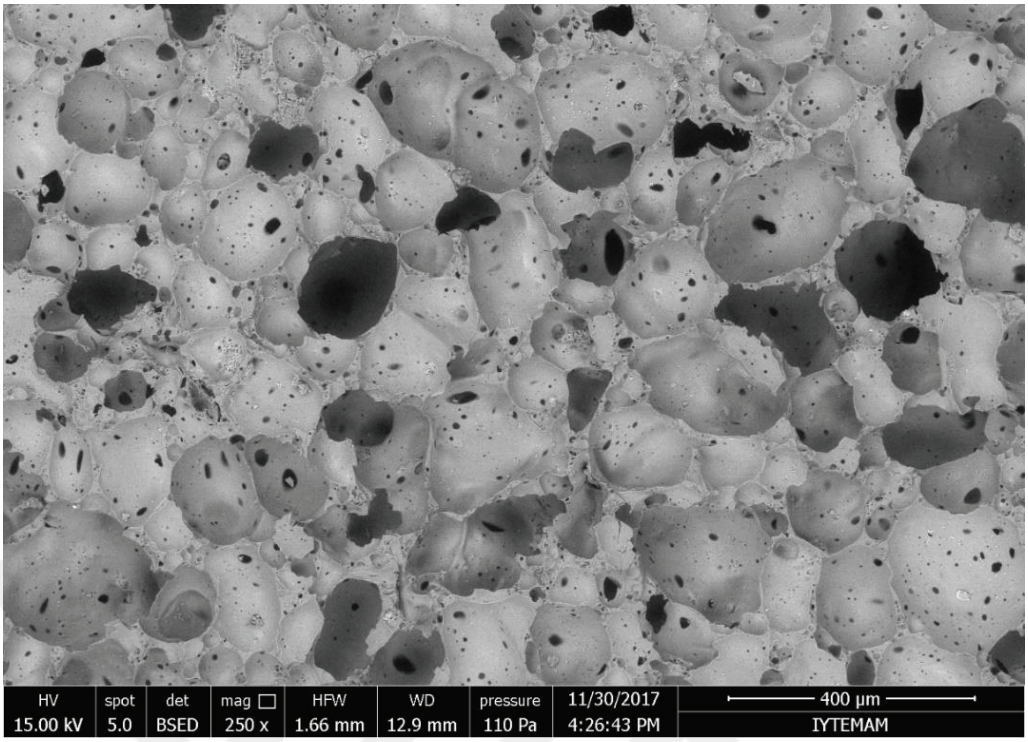

(a)

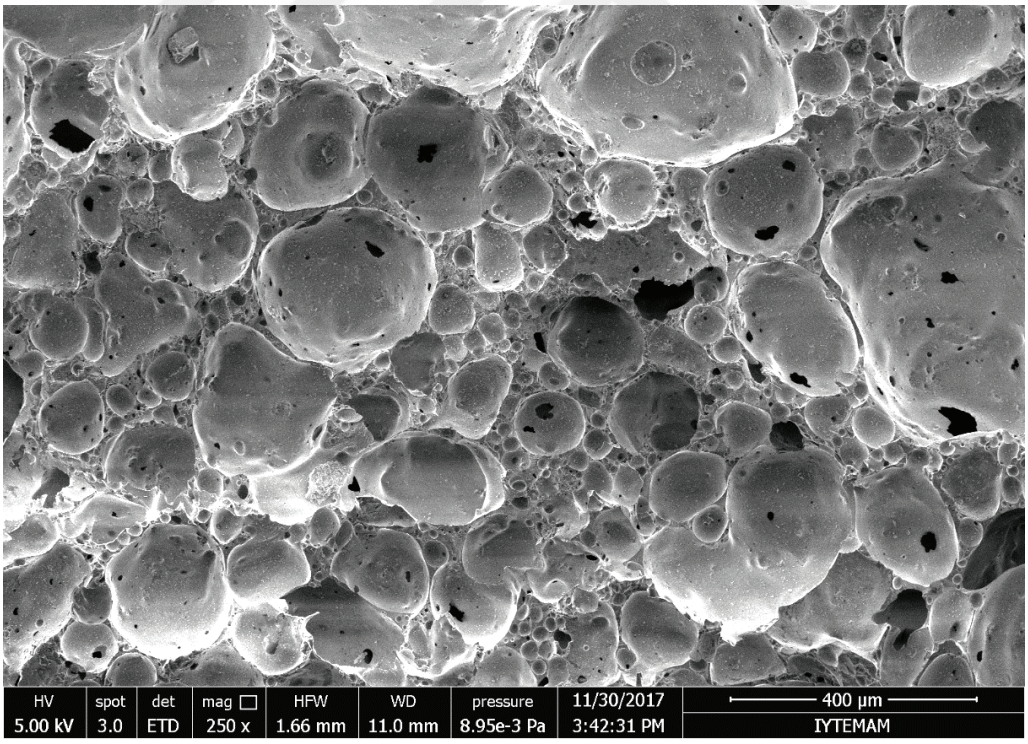

(b)

Figure 7.31. SEM images of sintered samples sintered at 750 ºC (a) 55 and (b) 60 wt% solid content

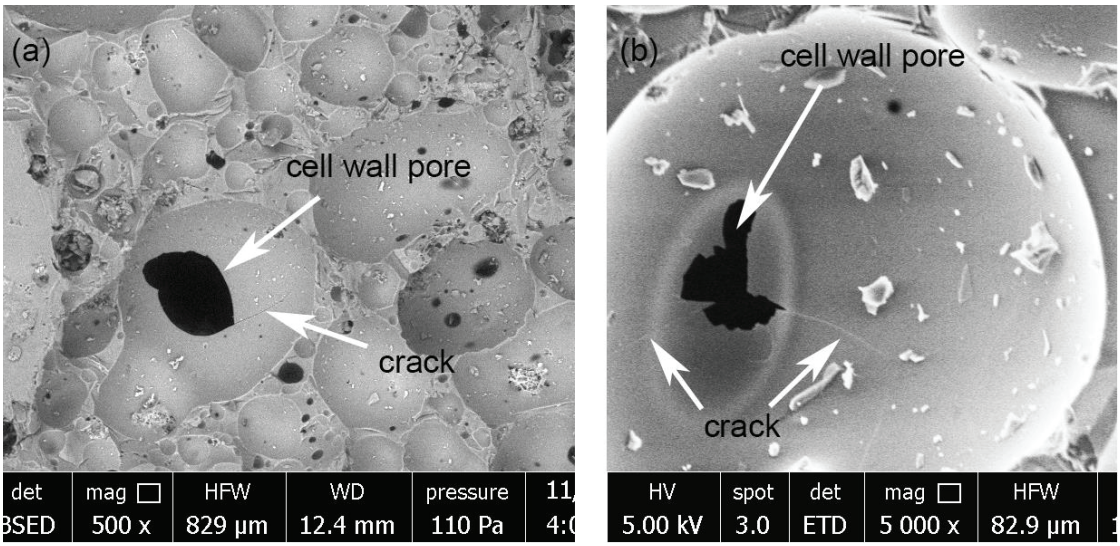

(a) (b)

Figure 7.32. SEM images showing cell wall pores in foam samples sintered at 750 ºC (a) 55 and (b) 60 wt% solid content

7.8. Compression Strength and Thermal Conductivity of Sintered Bodies

Figures 7.33(a-d) show quasi-static compression stress-strain curves of sintered foam samples with 55 and 60wt% solid content sintered at 700 and 750 ºC for 30 min, respectively. In Figure 7.33(d), the stress-strain curves of the foam sample of 60wt% solid content sintered 750 ºC for 60 min are also shown. The stress in compression test increases initially to a maximum stress and the sample fails by forming progressive facture either starting at the top or bottom of compression test plate as shown in Figure 7.34. After the failure, the sample remains in between the test plates and progressively fractures until about large strains. The initial peak before progressive fracture is taken as the compressive strength as marked in Figure 7.33(a). Except one sample, the sintered foam samples with 55 and 60wt% at 700 ºC show relatively very low compressive strength around 0.2 MP as seen in Figures 7.33(a) and (b). When the sintering temperature increases to 750 ºC both foam samples' strength values increases over 0.5 MPa. The increase of sintering time from 30 to 60 min increases the fracture strength over 1 MPa as seen in Figure 7.33(d). The average density and compressive strength of sintered foams are tabulated in Table 7.5. As tabulated in the same table, sintered foams samples with 60wt% have higher densities as compared with sample with 55wt% solid content. The

foam samples with 55 wt% solid content, density of 405 and 355 kg m^{-3} and sequentially sintered at 700 and 750 ^{o}C show average stresses of 0.15 and 0.57 MPa. The foam samples with 60 wt% solid content, density of 530 and 504 kg m^{-3} and sequentially sintered at 700 and 750 ^{o}C show average stresses of 0.32 and 0.58 MPa. Doubling the sintering time increases the average compressive strength to 1.3 MPa. These results confirmed that both sintering temperature and time are effective in increasing the compressive strength.

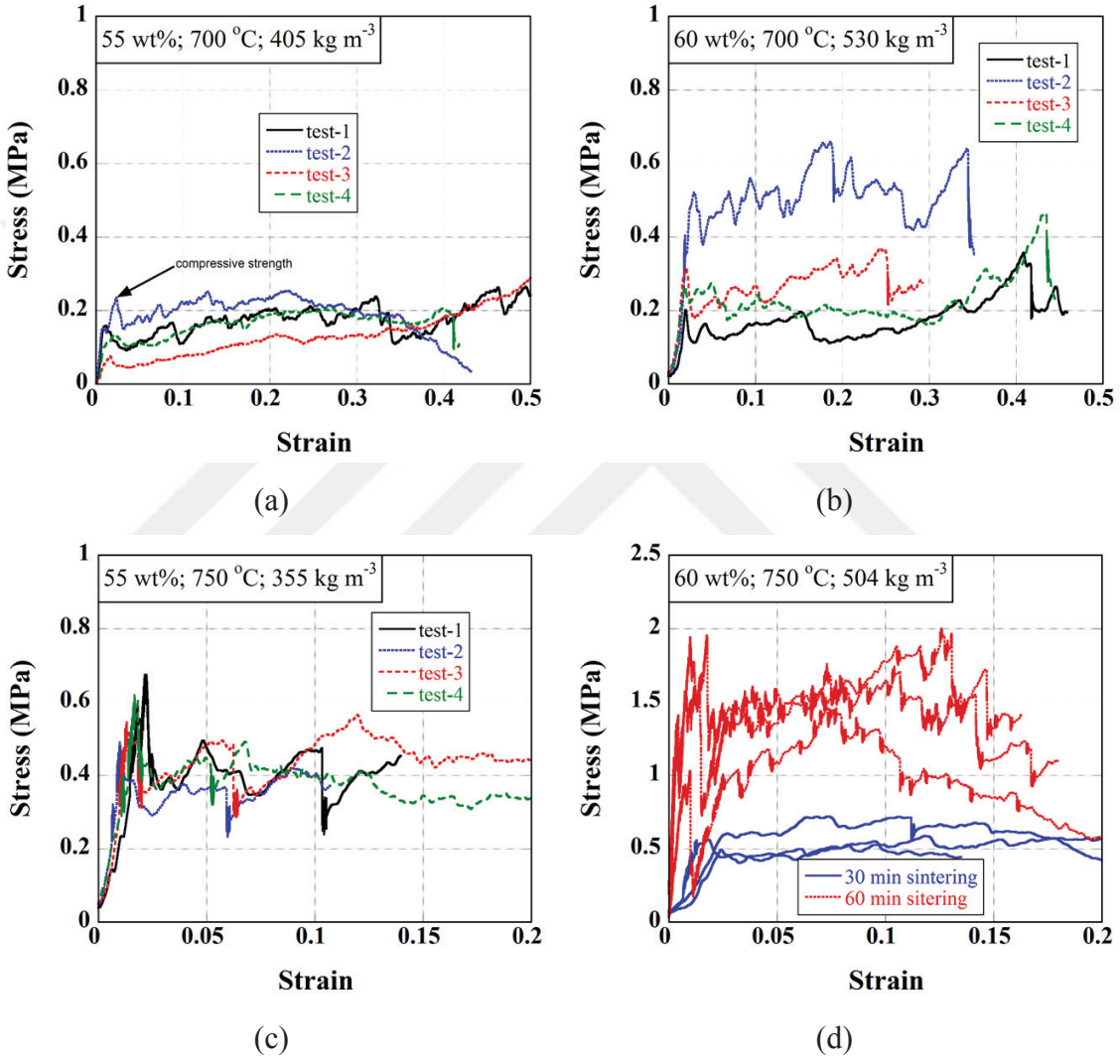

Figure 7.33 The compression stress-strain curves of the foamed and sintered samples (a) 55 wt% solid and 700 ^{o}C, (b) 60 wt% solid and 700 ^{o}C, (c) 55 wt% solid and 750 ^{o}C, (d) 60 wt% solid and 750 ^{o}C and the same foam sample sintered 60 min

The measured thermal conductivities of foam samples with 55 and 60wt% and sintered at 750^{o}C are tabulated in Table 7.6. The thermal conductivity of sintered foam

samples with 355 kg m^{-3} density is 0.042 w m^{-1} K^{-1}, while it increases to 0.057 w m^{-1} K^{-1} when the density increases to 504 kg m^{-3}.

Table 7.5. The average density and compressive strength of compression tested sintered foam samples

Sample	Average Density (kg m^{-3})	Average Compressive Strength (MPa)
55 wt% sintered at 700 °C for 30 min	405	0.15 (0.077-0.23)
60 wt% sintered at 700 °C for 30 min	530	0.32 (0.2-0.52)
55 wt% sintered at 750 °C for 30 min	355	0.57 (0.47-0.67)
60 wt% sintered at 750 °C for 30 min	504	0.58 (0.50-0.71)
60 wt% sintered at 750 °C for 60 min	504	1.3 (1.05-1.43)

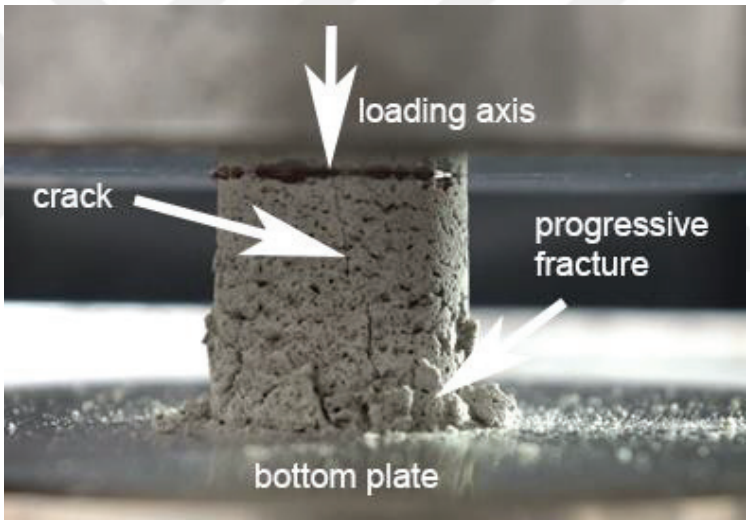

Figure 7.34. The picture of a failed sintered foam sample in compression test

Table 7.6. Thermal conductivities of sintered (750 °C) foams in different solid contents

Sample	Density (kg m^{-3})	Thermal Conductivity (W m^{-1} K^{-1})
750 °C 55 wt% Solid Content	355	0.042
750 °C 60 wt% Solid Content	504	0.057

CHAPTER 8

DISCUSSION

8.1. The Effect of Particle Size on the Viscosity and Maximum Expansion

The XRD pattern of the as-received glass powder, shown in Figure 7.1, displays a broad hump trend which pronounces its amorphous structure [76]. The XRF analysis of the powder is well matched with the literature and represents that the powder is in soda-lime glass structure [77].

Parameters like particle size, binder amount and solid content affected the viscosity and expansion behavior of slurries prepared for glass foaming. Particle size is one of the main parameters determining the rheology of ceramic slurries. The effect of particle size on the rheological behavior of ceramic slurries were previously investigated. When a system having particles with various sizes is packed closer than a system having the same size particles [78]. The particles used in the experiments, although were sieved to few particle sizes ranges, may be considered having wide particle size distribution and hence close packed. In close packed particle systems, rheological properties of the bubble surface are more pronounced than interparticle forces and steric forces [8, 78]. Since the close packing of the particles increases with decreasing of the interval of sieving decreases, the viscosity increases as the particle size decreases. However, the effect of particle on foam expansions was found to be not significant. The reason of this might come from choosing closer sieving sizes to obtain different size distributions and other experimental parameters affected the results more dominantly.

Sphericity of the particles is another important parameter affecting the viscosity of the slurries. In Krieger-Doughtery and Batchelor's model [79], the particle fraction was only considered. The effect of the particle sphericity on the viscosity of liquid-solid suspensions was investigated previously [8]. An increase in the particle sphericity resulted in a decrease in apparent viscosity. The sphericity of glass powder used in this study may be increased by applying high energy ball milling. This will be investigated as a future study.

8.2. The Effect of Solid Content and CMC Amount on Viscosity

Theoretical and experimental studies showed that the relative viscosity, μ_{rel} and solid fraction, ϕ are highly dependent to each other [78]. The variation of relative viscosity with solid fraction is summarized in Figure 8.1 [80-83]. The relative viscosity shows a rapid increase after 0.5 solid fraction. This behavior was also observed in present study. Figures 7.9(a-c) shows the average viscosity vs. CMC wt% of the slurries with 50, 55 and 60 wt% solid content. The viscosity particularly increases when the solid content is 60% for fine powder slurries. The increase in solid content causes viscosity to increase by preventing the particle flow in the slurry and by increasing the probability of interparticle interactions and packing the particles together [72].

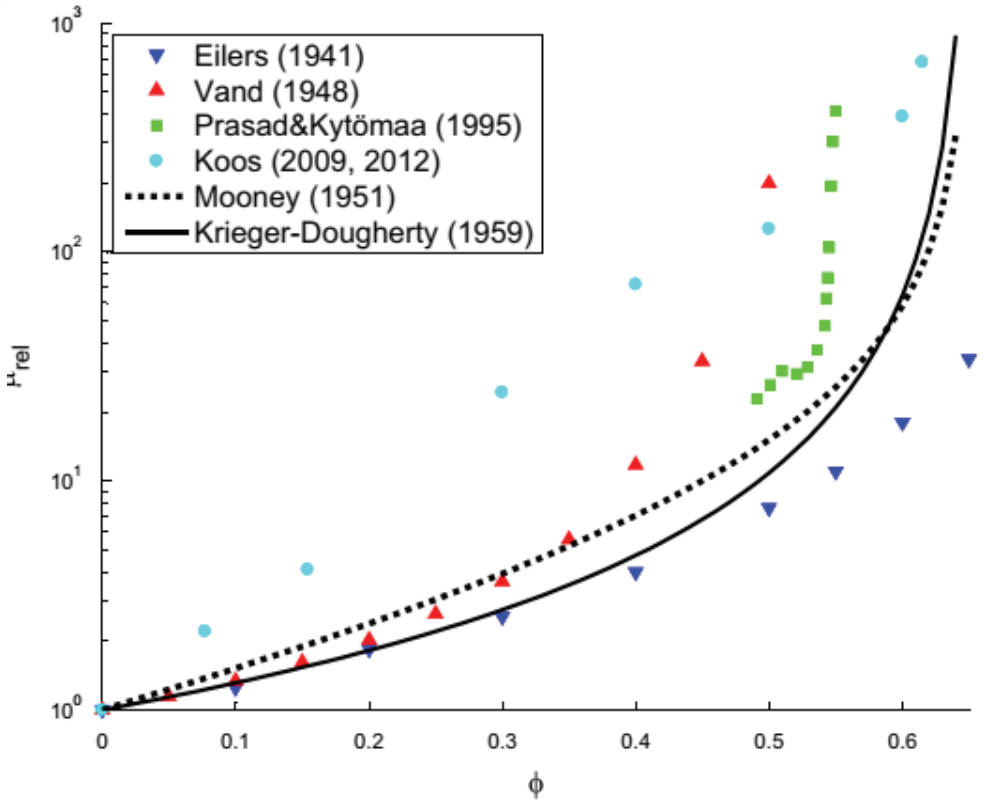

Figure 8.1. The relationship between solid fraction, ϕ and relative viscosity, μ_{rel} (Source: Konijn et al., 2014)

CMC addition stabilizes the slurries sterically and it also increases the viscosity of the system since as the CMC amount increases, the amount of the carboxymethyl

groups binding hydroxyl group increase. The binding energy of the powder increases the packing of the particles; hence viscosity increases.

8.3. Expansion of Foams

Thermodynamically, aqueous foams are unstable as foams collapse with time. Foam decay occurs mostly by drainage and coarsening (Figure 8.2). Drainage is the downward flow of the liquid metal through the cell edges due to gravitational forces. Coarsening is caused by the bubble-bubble gas transport which is resulted from the pressure difference. The gas in bubbles transport from smaller to larger bubble due to the concentration gradient from the pressure difference in bubbles. Disproportionation rate depends mainly on the partial pressure differences of the gases present. However, when the gas composition is uniform inside the bubble, the rheological behavior of the bubble surface becomes the main parameter affecting the disproportionation rate [84]. The duration of the decrease in bubble radius is greater in foams having lower viscosity since the surface tension and the dissolution rate of the gas decreases. Rheology of foams affects the drainage and coarsening of the foaming structure. Coarsening is accelerated with the increase of solid content or CMC content since the shear modulus increases [85].

The slurries that kept their expanded structure at longer times are classified as stable and the slurries that collapse after the maximum expansion as unstable in this study. As shown in Figures 7.16, 7.17 and 7.18, the unstable foams are only seen in the slurries with 60 wt% solid content, although they have the highest maximum expansion. The increase of CMC also tends to form unstable foams.

The expansion rate of slurries was found to be highly dependent on the viscosity change (Figure 7.20). As the flow of the slurry gets more difficult at high viscosity, the slurry expansion becomes difficult and pressure difference between the bubbles and the slurry matrix increases. This causes a local change in the gas-liquid ratio of the slurry after the foaming reaction starts and the gas diffusion from slurry matrix to the bubbles increases the internal pressure inside the bubbles [86]. Thus, a sudden explosion-type expansion in particularly slurries having 60 wt% solid content. This causes an increase in expansion rate. However, this also accelerates the foam decay and when the surface tension becomes more pronounced where the maximum expansion is reached. Therefore, in the slurries with high viscosity, the rate of the foam coarsening increases. This was also

observed previously [58, 84, 87]. This effect is also seen in the image analysis of bubble formation in Figures 7.21(a-c). Bubble diameter increases with the solid content increase due to the internal pressure increase with viscosity.

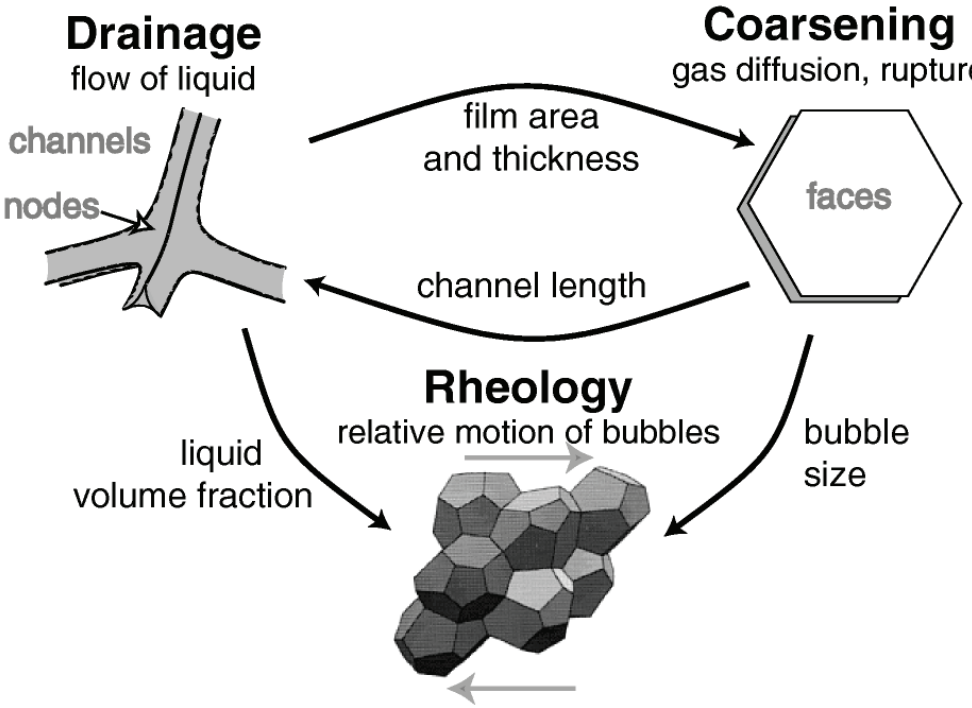

Figure 8.2. The interdependence of drainage, coarsening and rheology
(Source: Hilgenfeldt, et al., 2001)

The variations of number of cells in a selected area of slurries having different solid contents with 4 wt% CMC addition with medium powder is shown in Figure 8.3 The number of cells in 55 and 60 wt% solid content slurries are higher than in 50 wt% solid content slurries at 500 s corresponding to maximum expansion. This is because of the higher expansion rate in these foams. However, the number of cells in 55 and 60 wt% solid content slurries decreases below that in 50 wt% solid content slurries at 1500 s corresponding to the foaming duration after maximum expansion. This proved the increased foam decay in 55 and 60 wt% solid content slurries after foam expansion.

The average cell size increases during foaming in slurries having 50 wt% solid content since the cell wall rupture occurs easily in slurries having lower viscosity. The number of cells of these slurries decreases dramatically after about 720 seconds. After 1500 seconds, the number of cells is increasing due to the explosion of the bubbles and formation of smaller new bubbles since the gravitational forces prevents the expansion of

the slurry while new bubbles occurring. The increase in the cell number of slurries having higher viscosities might be explained by the shrinkage of the slurry. Glass particle shape might affect the shrinkage of the slurries after foaming. Sharp edges of the glass particles might explode the bubbles when they reach to a point they interfere with these sharp edges.

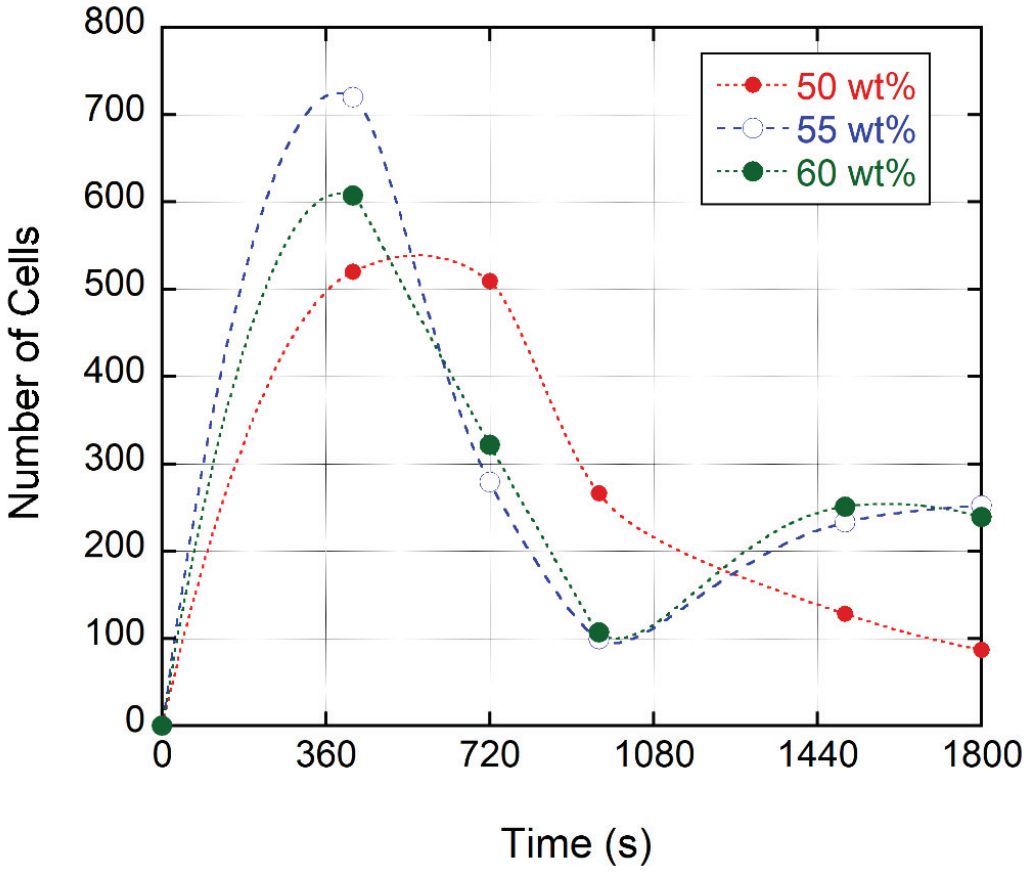

Figure 8.3. The variations of number of cells in slurries having different solid contents with time

Slurries with fine particles with 4 wt% CMC addition in 60 wt% solid content cannot be foamed as being very thick. The thickness of this kind of slurries comes from the much larger surface to volume ratio compared to large particles. Fine particles tend to agglomerate, and their flow behavior is affected by this phenomenon. Thus, in the large surface area of fine particles, the ratio of surface free energy to bulk energy is high. Therefore, below a critical diameter, surface drift diffusion allows matter transfer between the particles in a medium, such as the aqueous environment of this study and this prevents the material flow in the foaming medium.

8.4. The Foaming Reaction

The reaction kinetics and the hydrogen release mechanism shown in Figure 8.4 affects the foaming properties of the glass powder slurries. The corrosion rate of aluminum with hydrated lime depends on temperature, particle size of the aluminum and calcium hydroxide powder, aluminum and calcium hydroxide concentrations in the solution and the pH of the reaction environment. In this study, all the parameters except the pH of the environment are constant. The pH of the environment varies with the varying the CMC and solid content. Therefore, the productivity of hydrogen release, which increases the foam expansion, is augmented by the increase of the solid content and CMC. In order to understand the reaction kinetics in detail, the parameters mentioned above might be considered in the future.

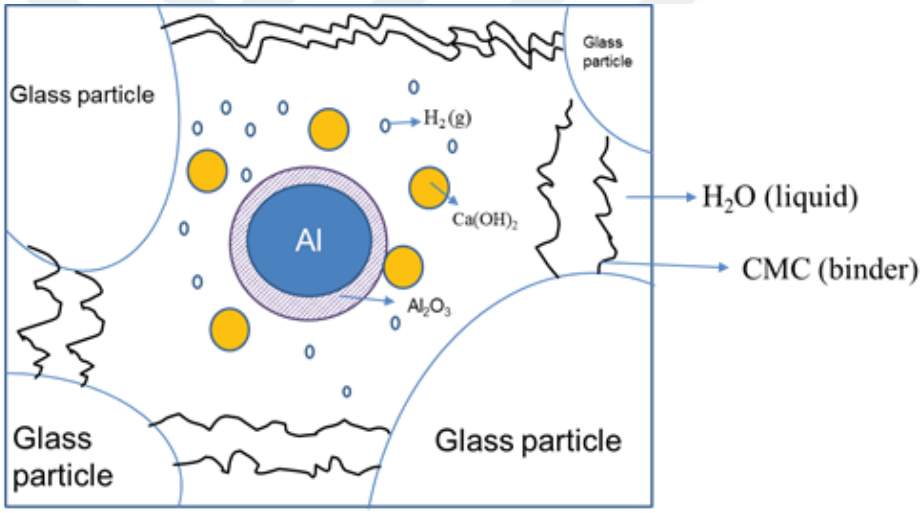

Figure 8.4. Schematic representation of the foaming system

8.5. 3^3 Full Factorial Design Results

Total 27 types of experiments were analyzed, and the parameters impacted the results were determined with 3-level factorial design in ANOVA. According to ANOVA, the most effective factor on the maximum expansion is the solid content, the second effective factor is CMC content and the least effective factor is the particle size. The variation in solid content is the most effective factor in the viscosity of the slurries according to the experimental results shown in Figure 8.5. Solid content dominates the

results mostly. The particle size had insignificant effect on the response of the maximum expansion since the size intervals might be chosen as close to each other.

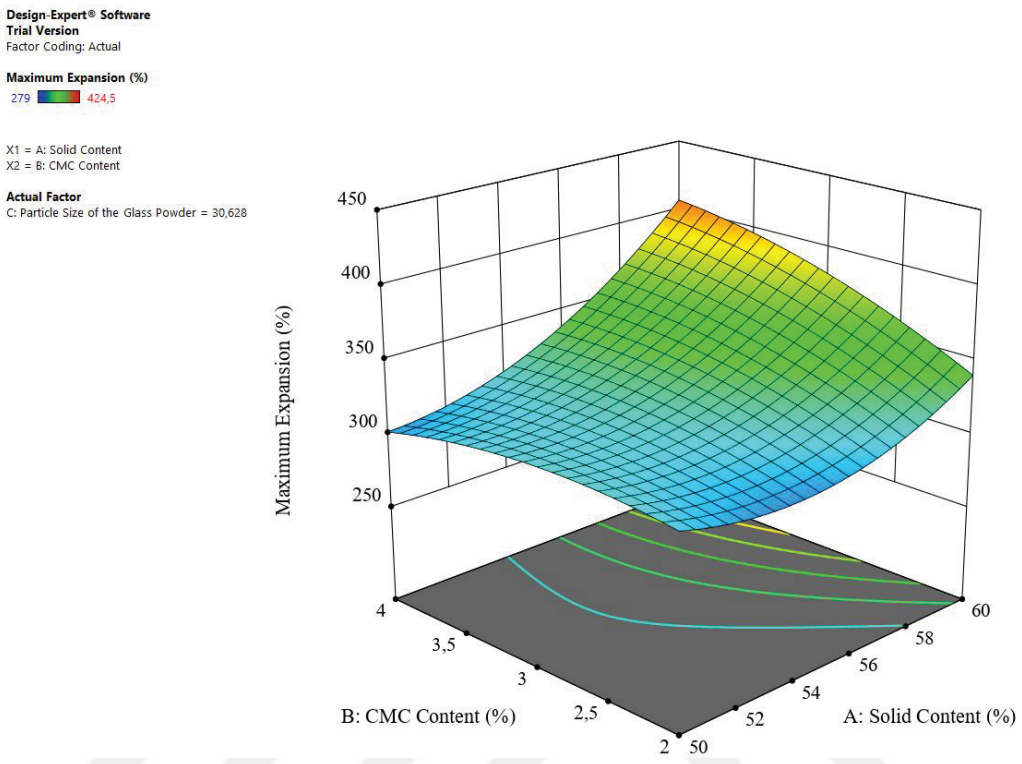

Figure 8.5. The response surface 3D plot of CMC content-maximum expansion and solid content-maximum expansion

8.6. Microstructural Analysis and Mechanical and Thermal Properties

The colloidal stability of the slurry was provided by the addition of the CMC with steric stabilization. Decaying process of the foam was prohibited by preventing the flocculation and van der Waals attractions between the adsorbed particles [68]. Therefore, the green body structure was obtained effectively as shown in Figure 7.26. The sintering increased the cell wall density and reduced the extent of cell wall pores (Figures 7.31 and 7.32). Increasing sintering temperature caused shrinkage of the body and decreased the pore size [88].

The compressive strength of glass foam samples tested previously are shown as function of density in Figure 8.6, together with those of present study. The collapse stress *vs.* density shown in Figure 8.6 (references in Fig. 13: 1-[48], 2-[48], 3-[24], 4-[89], 5 -[50], 6-[90],7-[91],8-[34], 9-[52],10- [53], 11-[54] and 12- [45]) were fitted with Equation 3.1. The collapse stresses

of the investigated and reported foam glasses are well fitted with the ϕ values between 0.7 and 1 for the foam densities up to 300 kg m^{-3} and the ϕ values between 0.7 and 0.9 for the foam densities above 300 kg m^{-3}. The tested present glass foam showed lower compressive strength than those of previous studies. The compressive strength however shows a well match with those of open cell foams. The lower strength of present foams simply arises from the porosities on the cell edge and walls and partly from introduced anisotropy during drying and sintering. The cells are elongated to the transverse to the foaming direction, which induced a lower strength in this direction.

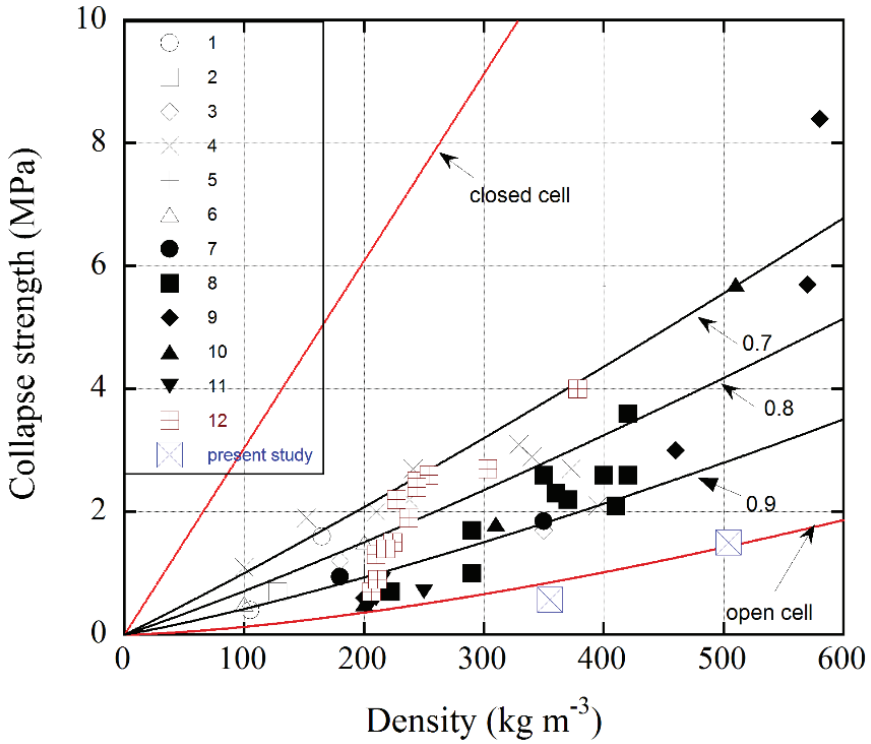

Figure 8.6. The collapse strength of glass foams and the present study

Thermal conductivities of the glass foam samples reported previously as function of density are shown in Figure 8.7 together with the thermal conductivities of glass foams of present study (reference: 1-[38], 2-[50] 3-[48], 4-[48], 5-[31],7-[92]and 8-[93]). Thermal conductivities of tested foam glass range between 0.042 to 0.057. The tested foam glass, as shown in Figure 8.7, exhibit lower thermal conductivities than those of foam glasses reported in the literature. The uniform pore distribution and open cell structure of the glass foams in the present study might be occasioned for lower thermal conductivities. In addition to

this, lower pore sizes, nanosized crystalline tobermorite structure, also residual hydration products increase the insulation properties of the product [1, 5, 9].

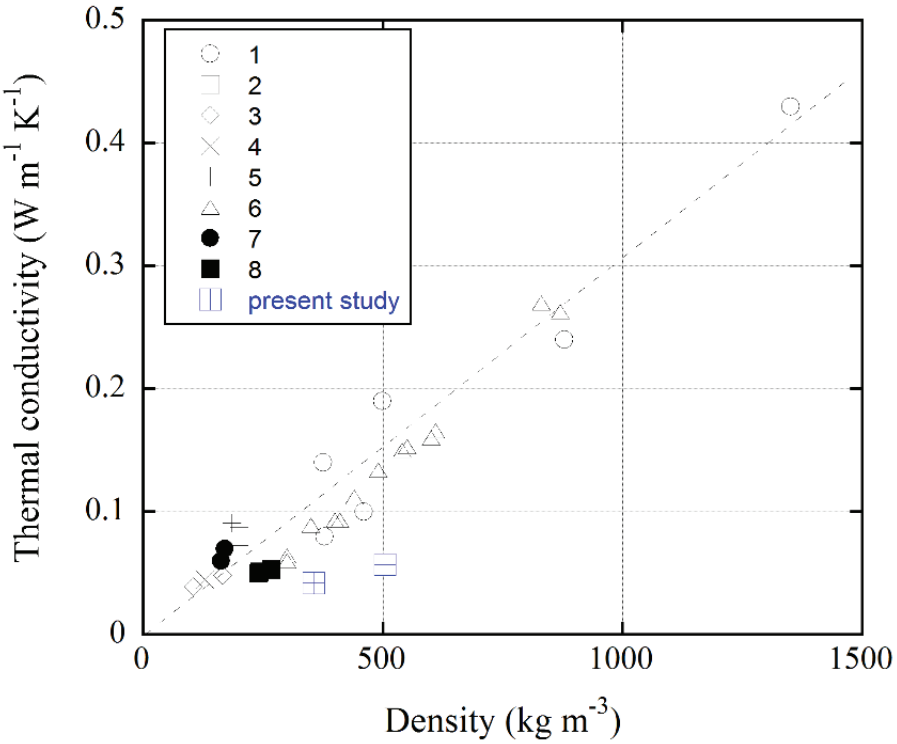

Figure 8.7. The thermal conductivity of foam glasses and present study

CHAPTER 9

CONCLUSIONS

Processing foam glass structures from aqueous solutions using a foaming agent of Al (1 wt%) and an alkali activator of $Ca(OH)_2$ (1 wt%) was experimentally investigated at room temperature. The rheological behavior and the effect of solid content (50, 55 and 60 wt%), CMC amount (0-4wt%) and glass-powder size distribution (fine, medium and coarse) on the foaming behavior of the prepared slurries were determined. The linear expansion of the slurries was measured using a laser distance measuring device standing above the foaming mold. The bubble size distribution of the slurries during foaming was also investigated from the video records of the foaming process. Followings were concluded.

The slurries with 50 and 55 wt% showed a Newtonian, while the slurries with 60 wt% solid content showed a non-Newtonian shear thinning behavior. In fine powder slurries with 60 wt% solid content and 4wt% CMC addition, no measurement could be taken due to the relatively high viscosity of the slurry. Results showed that an increase in CMC content and a decrease in particle size caused a shift from Newtonian to non-Newtonian behavior in the slurries. Furthermore, the slurries were determined to be stabilized with CMC addition.

Two types of linear expansion behavior were observed dependent on the solid content of the slurries. After the initial maximum expansion, the linear expansion stayed almost constant with time in low viscosity slurries and the linear expansion decreased with time in high viscosity slurries. The foam initial linear expansion rate until maximum expansion was also higher in high viscosity slurries. The extensively increased initial bubble pressure in high viscosity slurries resulted in explosion-type expansion initially leading to high expansion rates initially followed by a bursting of gas bubbles.

The bubble size and distribution were observed to be saturated after 12 min (~1250 s) in 50, 55 ad 60 wt% solid content slurries. A higher size of bubbles was found in 50 wt% slurries, while the size of bubbles in 55 and 60 wt% solid content slurries were comparatively smaller. The coarsening was accelerated in low viscosity slurries.

The ANOVA with a 3-level factorial analysis showed the most effective factor on the maximum expansion was the solid content followed by CMC content and the least effective factor was determined the particle size. Similar results were also found on the viscosity of the slurries.

The SEM images of the polished surface of a foam glass green bodies proved an efficient interaction between carboxyl groups of the carboxymethyl cellulose and the surfaces of glass particles.

The foam green bodies showed no binding at a sintering temperature of 650 ^{o}C, while sintering at 800 ^{o}C resulted in excessive shrinkage due to the melting of glass particles. The foam samples with 55 wt% and 60wt% solid content sintered at 700 and 750 ^{o}C for ½ hr showed average densities between 355-530 kg m^{-3} and average compressive stresses between 0.15 and 0.58 MPa. Increasing the sintering time from ½ to 1 hr at 750 ^{o}C increased the average compressive strength from 0.58 to 1.3 MPa for 60 wt% solid content foam. These proved that the sintering temperature and time were effective in increasing the compressive strength of foamed slurries. The thermal conductivity of sintered foam samples with 355 kg m^{-3} density was 0.042 w m^{-1} K^{-1}, while it increased to 0.057 w m^{-1} K^{-1} when the density increases to 504 kg m^{-3}. The tested foam glasses exhibited lower compressive strength and thermal conductivities than foam glasses reported in the literature.

9.1. Recommendations for Future Studies

1) Particle size effect on foaming was found to be least effective parameter, while the effect of wider particle size range should be investigated on the foaming behavior of such slurries.
2) The foaming and alkali activator content in present study kept constant, 1 wt%. The effect of the contents of the foaming agent and alkali activator on the foaming behavior should be investigated as future study.
3) The possible reactions between silica, foaming agent and alkali activator after foaming and after sintering should be investigated further.
4) The fine tuning of the compressive strength and thermal conductivity of the prepared foams should be performed by optimization of the sintering temperature and time.

5) Although, this study used soda-lime silica glass as the main ingredient, other materials such as metals or ceramic powders are good candidates where this method is useful.

REFERENCES

1. Hamad, A. J., Materials, Production, Properties and Application of Aerated Lightweight Concrete: A Review. *International Journal of Materials Science and Engineering* 2014, *2* (2), 152-157.

2. Scheffler, M.; Colombo, P., *Cellular Ceramics: Structure, Manufacturing, Properties and Applications*. Wiley: 2005.

3. Narloch, D. C.; Paschuk, S. A.; Corrêa, J. N.; Rocha, Z.; Mazer, W.; Torres, C. A. M. P.; Del Claro, F.; Denyak, V.; Schelin, H. R., Characterization of radionuclides present in portland cement, gypsum and phosphogypsum mortars. *Radiation Physics and Chemistry* 2018.

4. Narayanan, N.; Ramamurthy, K., Structure and properties of aerated concrete: a review. *Cement and Concrete Composites* 2000, *22* (5), 321-329.

5. Mathey, R. G. R., Walter J., Jr. *A review of autoclaved aerated concrete products*; nbsir87-3670; National Bureau of Standards, 1988.

6. Nambiar, E. K. K.; Ramamurthy, K., Shrinkage Behavior of Foam Concrete. *Journal of Materials in Civil Engineering* 2009, *21* (11), 631-636.

7. Kanehira, S.; Kanamori, S.; Nagashima, K.; Saeki, T.; Visbal, H.; Fukui, T.; Hirao, K., Controllable hydrogen release via aluminum powder corrosion in calcium hydroxide solutions. *Journal of Asian Ceramic Societies* 2013, *1* (3), 296-303.

8. An, Z.; Zhang, Y.; Li, Q.; Wang, H.; Guo, Z.; Zhu, J., Effect of particle shape on the apparent viscosity of liquid–solid suspensions. *Powder Technology* 2018, *328*, 199-206.

9. Wan, H.; Hu, Y.; Liu, G.; Qu, Y., Study on the structure and properties of autoclaved aerated concrete produced with the stone-sawing mud. *Construction and Building Materials* 2018, *184*, 20-26.

10. Gibson, L. J.; Ashby, M. F., *Cellular Solids: Structure and Properties*. 2 ed.; Cambridge University Press: Cambridge, 1997.

11. Ergul, S.; Ferrante, F.; Pisciella, P.; Karamanov, A.; Pelino, M., Characterization of basaltic tuffs and their applications for the production of ceramic and glass-ceramic materials. *Ceramics International* 2009, *35* (7), 2789-2795.

12. Pehlivanlı, Z. O.; Uzun, İ.; Demir, İ., Mechanical and microstructural features of autoclaved aerated concrete reinforced with autoclaved polypropylene, carbon, basalt and glass fiber. *Construction and Building Materials* 2015, *96*, 428-433.

13. Rasheed, M. A.; Prakash, S. S., Behavior of hybrid-synthetic fiber reinforced cellular lightweight concrete under uniaxial tension – Experimental and analytical studies. *Construction and Building Materials* 2018, *162*, 857-870.

14. Bonakdar, A.; Babbitt, F.; Mobasher, B., Physical and mechanical characterization of Fiber-Reinforced Aerated Concrete (FRAC). *Cement and Concrete Composites* 2013, *38*, 82-91.

15. Tasdemir, C.; Sengul, O.; Tasdemir, M. A., A comparative study on the thermal conductivities and mechanical properties of lightweight concretes. *Energy and Buildings* 2017, *151*, 469-475.

16. Long, B. Glass product and method of manufacturing sponge-like glass. 1934.

17. Games, S. Method of making a vitreous material. 1932, 1932.

18. Jones, G. D.; McMillan, W. J.; Williams, C. N., Foamed Glass And Vitreous Silica Pellets. *Industrial & Engineering Chemistry Product Research and Development* 1979, *18* (1), 64-69.

19. Long, B. Process for the manufacture of multicellular glass. 1938.

20. Ivanov, S. É.; Belyakov, A. V., Diatomite and its applications. *Glass and Ceramics* 2008, *65* (1), 48-51.

21. Hamid Hojaji, D. M. P. M. B., Theodore Aaron Litovitz Method and composition for making foam glass from diatomaceous earth and fly ash. EP0091473A4, 1981.

22. Ford, W. D. Nodulated cellular glass and method of forming. 1954.

23. Lu, J.; Onitsuka, K., Construction utilization of foamed waste glass. *Journal of Environmental Sciences-China* 2004, *16* (2), 302-307.

24. Wu, J. P.; Boccaccini, A. R.; Lee, P. D.; Kershaw, M. J.; Rawlings, R. D., Glass ceramic foams from coal ash and waste glass: production and characterisation. *Advances in Applied Ceramics* 2006, *105* (1), 32-39.

25. Eidukyavichus, K. K.; Matseikene, V. R.; Balkyavichus, V. V.; Shpokauskas, A. A.; Laukaitis, A. A.; Kunskaite, L. Y., Use of cullet of different chemical compositions in foam glass production. *Glass and Ceramics* 2004, *61* (3-4), 77-80.

26. Chen, B.; Luo, Z.; Lu, A., Preparation of sintered foam glass with high fly ash content. *Materials Letters* 2011, *65* (23), 3555-3558.

27. Chakartnarodom, P.; Ineure, P., Foam Glass Development Using Glass Cullet and Fly Ash or Rice Husk Ash as the Raw Materials. *Key Engineering Materials* 2014, *608*, 73-78.

28. Fernandes, H. R.; Tulyaganov, D. U.; Ferreira, J. M. F., Preparation and characterization of foams from sheet glass and fly ash using carbonates as foaming agents. *Ceramics International* 2009, *35* (1), 229-235.

29. Petersen, R. R.; König, J.; Smedskjaer, M. M.; Yue, Y., Foaming of CRT panel glass powder using Na2CO3. *Glass Technology - European Journal of Glass Science and Technology Part A* 2014, *55* (1), 1-6.

30. Bernardo, E.; Albertini, F., Glass foams from dismantled cathode ray tubes. *Ceramics International* 2006, *32* (6), 603-608.

31. Bobkova, N. M.; Barantseva, S. E.; Trusova, E. E., Production of foam glass with granite siftings from the Mikashevichi deposit. *Glass and Ceramics* 2007, *64* (1), 47-50.

32. Spiridonov, Y. A.; Orlova, L. A., Problems of Foam Glass Production. *Glass and Ceramics* 2003, *60* (9-10), 313-314.

33. Bernardo, E.; Cedro, R.; Florean, M.; Hreglich, S., Reutilization and stabilization of wastes by the production of glass foams. *Ceramics International* 2007, *33* (6), 963-968.

34. Bernardo, E.; Scarinci, G.; Bertuzzi, P.; Ercole, P.; Ramon, L., Recycling of waste glasses into partially crystallized glass foams. *Journal of Porous Materials* 2010, *17* (3), 359-365.

35. Bernardo, E.; Scarinci, G.; Hreglich, S., Foam glass as a way of recycling glasses from cathode ray tubes. *Glass Science and Technology* 2005, *78* (1), 7-11.

36. Mear, F.; Yot, P.; Cambon, M.; Ribes, A. M., Elaboration and characterisation of foam glass from cathode ray tubes. *Advances in Applied Ceramics* 2005, *104* (3), 123-130.

37. Mear, F.; Yot, P.; Ribes, M., Effects of temperature, reaction time and reducing agent content on the synthesis of macroporous foam glasses from waste funnel glasses. *Materials Letters* 2006, *60* (7), 929-934.

38. Mear, F.; Yot, P.; Viennois, R.; Ribes, M., Mechanical behaviour and thermal and electrical properties of foam glass. *Ceramics International* 2007, *33* (4), 543-550.

39. Guo, H. W.; Gong, Y. X.; Gao, S. Y., Preparation of high strength foam glass–ceramics from waste cathode ray tube. *Materials Letters* 2010, *64* (8), 997-999.

40. Matamoros-Veloza, Z.; Rendon-Angeles, J. C.; Yanagisawa, K.; Cisneros-Guerrero, M. A.; Cisneros-Guerrero, M. M.; Aguirre, L., Preparation of foamed glasses from CRT TV glass by means of hydrothermal hot-pressing technique. *Journal of the European Ceramic Society* 2008, *28* (4), 739-745.

41. Chen, M. J.; Zhang, F. S.; Zhu, J. X., Lead recovery and the feasibility of foam glass production from funnel glass of dismantled cathode ray tube through pyrovacuum process. *Journal of Hazardous Materials* 2009, *161* (2-3), 1109-1113.

42. Gerhard, B., Foaming of borosilicate glasses by chemical reactions in the temperature range 950-1150 °C. *Journal of Non-Crystalline Solids* 1980, *38-39, Part 2* (0), 855-860.

43. Goyal, S. K.; Cutler, I. B., Absorption of water in waste glass as a precursor for foam formation. *Journal of Non-Crystalline Solids* 1975, *19* (DEC), 311-320.

44. Manevich, V. E.; Subbotin, K. Y., Mechanism of foam-glass formation. *Glass and Ceramics* 2008, *65* (5-6), 154-156.

45. Attila, Y.; Guden, M.; Tasdemirci, A., Foam glass processing using a polishing glass powder residue. *Ceramics International* 2013, *39* (5), 5869-5877.

46. König, J.; Petersen, R. R.; Yue, Y., Influence of the glass particle size on the foaming process and physical characteristics of foam glasses. *Journal of Non-Crystalline Solids* 2016, *447*, 190-197.

47. Guden, M.; Yüksel, S., SiC-particulate aluminum composite foams produced from powder compacts: foaming and compression behavior. *Journal of Materials Science* 2006, *41* (13), 4075-4084.

48. Wrap (2019, May 5). Retrieved from https:// www.wrap.org.uk.

49. Shutov, A. I.; Yashurkaeva, L. I.; Alekseev, S. V.; Yashurkaev, T. V., Study of the structure of foam glass with different characteristics. *Glass and Ceramics* 2007, *64* (9-10), 297-299.

50. Kaz'mina, O. V.; Vereshchagin, V. I.; Abiyaka, A. N., Prospects for use of finely disperse quartz sands in productıon of foam-glass crystalline materıals. *Glass and Ceramics* 2008, *65* (9-10), 319-321.

51. Kaz'mina, O. V.; Vereshchagin, V. I.; Semukhin, B. S.; Abiyaka, a. N., Low-temperature synthesis of granular glass from mixes based on silica-alumina-containing components for obtaining foam materials. *Glass and Ceramics* 2009, *66* (9-10), 341-344.

52. Garcia-Ten, J.; Saburit, A.; Orts, M. J.; Bernardo, E.; Colombo, P., Glass foams from oxidation/reduction reactions using SiC, Si3N4 and AlN powders. *Glass Technology-European Journal of Glass Science and Technology Part A* 2011, *52* (4), 103-110.

53. Llaudis, A. S.; Tari, M. J. O.; Ten, F. J. G.; Bernardo, E.; Colombo, P., Foaming of flat glass cullet using Si3N4 and MnO2 powders. *Ceramics International* 2009, *35* (5), 1953-1959.

54. Garkavi, M. S.; Mel'chaeva, O. K.; Nazarova, A. I., Effect of the process parameters of mix preparation on the properties of foam glass. *Glass and Ceramics* 2011, *68* (1-2), 44-46.

55. Morgan, J. S.; Wood, J. L.; Bradt, R. C., Cell-size effects on the strength of foamed glass. *Materials Science and Engineering* 1981, *47* (1), 37-42.

56. Østergaard, M. B.; Petersen, R. R.; König, J.; Johra, H.; Yue, Y., Influence of foaming agents on solid thermal conductivity of foam glasses prepared from CRT panel glass. *Journal of Non-Crystalline Solids* 2017, *465*, 59-64.

57. Weaire, D.; Phelan, R., The physics of foam. *Journal of Physics: Condensed Matter* 1996, *8* (47), 9519.

58. Koerner, C., Physics of Foaming. In *Integral Foam Molding of Light Metals*, Springer Berlin Heidelberg: 2008; pp 77-102.

59. Daoud, A., Effect of fly ash addition on the structure and compressive properties of 4032–fly ash particle composite foams. *Journal of Alloys and Compounds* 2009, *487* (1), 618-625.

60. Koerner, C., *Integral Foam Molding of Light Metals: Technology, Foam Physics and Foam Simulation*. Springer Berlin Heidelberg: 2008.

61. Binks, B. P.; Horozov, T. S., Aqueous Foams Stabilized Solely by Silica Nanoparticles. *Angewandte Chemie International Edition* 2005, *44* (24), 3722-3725.

62. Fameau, A.-L.; Salonen, A., Effect of particles and aggregated structures on the foam stability and aging. *Comptes Rendus Physique* 2014, *15* (8–9), 748-760.

63. Banhart, J., Metal Foams: Production and Stability. *Advanced Engineering Materials* 2006, *8* (9), 781-794.

64. Kumagai, H.; Torikata, Y.; Yoshimura, H.; Kato, M.; Yano, T., Estimation of the Stability of Foam Containing Hydrophobic Particles by Parameters in the Capillary Model. *Agricultural and Biological Chemistry* 1991, *55* (7), 1823-1829.

65. Bhakta, A.; Ruckenstein, E., Decay of standing foams: drainage, coalescence and collapse. *Advances in Colloid and Interface Science* 1997, *70* (0), 1-124.

66. Jin, I.; Kenny, L. D.; Sang, H., Stabilized metal foam body. Google Patents: 1992.

67. Yang, L., 1 - Fundamentals of nanotechnology and orthopedic materials. In *Nanotechnology-Enhanced Orthopedic Materials*, Yang, L., Ed. Woodhead Publishing: Oxford, 2015; pp 1-25.

68. Lewis, J. A., Colloidal Processing of Ceramics. *Journal of the American Ceramic Society* 2000, *83* (10), 2341-2359.

69. Park, S. J.; Seo, M. K., *Interface Science and Composites*. Elsevier Science: 2011.

70. Duvarcı Çağlar, Ö.; Çiftçioğlu, M., *Rheological behavior of nanocrystalline/ submicron ceramic powder dispersion*. 2009.

71. Rheology of Disperse Systems. In *Product Design and Engineering*.

72. Bergstrom, L., *Surface and Colloid Chemistry in Advanced Ceramics Processing*. CRC Press: 2017.

73. Huang, Y.; Yang, J., *Novel Colloidal Forming of Ceramics*. Springer Berlin Heidelberg: 2011.

74. Wolfgang M Sigmund, N. S. B., Lennart Bergström, Novel powder-processing methods for advanced ceramics. *Journal of the American Ceramic Society* 2000, *83* (7), 1557-1574.

75. C-Therm, (2019, May 5). Retrieved from https://www.chtherm.com.

76. Rehman, Z. U.; Suk, H.; Janulewicz, K. A., Optical breakdown-driven mesostructure in bulk of soda-lime glass. *Journal of Non-Crystalline Solids* 2016, *448*, 68-73.

77. Laurent, O.; Mantisi, B.; Micoulaut, M., Structure and Topology of Soda-Lime Silicate Glasses: Implications for Window Glass. *The Journal of Physical Chemistry B* 2014, *118* (44), 12750-12762.

78. Konijn, B. J.; Sanderink, O. B. J.; Kruyt, N. P., Experimental study of the viscosity of suspensions: Effect of solid fraction, particle size and suspending liquid. *Powder Technology* 2014, *266*, 61-69.

79. Mueller, S.; Llewellin, E. W.; Mader, H. M., The rheology of suspensions of solid particles. *Proceedings of the Royal Society A: Mathematical, Physical and Engineering Sciences* 2010, *466* (2116), 1201-1228.

80. Eilers, H., Die Viskosität von Emulsionen hochviskoser Stoffe als Funktion der Konzentration. *Kolloid-Zeitschrift* 1941, *97* (3), 313-321.

81. Vand, V., Viscosity of Solutions and Suspensions. II. Experimental Determination of the Viscosity–Concentration Function of Spherical Suspensions. *The Journal of Physical and Colloid Chemistry* 1948, *52* (2), 300-314.

82. Prasad, D.; Kytömaa, H. K., Particle stress and viscous compaction during shear of dense suspensions. *International Journal of Multiphase Flow* 1995, *21* (5), 775-785.

83. Koos, E.; Linares-Guerrero, E.; Hunt, M. L.; Brennen, C. E., Rheological measurements of large particles in high shear rate flows. *Physics of Fluids* 2012, *24* (1), 013302.

84. Ronteltap, A. D.; Damsté, B. R.; De Gee, M.; Prins, A., The role of surface viscosity in gas diffusion in aqueous foams. I. Theoretical. *Colloids and Surfaces* 1990, *47*, 269-283.

85. Hilgenfeldt, S.; Koehler, S. A.; Stone, H. A., Dynamics of Coarsening Foams: Accelerated and Self-Limiting Drainage. *Physical Review Letters* 2001, *86* (20), 4704-4707.

86. Kroezen, A. B. J.; Wassink, J. G.; Schipper, C. A. C., The flow properties of foam. 1988, *104* (10), 393-400.

87. Sepulveda, P.; Binner, J. G. P., Processing of cellular ceramics by foaming and in situ polymerisation of organic monomers. *Journal of the European Ceramic Society* 1999, *19* (12), 2059-2066.

88. Ohji, T.; Singh, M.; Singh, D.; Salem, J., *Advanced Processing and Manufacturing Technologies for Structural and Multifunctional Materials III*. Wiley: 2009.

89. Shutov, A. I.; Yashurkaeva, L. I.; Alekseev, S. V.; Yashurkaev, T. V., Modeling of the structure of heat-insulating foam glass. *Glass and Ceramics* 2007, *64* (11-12), 397-399.

90. Kaz'mina, O. V.; Vereshchagin, V. I.; Abiyaka, A. N., Assessment of the compositions and components for obtaining foam-glass-crystalline materials from aluminosilicate initial materials. *Glass and Ceramics* 2009, *66* (3-4), 82-85.

91. Fernandes, H. R.; Tulyaganov, D. U.; Ferreira, J. M. F., Production and characterisation of glass ceramic foams from recycled raw materials. *Advances in Applied Ceramics* 2009, *108* (1), 9-13.

92. Xi, C.; Zheng, F.; Xu, J.; Yang, W.; Peng, Y.; Li, Y.; Li, P.; Zhen, Q.; Bashir, S.; Liu, J. L., Preparation of glass-ceramic foams using extracted titanium tailing and glass waste as raw materials. *Construction and Building Materials* 2018, *190*, 896-909.

93. Konig, J.; Petersen, R. R.; Iversen, N.; Yue, Y. Z., Suppressing the effect of cullet composition on the formation and properties of foamed glass. *Ceramics International* 2018, *44* (10), 11143-11150.

APPENDIX A

SUPPLEMENTARY MATERIAL

A.1. Viscosity Experiments

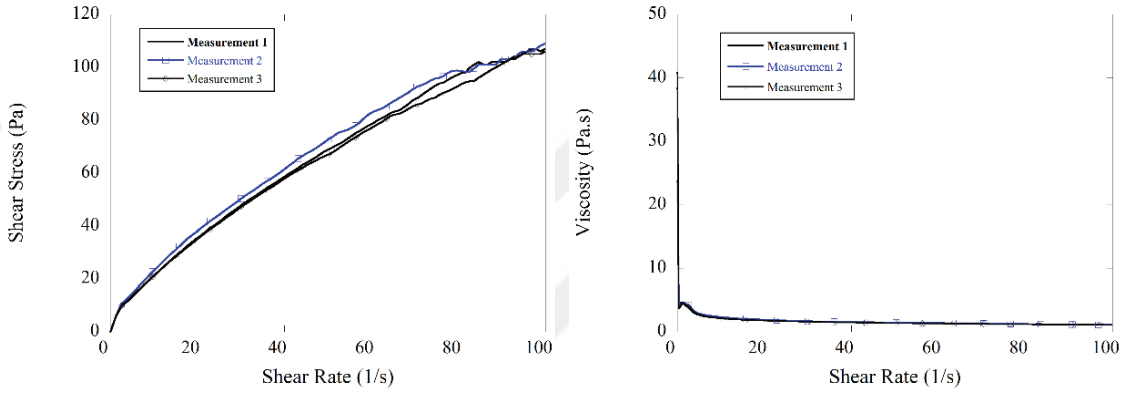

Figure A.1. Three measurements of shear stress-shear rate and viscosity-shear rate curves of the slurry with fine powders in 60 wt% solids content with 2 wt% CMC

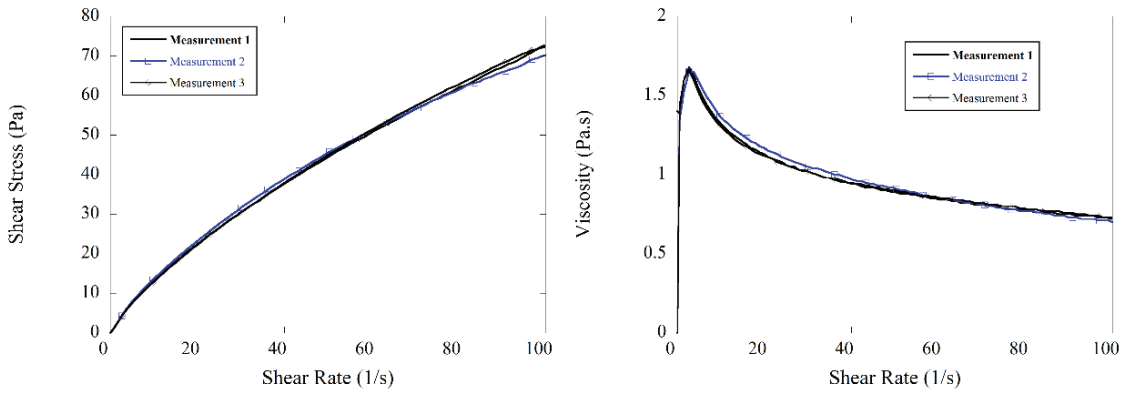

Figure A.2. Three measurements of shear stress-shear rate and viscosity-shear rate curves of the slurry with coarse powders in 50 wt% solids content with 2 wt% CMC

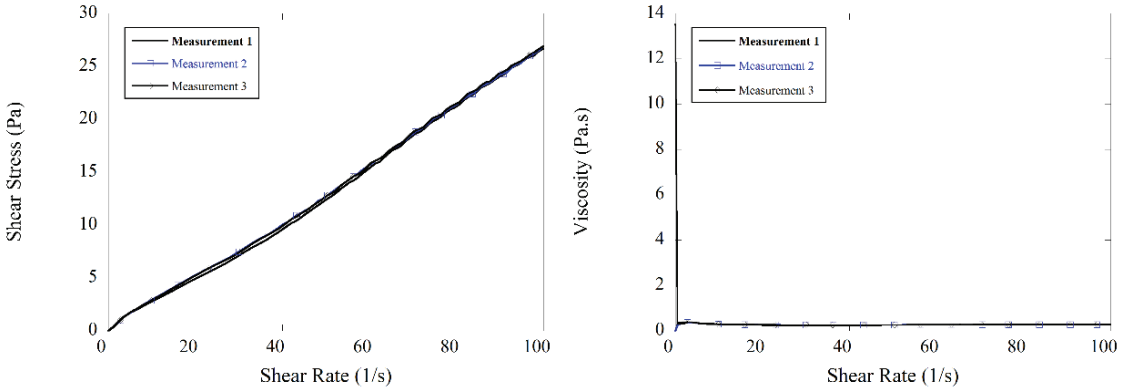

Figure A.3. Three measurements of shear stress-shear rate and viscosity-shear rate curves of the slurry with coarse powders in 60 wt% solids content with 2 wt% CMC

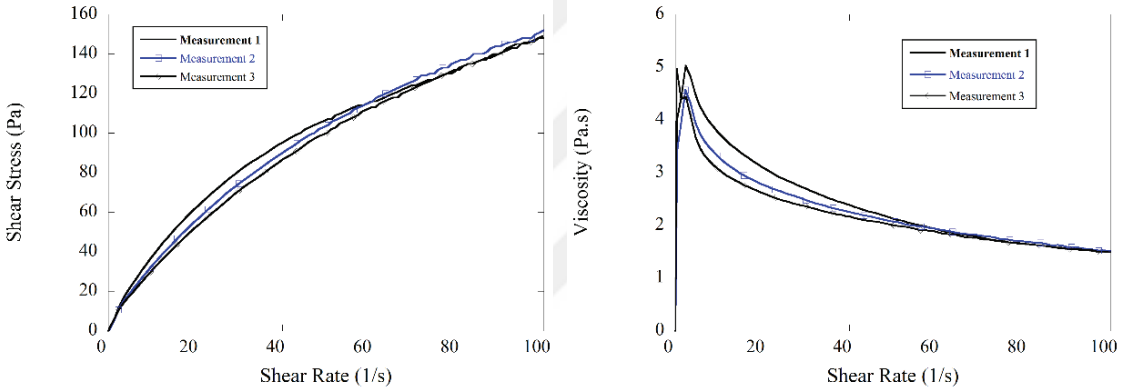

Figure A.4. Three measurements of shear stress-shear rate and viscosity-shear rate curves of the slurry with fine powders in 50 wt% solids content with 3 wt% CMC

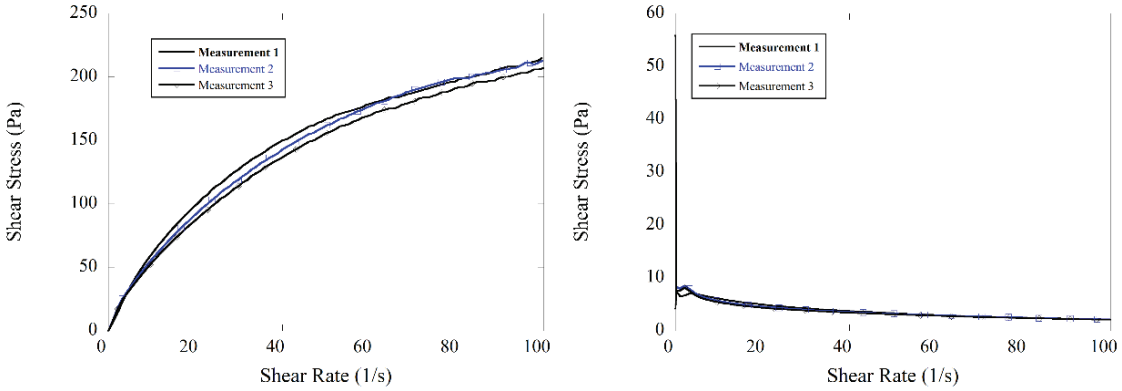

Figure A.5. Three measurements of shear stress-shear rate and viscosity-shear rate curves of the slurry with fine powders in 60 wt% solids content with 3 wt% CMC

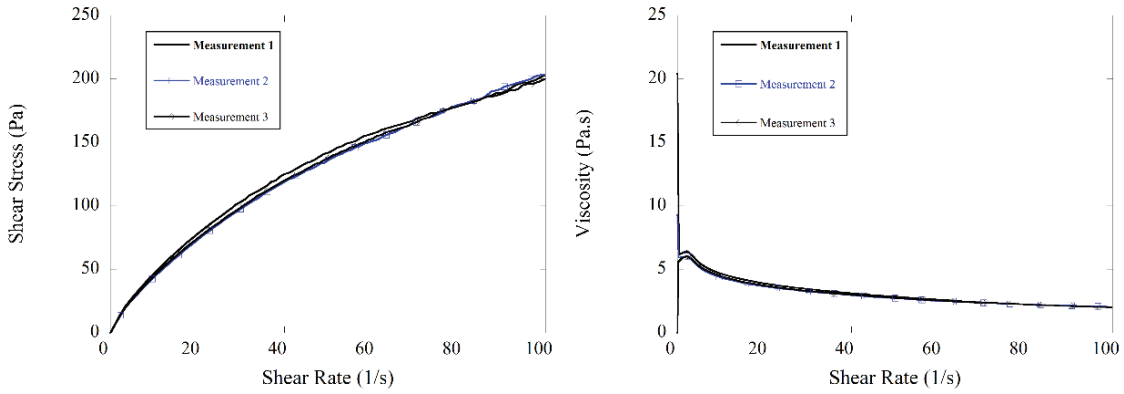

Figure A.6. Three measurements of shear stress-shear rate and viscosity-shear rate curves of the slurry with medium powders in 50 wt% solids content with 3 wt% CMC

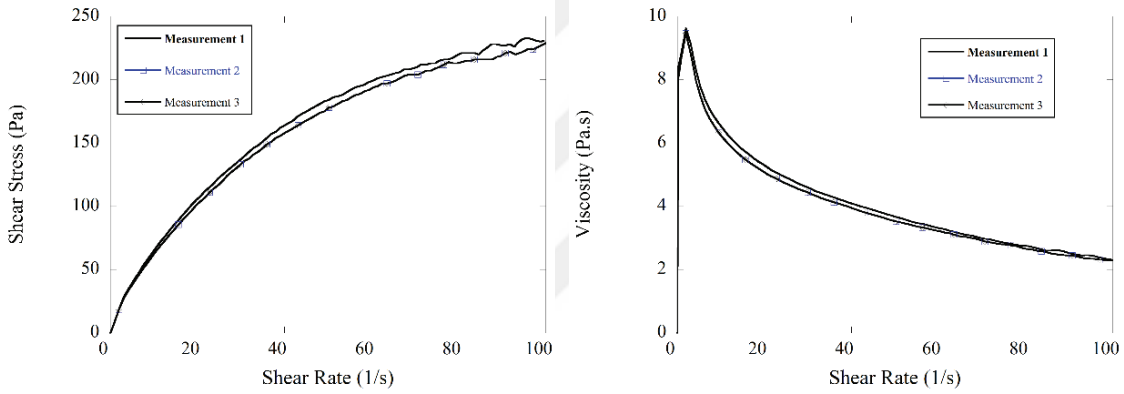

Figure A.7. Three measurements of shear stress-shear rate and viscosity-shear rate curves of the slurry with medium powders in 60 wt% solids content with 3 wt% CMC

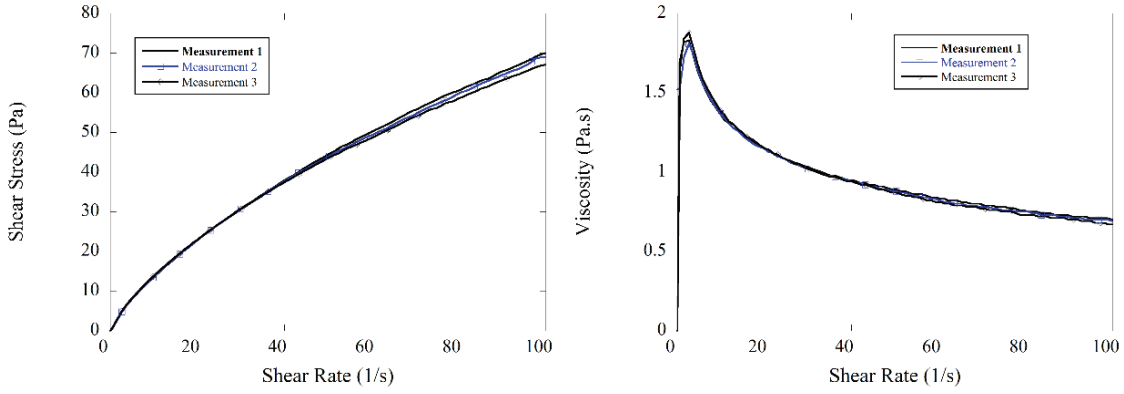

Figure A.8. Three measurements of shear stress-shear rate and viscosity-shear rate curves of the slurry with coarse powders in 50 wt% solids content with 3 wt% CMC

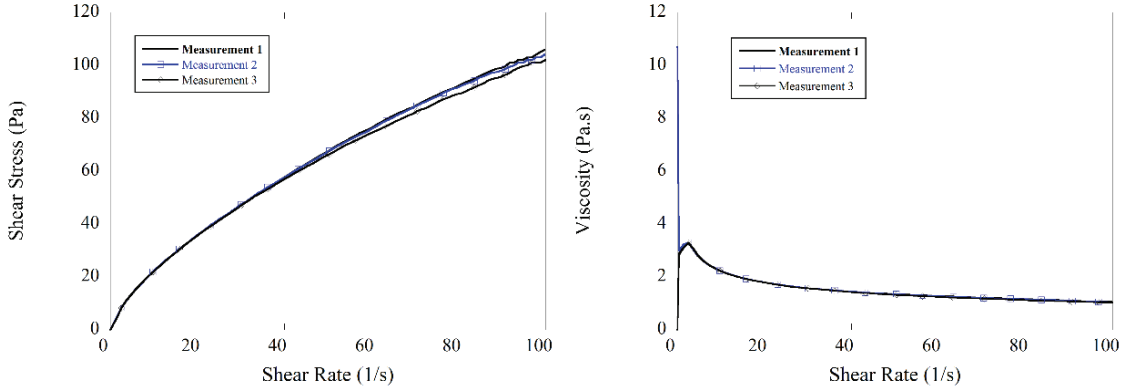

Figure A.9. Three measurements of shear stress-shear rate and viscosity-shear rate curves of the slurry with coarse powders in 60 wt% solids content with 3 wt% CMC

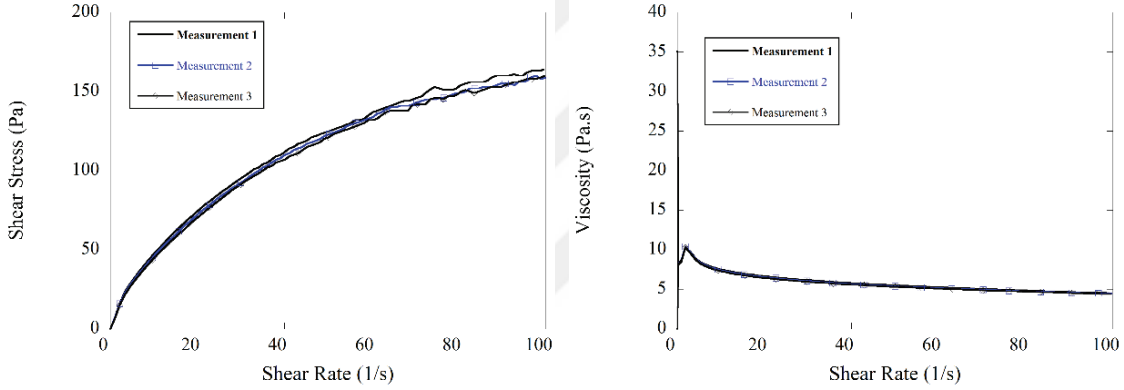

Figure A.10. Three measurements of shear stress-shear rate and viscosity-shear rate curves of the slurry with medium powders in 50 wt% solids content with 4 wt% CMC

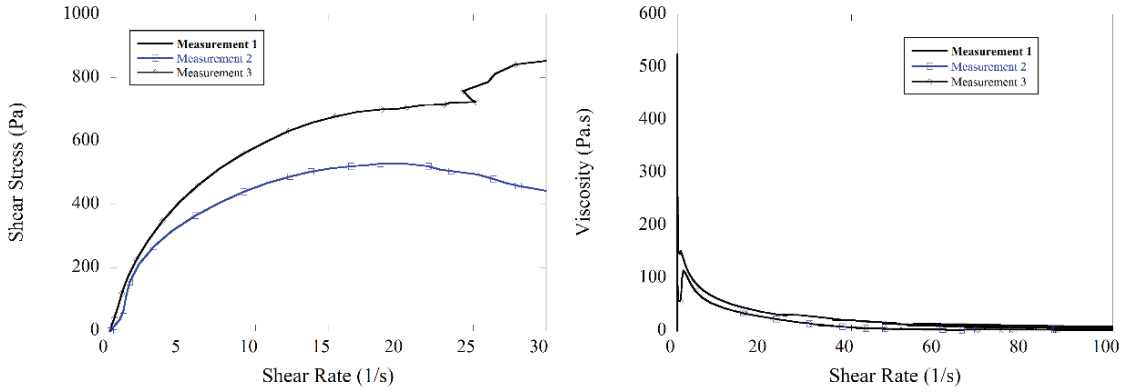

Figure A.11. Three measurements of shear stress-shear rate and viscosity-shear rate curves of the slurry with medium powders in 60 wt% solids content with 4 wt% CMC

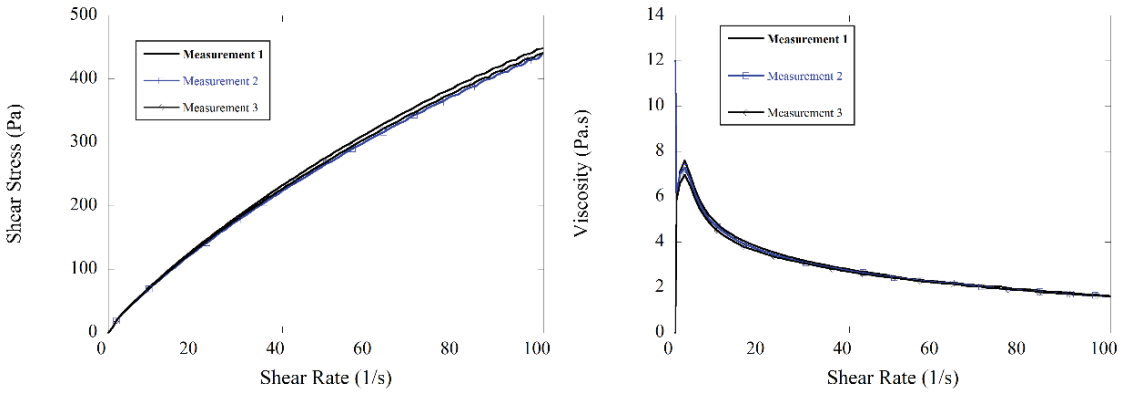

Figure A.12. Three measurements of shear stress-shear rate and viscosity-shear rate curves of the slurry with coarse powders in 50 wt% solids content with 4 wt% CMC

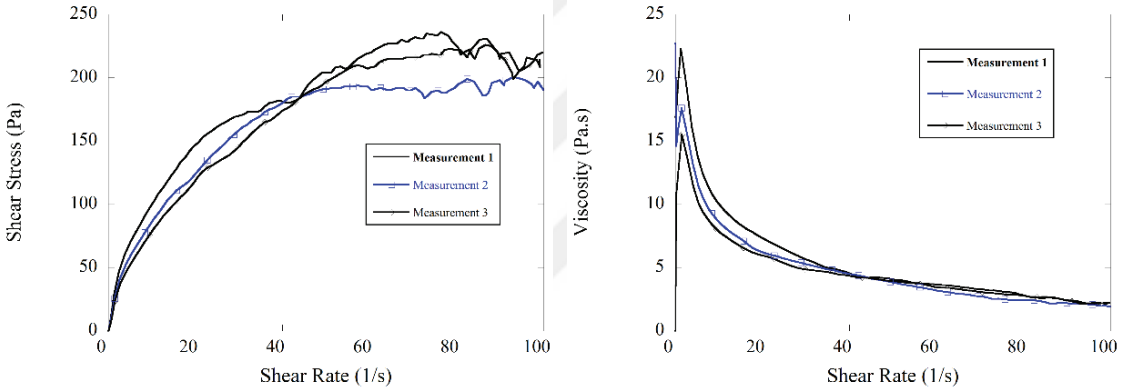

Figure A.13. Three measurements of shear stress-shear rate and viscosity-shear rate curves of the slurry with coarse powders in 60 wt% solids content with 4 wt% CMC

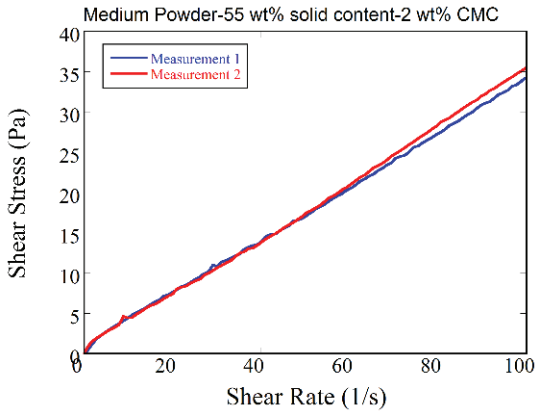

Figure A.14. Two measurements of shear stress-shear rate curve of the slurry with medium powders in 55 wt% solids content with 2 wt% CMC

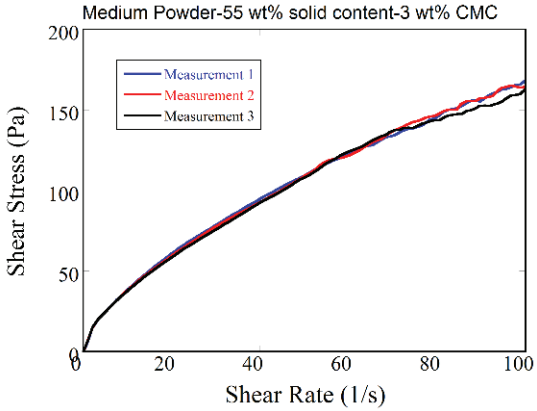

Figure A.15. Three measurements of shear stress-shear rate curve of the slurry with medium powders in 55 wt% solids content with 3 wt% CMC

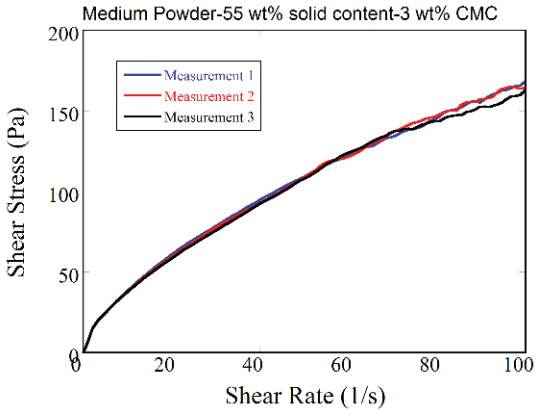

Figure A.15. Three measurements of shear stress-shear rate curve of the slurry with medium powders in 55 wt% solids content with 3 wt% CMC

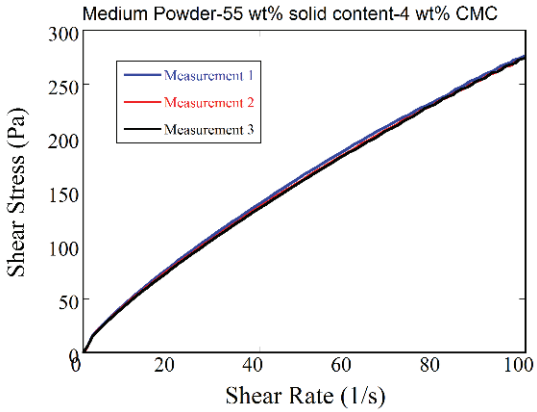

Figure A.16. Three measurements of shear stress-shear rate curve of the slurry with medium powders in 55 wt% solids content with 4 wt% CMC

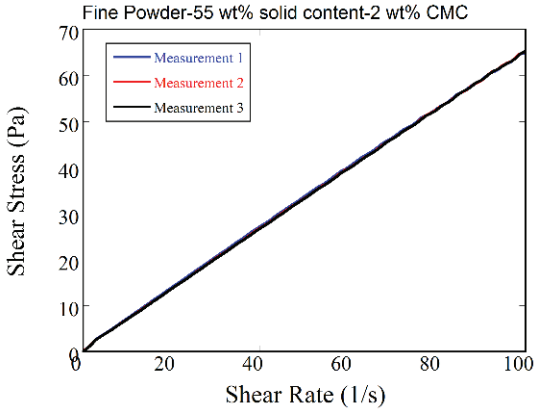

Figure A.17. Three measurements of shear stress-shear rate curve of the slurry with fine powders in 55 wt% solids content with 2 wt% CMC

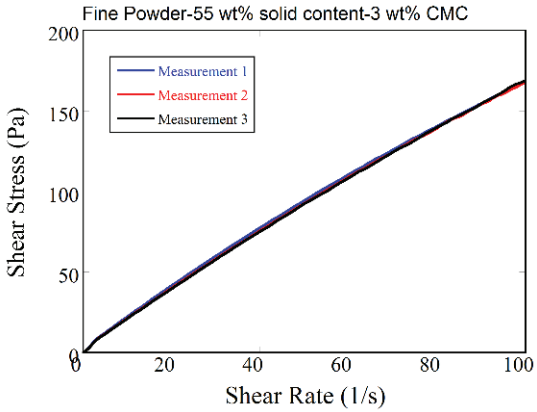

Figure A.18. Three measurements of shear stress-shear rate curve of the slurry with fine powders in 55 wt% solids content with 3 wt% CMC

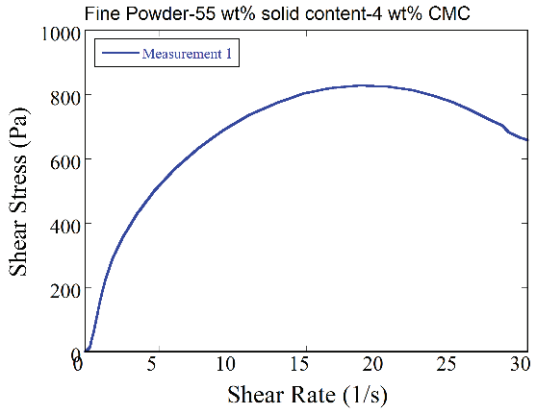

Figure A.19. Shear stress-shear rate curve of the slurry with fine powders in 55 wt% solids content with 4 wt% CMC

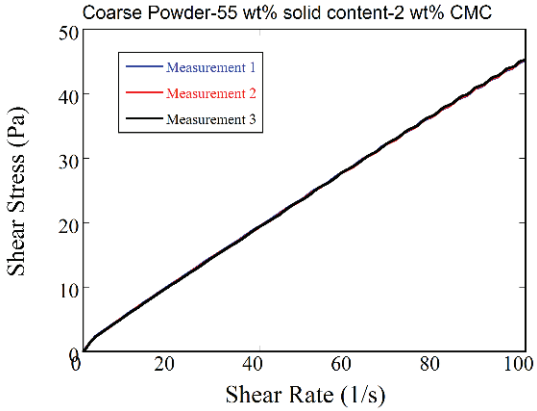

Figure A.20. Three measurements of shear stress-shear rate curve of the slurry with coarse powders in 55 wt% solids content with 2 wt% CMC

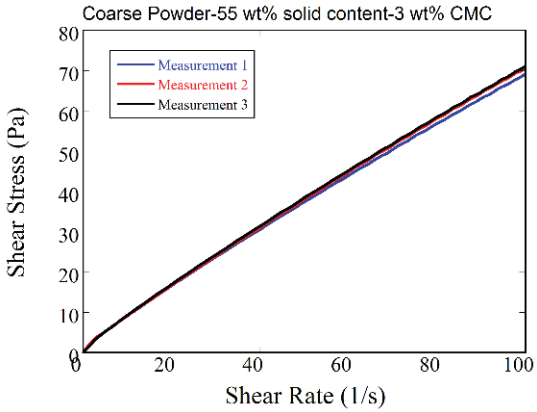

Figure A.21. Three measurements of shear stress-shear rate curve of the slurry with coarse powders in 55 wt% solids content with 3 wt% CMC

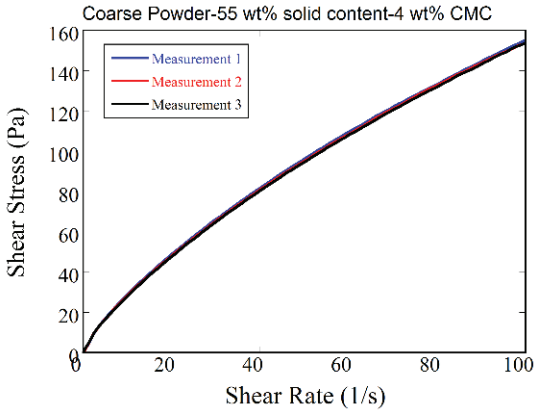

Figure A.22. Three measurements of shear stress-shear rate curve of the slurry with coarse powders in 55 wt% solids content with 4 wt% CMC

A.2. Linear Expansion Experiments

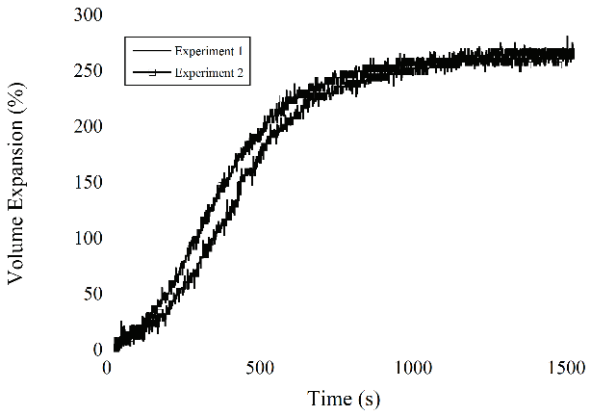

Figure A.23. Two linear expansion measurements of slurries with Medium powders with 2 wt% cmc in 50 wt% solids content

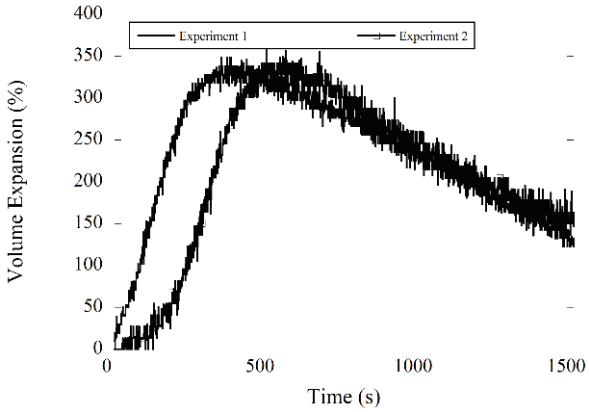

Figure A.24. Two linear expansion measurements of medium powders with 2 wt% cmc in 60 wt% solids content

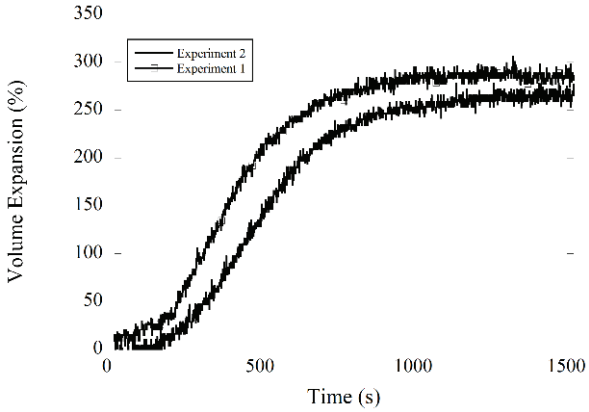

Figure A.25. Two linear expansion measurements of Coarse powders with 2 wt% cmc in 50 wt% solids content

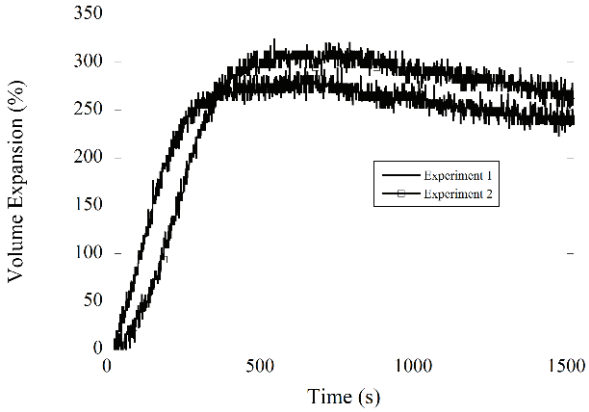

Figure A.26. Two linear expansion measurements of coarse powders with 2 wt% cmc in 60 wt% solids content

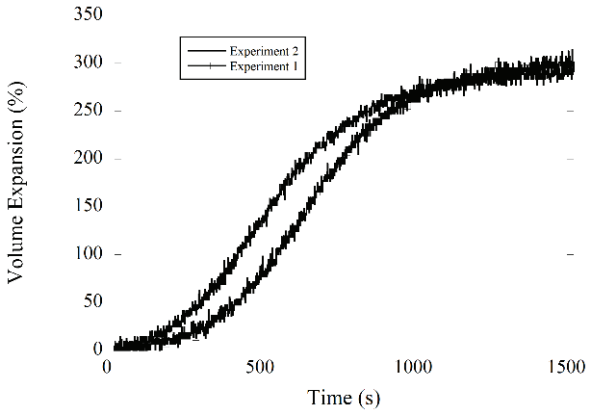

Figure A.27. Two linear expansion measurements of fine Powders with 3 wt% cmc in 50 wt% solids content

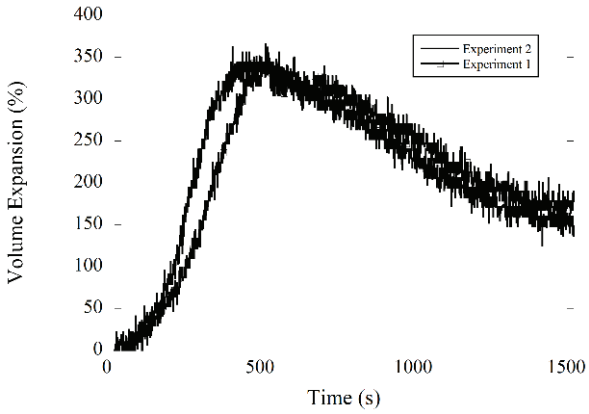

Figure A.28. Two linear expansion measurements of fine Powders with 3 wt% cmc in 60 wt% solids content

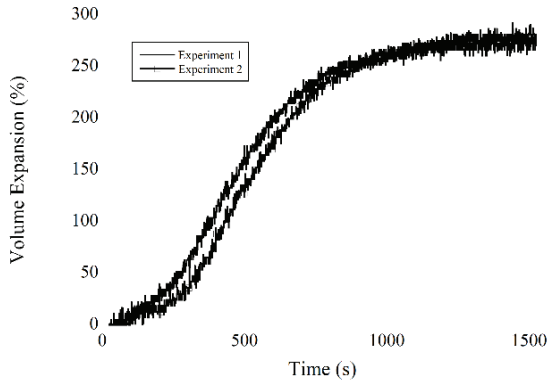

Figure A.29. Two linear expansion measurements of medium powders with 3 wt% cmc in 50 wt% solids content

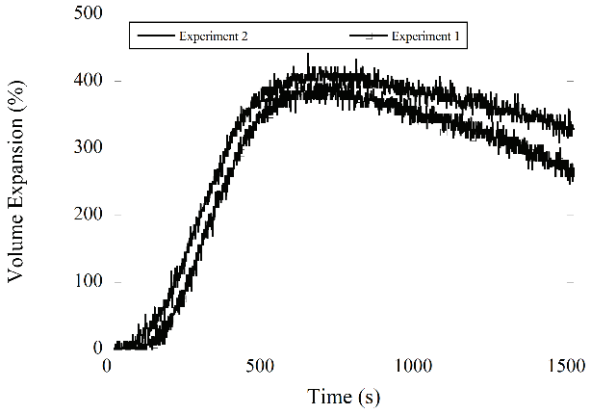

Figure A.30. Two linear expansion measurements of medium powders with 3 wt% cmc in 60 wt% solids content

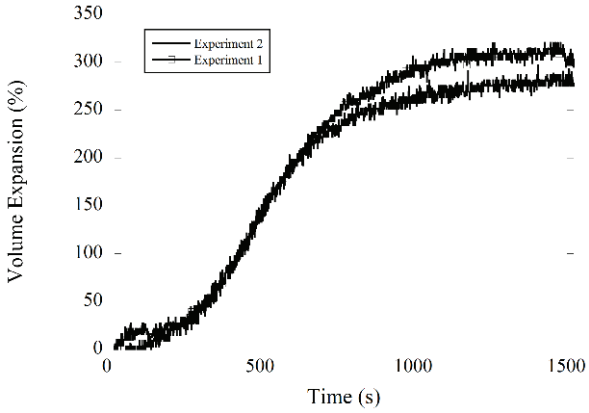

Figure A.31. Two linear expansion measurements of coarse powders with 3 wt% cmc in 50 wt% solids content

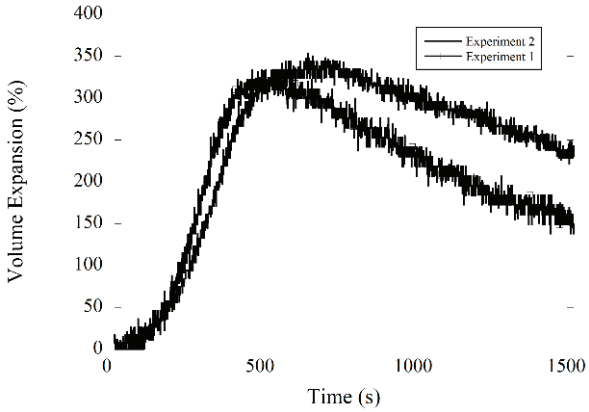

Figure A.32. Two linear expansion measurements of coarse powders with 3 wt% cmc in 60 wt% solids content

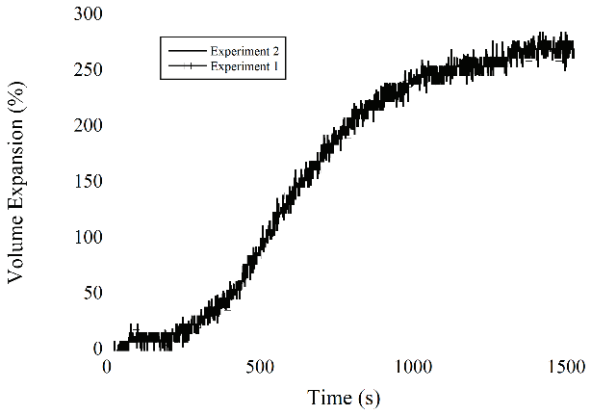

Figure A.33. Two linear expansion measurements of fine powders with 3 wt% cmc in 50 wt% solids content

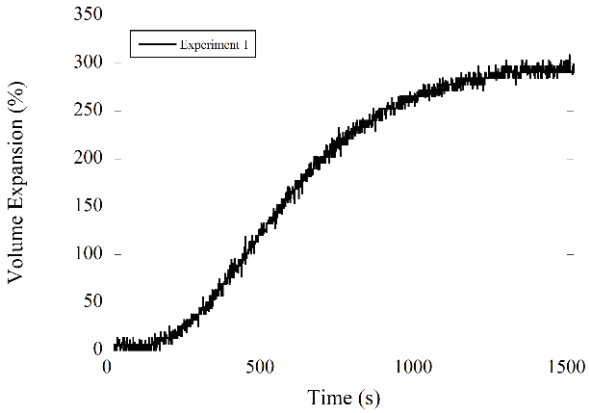

Figure A.34. Linear expansion measurements of medium powders with 4 wt% cmc in 50 wt% solids content

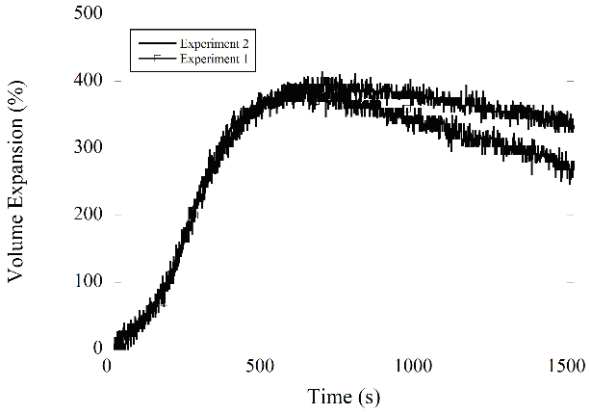

Figure A.35. Two linear expansion measurements of medium powders with 4 wt% cmc in 60 wt% solids content

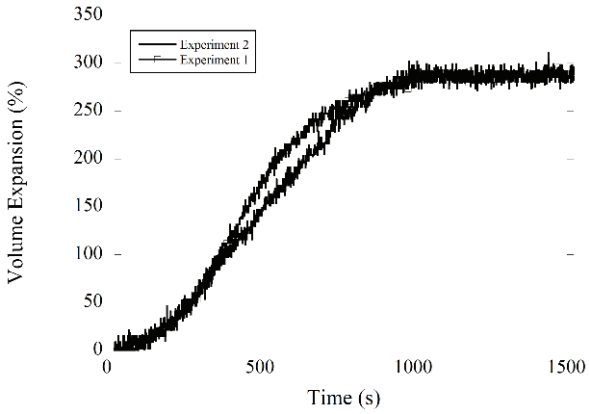

Figure A.36. Two linear expansion measurements of coarse powders with 4 wt% cmc in 50 wt% solids content

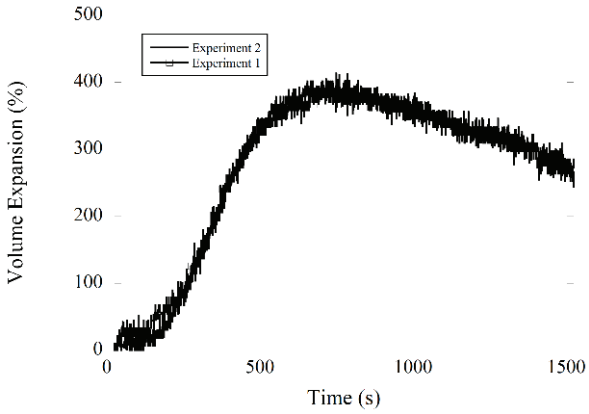

Figure A.37. Two linear expansion measurements of coarse powders with 4 wt% cmc in 60 wt% solids content

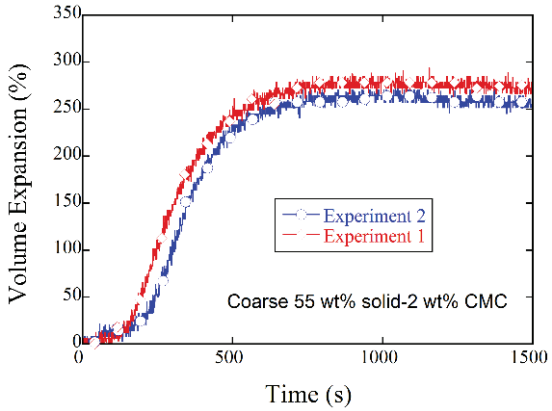

Figure A.38. Two linear expansion measurements of coarse powders with 2 wt% cmc in 55 wt% solids content

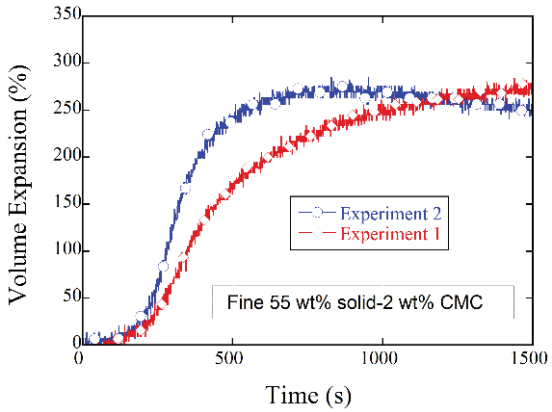

Figure A.39. Two linear expansion measurements of fine powders with 2 wt% cmc in 55 wt% solids content

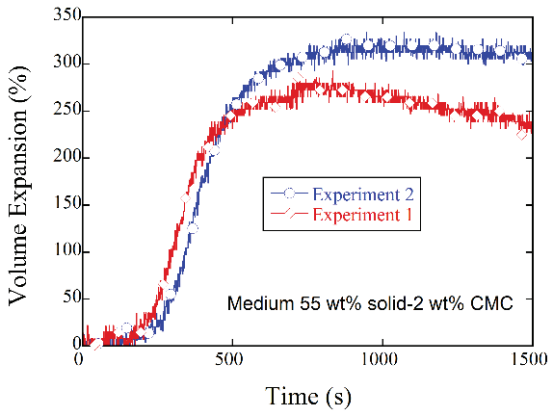

Figure A.40. Two linear expansion measurements of medium powders with 2 wt% cmc in 55 wt% solids content

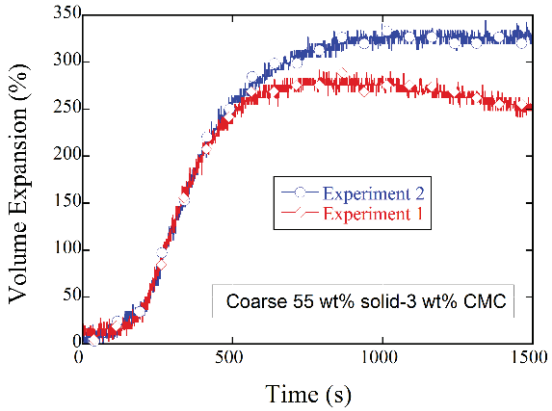

Figure A.41. Two linear expansion measurements of coarse powders with 3 wt% cmc in 55 wt% solids content

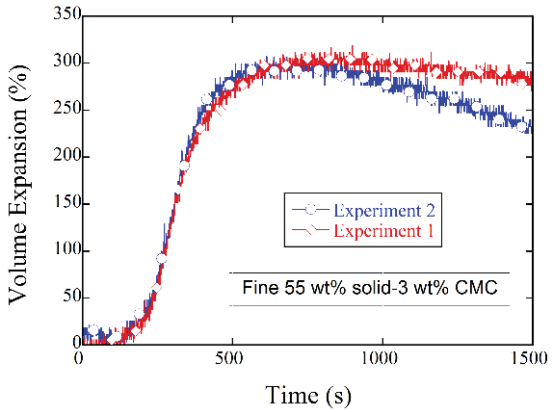

Figure A.42. Two linear expansion measurements of fine powders with 3 wt% cmc in 55 wt% solids content

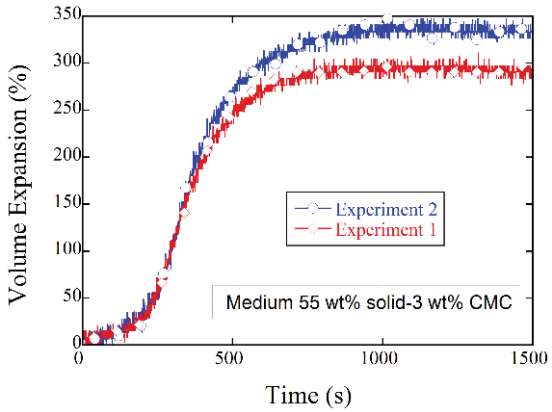

Figure A.43. Two linear expansion measurements of medium powders with 3 wt% cmc in 55 wt% solids content

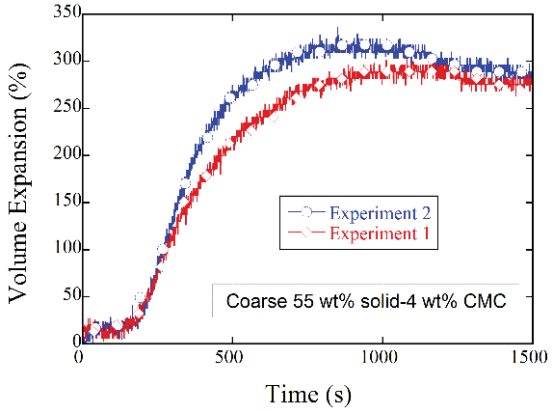

Figure A.44. Two linear expansion measurements of coarse powders with 4 wt% cmc in 55 wt% solids content

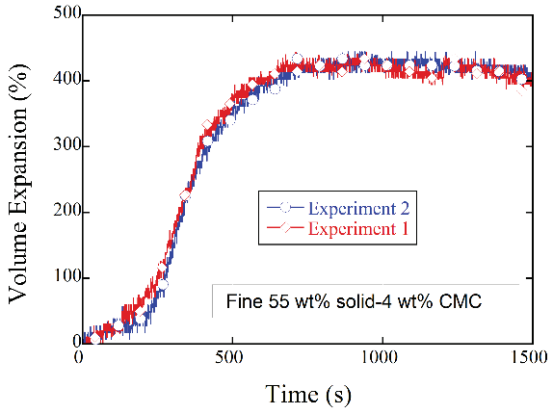

Figure A.45. Two linear expansion measurements of fine powders with 4 wt% cmc in 55 wt% solids content

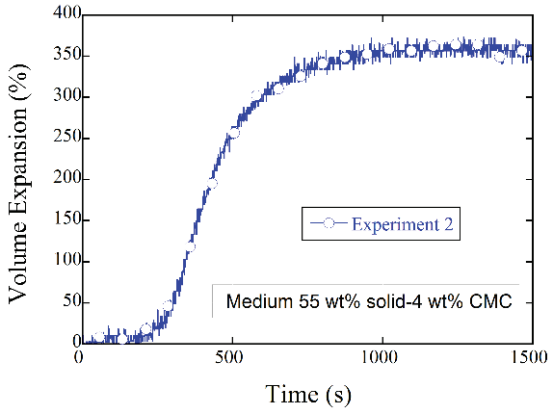

Figure A.46. Two linear expansion measurements of Medium powders with 4 wt% cmc in 55 wt% solids content

VITA

Doğuş ZEREN

Date of Birth: Jun 1987

Place of Birth: İzmir/TURKEY

EDUCATION

B.Sc. (2005-2009): Department of Metallurgical and Materials Engineering, Dokuz Eylül University, İzmir, Turkey

M.Sc. (2010-2013): Department of Materials Science and Engineering, İzmir Institute of Technology, İzmir, Turkey

PhD (2013-2019): Department of Materials Science and Engineering, İzmir Institute of Technology, İzmir, Turkey

EMPLOYMENT HISTORY

- Research and Development Specialist in Norm Fasteners, İzmir, Turkey (2019-present)
- Research Assistant in Department of Materials Science and Engineering, İzmir Institute of Technology, İzmir, Turkey (2010-2019)

SELECTED PUBLICATIONS

Zeren, D., Şentürk, U., Güden, M., "Expansion behavior of waste glass powder slurries containing carboxymethyl cellulose, lime and Al powder", Ceramics International, 2019 (submitted).

Zeren, D., Kesici, K., Tüney, İ., Güden, M., Sukatar, A., "The shape and size effect of the diatom frustule addition on the compression behavior of an epoxy", Materials Science Forum, Vol. 915, pp. 140-146, 2018.

Zeren, D., Güden, M. "The increased compression strength of an epoxy resin with the addition of heat-treated natural nano-structured diatom frustules", Journal of Composite Materials, 51(12), 1681–1691, 2017.

Kesici, K., Tüney, İ., Zeren, D., Güden, M., Sukatar, A. "Morphological and molecular identification of pennate diatoms isolated from Urla, İzmir, coast of the Aegean Sea", Turkish Journal of Biology, 37: 530-537, 2013.